

**STIMULATED BRILLOUIN SCATTERING  
PULSE COMPRESSION AND  
HARMONIC GENERATION: APPLICATIONS  
TO PRECISION XUV LASER SPECTROSCOPY**



VRIJE UNIVERSITEIT

**STIMULATED BRILLOUIN SCATTERING  
PULSE COMPRESSION AND  
HARMONIC GENERATION: APPLICATIONS  
TO PRECISION XUV LASER SPECTROSCOPY**

ACADEMISCH PROEFSCHRIFT

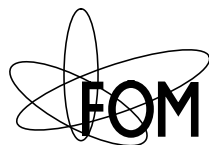
ter verkrijging van de graad van doctor aan  
de Vrije Universiteit Amsterdam,  
op gezag van de rector magnificus  
prof.dr. T. Sminia,  
in het openbaar te verdedigen  
ten overstaan van de promotiecommissie  
van de faculteit der Exacte Wetenschappen /  
Natuurkunde en Sterrenkunde  
op donderdag 7 juni 2001 om 13.45 uur  
in het hoofgebouw van de universiteit,  
De Boelelaan 1105

door

**Iavor Tzvetanov Veltchev**

geboren te Rousse, Bulgarije

Promotor: prof.dr. W. Hogervorst  
Copromotor: dr. W.M.G. Ubachs



The work described in this thesis was performed as part of the research program of the “Stichting voor Fundamenteel Onderzoek der Materie” (FOM) with financial support of the “Nederlandse Organisatie voor Wetenschappelijk Onderzoek” (NWO), and was carried out at the Laser Centre of the Vrije Universiteit Amsterdam.

*на Христина и Александър*



# Contents

<b>Preface</b>	<b>1</b>
<b>1 Introduction to stimulated Brillouin scattering and high-order harmonic generation.</b>	<b>3</b>
1.1 Theory of SBS	3
1.1.1 Spontaneous light scattering from thermal fluctuations	3
1.1.2 Stimulated Brillouin Scattering	7
1.2 Applications of SBS	17
1.2.1 Phase conjugation by SBS	17
1.2.2 Pulse compression by SBS	21
1.2.3 Other applications	24
1.3 High-order harmonic generation	26
<b>2 SBS pulse compression to 200 ps in a compact single-cell setup.</b>	<b>33</b>
2.1 Introduction	33
2.2 Experimental setup and measurement methods	34
2.3 Results and discussion	36
2.3.1 Transverse beam profile effect in SBS	37
2.3.2 Pulse compression at 532 nm for various liquids	38
2.3.3 Pulse compression at 355 nm	40
2.3.4 Proposal for a simplified low-loss SBS-geometry	41
2.4 Conclusion	42
<b>3 Pulse compression to the sub-phonon lifetime region by half-cycle gain in transient stimulated Brillouin scattering.</b>	<b>45</b>
3.1 Introduction	45
3.2 Theory of transient SBS	45
3.3 Numerical model	49
3.4 Results and Discussion	51
3.5 Experiment	52
3.6 Conclusions	53

<b>4</b>	<b>Higher-order stimulated Brillouin scattering with Bessel beams.</b>	<b>59</b>
4.1	Introduction	59
4.2	Experimental setup	61
4.3	Results and discussion	61
4.4	Conclusions	64
<b>5</b>	<b>A Dense Grid of Reference Iodine Lines for Optical Frequency Calibration in the Range 571-596 nm.</b>	<b>67</b>
5.1	Introduction	67
5.2	Experimental	68
5.3	Data analysis	72
5.4	The reference standard	76
5.5	Conclusions	76
<b>6</b>	<b>Precision frequency calibration in XUV.</b>	<b>79</b>
6.1	Precision spectroscopy of argon at 105 nm	79
6.1.1	Introduction	79
6.1.2	Experimental setup	80
6.1.3	Results and discussion	80
6.1.4	Conclusion	85
6.2	Precision VUV spectroscopy of xenon	85
6.2.1	Introduction	86
6.2.2	Experimental	86
6.2.3	Data analysis and discussion	87
6.2.4	Conclusions	93
6.3	Precision XUV spectroscopy of N <sub>2</sub> around 98 nm	93
6.3.1	Introduction	93
6.3.2	Experimental	93
6.3.3	Results	95
6.3.4	Conclusion	97
<b>7</b>	<b>Table-top narrow-band XUV laser source.</b>	<b>99</b>
7.1	Introduction	99
7.2	Continuous-wave part of the setup	100
7.3	The fiber connection	102
7.4	Pulse-dye-amplifier	104
7.4.1	Spectral and temporal characterization of the PDA output	106
7.5	Ti:Sapphire amplifier	110
7.5.1	Ti:Sapphire pre-amplifier	110
7.5.2	Ti:sapphire multi-pass amplifier	113
7.6	Outlook	114

<b>Publications</b>	<b>119</b>
<b>Samenvatting</b>	<b>121</b>
<b>Обобщение</b>	<b>125</b>
<b>Dankwoord</b>	<b>129</b>



## Preface

The present Thesis is devoted to precision spectroscopy in the extreme ultraviolet (XUV) region of the electromagnetic spectrum aided by the use of two nonlinear processes: stimulated Brillouin scattering (SBS) and harmonic generation. The former is used to efficiently compress laser pulses in order to achieve high peak intensities, necessary for enhancing the yield from a nonlinear process such as harmonic generation. The process of pulse compression by SBS is discussed in detail in the first part of the Thesis, both from theoretical and experimental perspective. The use of successive second and third harmonic generation for precision frequency measurements in the XUV is demonstrated as well. A laser system is being developed (the latest results are presented in Chapter 7) that combines both SBS pulse compression and harmonic generation techniques, and is expected to deliver narrowband ( $\delta\nu/\nu \approx 3 \times 10^{-6}$ ) wavelength tunable pulses in the XUV.

This Thesis comprises 7 chapters which include 58 figures and 14 tables, and is organized as follows.

Chapter 1 is an introduction to stimulated Brillouin scattering and high-order harmonic generation. Both these essentially nonlinear phenomena are important elements in this Thesis and bear relevance to different chapters that follow. In the first two sections of Chapter 1 the basic theory of the Brillouin scattering process is discussed along with its applications. The steady-state theory of SBS is developed with emphasis on the two important configurations (SBS amplifier and SBS generator) essential for understanding SBS pulse compression. From a historical perspective the pioneering experiments on SBS are briefly discussed with the aim to follow the development of the ideas leading to SBS pulse compression throughout the 1960s, 70s, and 80s. Some of the many practical applications of SBS with strong relevance to the content of this Thesis are introduced as well. In the last section of Chapter 1 the basics of high-order harmonic generation are introduced both in focused and guided geometry.

Different schemes for experimental realization of SBS pulse compression are discussed in Chapter 2. Second and third harmonics of a pulsed Nd:YAG laser are efficiently compressed in different liquid media in a new, single-cell generator-amplifier setup. Pulses as short as 200 ps are generated from the 5 ns output of a commercial injection-seeded Q-switched Nd:YAG system with an exceptionally high efficiency. The transverse effects in the pulse compression process are investigated as well. We provide a recipe for continuously tuning the compressed pulse duration from 2 ns to 200 ps, thus turning the commercially available Nd:YAG lasers into more versatile laboratory tools for dynamical and nonlinear optical studies.

The possibility for SBS pulse compression below the phonon lifetime limit is the subject of Chapter 3. A new approach to the theory of transient SBS is presented which reveals the true physical limitations to the output pulse duration in the SBS compressor setup. A numerical method for modeling the evolution of the process in fully transient regime is developed and the different stages of the process are discussed in detail. Under proper conditions pulses as short as a half acoustic cycle can be generated. An experimental study of the process in the transient regime confirms the theoretical predictions.

A fundamental experimental study of the SBS process pumped by a non-diffracting (Bessel) beam is presented in Chapter 4. Higher-order Stokes components have been observed for the first time as a result of pure multiple scattering in a bulk medium. The spatial, spectral and temporal properties of the interacting waves are discussed.

A contribution to precision metrology is presented in Chapter 5. Using Doppler-free saturation spectroscopy in molecular iodine in the range of 571 – 596 nm more than 100 hyperfine components in the  $B-X$  system are calibrated with average absolute accuracy of 2 MHz. In combination with a theoretical study of the hyperfine splittings the absolute frequencies of 1584 hyperfine components in six ( $v'-1$ ) bands ( $v'=13..18$ ) are predicted with overall accuracy of 2 MHz for  $9 \leq J \leq 140$ . These frequencies form a dense grid of reference lines for precision spectroscopic studies. It is more than an order of magnitude more accurate than the widely used iodine atlas, based on Doppler-broadened lines, and its density (a line in nearly each wavenumber) makes it an easy to use spectroscopic tool for absolute wavelength calibration.

This new reference standard along with its extension towards longer wavelengths is used for precision frequency calibration in the extreme ultraviolet region as discussed in Chapter 6. A narrow-band laser source based on successive second and third harmonic generation of powerful Fourier-transform limited pulses is applied for precision spectroscopic studies of argon, xenon and nitrogen at wavelengths below 105 nm. High absolute accuracy of the measurements is achieved by simultaneous detection of both saturated absorption spectrum of  $I_2$  and transmission fringes of an actively stabilized Fabry-Perot cavity in the visible along with the XUV spectrum. This scheme yields an absolute accuracy of less than 100 MHz for measurements in the XUV.

In Chapter 7 a new project is discussed. It combines the scientific results presented in the preceding chapters into a new design for a narrowband tunable XUV laser source. The latest development on this undertaking is presented. The design aims at high-order harmonic generation of powerful infrared pulses of 300 ps pulse duration. A narrow-band CW Ti:sapphire ring-laser is used for injection seeding of a dye amplifier chain, pumped by SBS compressed pulses of Nd:YAG laser. Fourier-transform limited wavelength tunable pulses of 300 ps duration are amplified in a multipass Ti:sapphire amplifier to achieve highly energetic pulses that subsequently can be used for harmonic generation.

# Chapter 1

## Introduction to stimulated Brillouin scattering and high-order harmonic generation.

In the first two Sections of this Chapter the basic concepts underlying the Brillouin scattering process are discussed. The steady-state theory of stimulated Brillouin scattering (SBS) is developed with an emphasis on the two cases of SBS amplification and SBS generation. A historical review of the pioneering experiments is given and many of the practical applications of SBS are discussed. In the last section the basics of high-order harmonic generation are introduced both in focused and guided geometry.

### 1.1 Theory of SBS

#### 1.1.1 Spontaneous light scattering from thermal fluctuations

Spontaneous light scattering occurs when light interacts with fluctuations in the optical properties of a material medium. Any inhomogeneity in the medium (due to fluctuations from a variety of sources, discussed in the following) creates a rich angular and frequency spectrum [1]. There are three quantities which characterize the individual scattering process: the frequency shift  $\Omega_X$ , the line-width  $\Gamma_X$  and the scattering cross section  $\sigma_X$ .

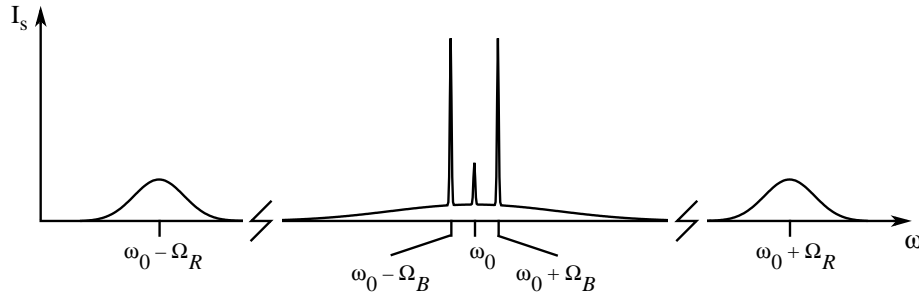


**Figure 1.1:** Spontaneous light scattering.

Consider a light scattering experiment in which monochromatic light with frequency  $\omega_0$  propagates through an inhomogeneous medium. The scattered light is detected and a typical spectrum is shown in Fig. 1.1. In general it consists of six peaks: Stokes

and anti-Stokes Raman, Stokes and anti-Stokes Brillouin, Rayleigh and Rayleigh-wing features are seen.

The large shift of the order of  $1000 \text{ cm}^{-1}$  is due to scattering from vibrational modes of the molecules constituting the medium and is known as Raman scattering. In Fig. 1.1 only one pair of lines (Stokes and anti-Stokes) is depicted for simplicity, but in polyatomic molecular systems, or crystals with several atoms in the unit cell, there are many such vibrational frequencies, each creating a pair of Stokes ( $\omega_0 - \Omega_R$ ) and anti-Stokes ( $\omega_0 + \Omega_R$ ) components. Since the populations of the excited vibrational modes are very low at room temperature, the anti-Stokes intensities are small compared with the corresponding Stokes components. Measurement of the width of the Raman line, typically a few  $\text{cm}^{-1}$ , yields a excited state lifetime of the order of several pico-seconds.

The broad peak centered around  $\omega_0$  corresponds to Rayleigh-wing scattering from fluctuations in the orientation of anisotropic molecules. Its characteristic time  $\tau_{RW} = 4\pi a^3 \eta_s / 3kT_0$  ( $a$  - average molecular radius,  $\eta_s$  - viscosity [2]) at room temperature is of the order of several pico-seconds, while the scattered light extends over many wavenumbers.

The central triplet ( $\omega_0; \omega_0 \pm \Omega_B$ ) in Fig. 1.1 is due to scattering from two classes of thermally excited fluctuations. The unshifted line at  $\omega_0$  is the spontaneous Rayleigh scattering from entropy fluctuations at constant pressure, while the two satellites are the Stokes and anti-Stokes components of the spontaneous Brillouin scattering from adiabatic fluctuations of density propagating with the velocity of sound in the medium. Both processes can be theoretically treated simultaneously. The works of Einstein [3] and Landau and Placzek [4] led to an expression for the total scattering coefficient (differential cross-section per unit volume) for scattering from thermal fluctuations:

$$R_{tot} = \frac{\omega_0^4}{16\pi^2 c^4} \left( \rho \frac{\partial \epsilon}{\partial \rho} \right)^2 C_T k_B T \sin^2 \phi, \quad (1.1)$$

where  $\omega_0$  is the incident light frequency,  $C_T = -\frac{1}{V} \left( \frac{\partial V}{\partial \rho} \right)_T$  the isothermal compressibility,  $k_B$  - the constant of Boltzmann, and  $\phi$  - the angle between the polarization vector of the light wave and the direction of observation. Using Eq.(1.1) the total intensity, scattered from volume  $V$  in direction  $\phi$  at distance  $L$  is given by:

$$I_{tot} = I_0 \frac{\omega_0^4 V}{16\pi^2 L^2 c^4} \left( \rho \frac{\partial \epsilon}{\partial \rho} \right)^2 C_T k_B T \sin^2 \phi. \quad (1.2)$$

In order to determine the spectrum of the scattered light, the dynamical behavior of the fluctuations has to be taken into account [5]. We represent the fluctuation of the dielectric constant as:

$$\Delta \tilde{\epsilon} = \frac{\partial \epsilon}{\partial \rho} \Delta \tilde{\rho}. \quad (1.3)$$

By choosing entropy  $S$  and pressure  $p$  as independent thermodynamical variables,

we can express the density variation  $\Delta\tilde{\rho}$  in Eq.(1.3) as:

$$\Delta\tilde{\rho} = \left(\frac{\partial\rho}{\partial p}\right)_S \Delta\tilde{p} + \left(\frac{\partial\rho}{\partial S}\right)_p \Delta\tilde{S}. \quad (1.4)$$

Here the first term on the right-hand side describes adiabatic density fluctuations (acoustic waves) and leads to Brillouin scattering, whereas the second term describes isobaric entropy fluctuations and leads to Rayleigh scattering. The two contributions are quite different in character, since the evolution of a pressure wave is governed by a wave equation with damping [6]:

$$\frac{\partial^2 \Delta\tilde{p}}{\partial t^2} - \Gamma \nabla^2 \left( \frac{\partial \Delta\tilde{p}}{\partial t} \right) - v^2 \nabla^2 \Delta\tilde{p} = 0, \quad (1.5)$$

while the entropy fluctuations are described by a diffusion equation:

$$\rho c_p \frac{\partial \Delta\tilde{S}}{\partial t} - \kappa \nabla^2 \Delta\tilde{S} = 0. \quad (1.6)$$

In Eqs.(1.5, 1.6)  $c_p$  is the specific heat at constant pressure,  $\kappa$  - the thermal conductivity,  $\Gamma$  the sound wave damping parameter, and  $v$  the velocity of sound.

#### *Spontaneous Brillouin scattering*

Consider Brillouin scattering from a sound wave of the form:  $\Delta\tilde{p} = \Delta p e^{i(qz - \Omega t)} + \text{c.c.}$ , which substituted into the acoustic equation (1.5) leads to a dispersion relation of the form  $\Omega^2 = q^2(v^2 - i\Omega\Gamma)$ . It can be transformed in:

$$q \simeq \frac{\Omega}{v} + i \frac{\Gamma_B}{2v}, \quad (1.7)$$

where  $\Gamma_B = \Gamma q^2$  is the phonon decay rate, which is the quantity used to define phonon lifetime  $\tau_p = 1/\Gamma_B$  and sound absorption coefficient  $\alpha_s = \Gamma_B/v$ .

Let us write the incident optical field in the form:

$$\tilde{E}_0(\mathbf{r}, t) = E_0 e^{i(\mathbf{k}\cdot\mathbf{r} - \omega_0 t)} + \text{c.c.},$$

and assume that the scattered field obeys the driven wave equation:

$$\nabla^2 \tilde{E} - \frac{n^2}{c^2} \frac{\partial^2 \tilde{E}}{\partial t^2} = \frac{4\pi}{c^2} \frac{\partial^2 \tilde{P}}{\partial t^2}. \quad (1.8)$$

We consider the additional polarization in the medium (due to the fluctuation  $\Delta\epsilon$ ) with the form  $\tilde{P} = \frac{\Delta\epsilon}{4\pi} \tilde{E}_0$ . Taking into account Eqs.(1.3,1.4) one can write:

$$\tilde{P}(\mathbf{r}, t) = \frac{1}{4\pi} \frac{\partial\epsilon}{\partial\rho} \left( \frac{\partial\rho}{\partial p} \right)_S \Delta\tilde{p}(\mathbf{r}, t) \tilde{E}_0(\mathbf{r}, t) = \frac{1}{4\pi} \gamma_e C_S \Delta\tilde{p}(\mathbf{r}, t) \tilde{E}_0(\mathbf{r}, t), \quad (1.9)$$

where  $\gamma_e = (\rho \partial \epsilon / \partial \rho)|_{\rho=\rho_0}$  is the electrostrictive constant and  $C_S = \rho^{-1}(\partial \rho / \partial p)_S$  - the adiabatic compressibility. By substituting in Eq.(1.8) a pressure disturbance of the form  $\Delta \tilde{p}(\mathbf{r}, t) = \Delta p e^{i(\mathbf{q} \cdot \mathbf{r} - \Omega t)} + \text{c.c.}$  we get:

$$\nabla^2 \tilde{E} - \frac{n^2}{c^2} \frac{\partial^2 \tilde{E}}{\partial t^2} = -\frac{\gamma_e C_S}{c^2} \left[ (\omega_0 - \Omega)^2 E_0 \Delta p^* e^{i[(\mathbf{k}_L - \mathbf{q}) \cdot \mathbf{r} - (\omega_0 - \Omega)t]} + (\omega_0 + \Omega)^2 E_0 \Delta p e^{i[(\mathbf{k}_L + \mathbf{q}) \cdot \mathbf{r} - (\omega_0 + \Omega)t]} + \text{c.c.} \right] \quad (1.10)$$

The first term on the right-hand side leads to Stokes scattering, while the second one to anti-Stokes scattering. The two situations are graphically presented in Fig. 1.2a,b.

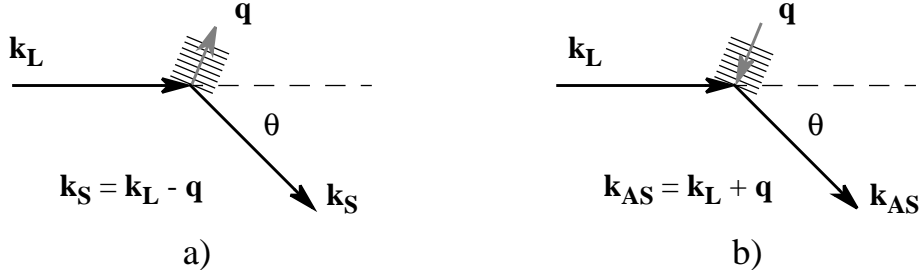


**Figure 1.2:** Spontaneous Brillouin scattering from propagating density fluctuations; a) - spontaneous Stokes scattering at angle  $\theta$ ; b) - spontaneous anti-Stokes scattering.

From Eq.(1.10) it follows that the additional polarization has a component with a wave vector  $\mathbf{k}_{S/AS} = \mathbf{k}_L \mp \mathbf{q}$  and a shifted frequency  $\omega_{S/AS} = \omega \mp \Omega$ . In order to satisfy both the energy and momentum conservation during the scattering process, assuming  $\omega_{S/AS} \approx \omega_0$  and  $|\mathbf{k}_{S/AS}| \approx |\mathbf{k}_L|$ , the wave vector and frequency of the phonon involved must obey the following relations:

$$|\mathbf{q}| = 2|\mathbf{k}_L| \sin \frac{\theta}{2}, \quad (1.11 \text{ a})$$

$$\Omega = 2n\omega_0 \frac{v}{c} \sin \frac{\theta}{2}, \quad (1.11 \text{ b})$$

where  $\theta$  is the scattering angle measured with respect to  $\mathbf{k}_L$ . The relations (1.11 a, 1.11 b) were first derived by Brillouin in his pioneering work [7]. In the case of forward scattering ( $\theta = 0$ ) it is clear, that the Brillouin shift is equal to zero, whereas for backward scattering it is largest and its value is  $\Omega_{\max} = \Omega(\theta = 180^\circ) = 2n\omega_0 v/c$ .

For the Brillouin linewidth  $\Gamma_B = \Gamma|\mathbf{q}|^2$  we obtain:

$$\Gamma_B = \frac{1}{\tau_p} = 4n^2 \Gamma \frac{\omega_0^2}{c^2} \sin^2 \frac{\theta}{2}. \quad (1.12)$$

When the second harmonic of Nd:YAG laser ( $\lambda_0 = 532$  nm) is scattered in water ( $v = 1480$  m/s,  $n = 1.33$ ), the Brillouin shift for backscattering is  $\Omega_B/2\pi = 7.4$  GHz and the Brillouin linewidth is  $\Gamma_B/2\pi = 540$  MHz. A phonon lifetime  $\tau_p = 295$  ps, and a sound wave absorption coefficient  $\alpha_s = \Gamma_B/v = 2.3 \times 10^4$  cm<sup>-1</sup> can be calculated as well. The propagation distance of the phonons  $L_s = \alpha_s^{-1} = 435$  nm is shorter than the light wavelength and for all practical modeling applications the phonons can be considered essentially non-moving.

### 1.1.2 Stimulated Brillouin Scattering

In the preceding section, the light intensity was assumed to be low enough that it does not alter the optical properties of the medium. In that case only spontaneous scattering due to thermal fluctuations can occur. In the presence of a strong optical field, due to a variety of processes (electrostriction, absorption), the fluctuations can be amplified and scatter the light even stronger. This positive feedback leads to a whole new class of nonlinear phenomena, known as stimulated scattering processes.

Here we discuss the stimulated Brillouin scattering process (SBS), which takes place when the optical field drives acoustic waves in the medium. The general scheme for observing SBS involves a laser field with frequency  $\omega_L$  which interacts with a co-propagating pressure wave of frequency  $\Omega$ . The light, which is scattered backwards, according to the energy conservation is down-shifted and its frequency is  $\omega_S = \omega_L - \Omega$ . The interference between the incident and the scattered optical fields contains an acoustic frequency term at  $\Omega = \omega_L - \omega_S$ , which if powerful enough can itself create an acoustic wave. The resulting amplified acoustic wave can scatter more efficiently the incident field, thus amplifying the scattered light at Stokes frequency ( $\omega_S$ ). This interaction can lead to an exponential growth of the Stokes intensity if both the pump and the Stokes waves overlap over an extended propagation distance. In focused geometry this is the case of backward scattering only; in forward direction according to Eq.(1.11 b) the acoustic wave frequency vanishes. In a cavity SBS under 90° can be realized as well.

The physical mechanism by which the two optical fields can generate a pressure wave is either electrostriction<sup>a</sup> or absorption. The former is always present and is dominant in lossless media, which makes it the most interesting from a practical point of view. The latter occurs in lossy substances only and we shall not discuss it here. The electrostrictively induced pressure, created by a static electric field is given by [5]:

$$p_{st} = -\rho \frac{\partial \epsilon}{\partial \rho} \frac{E^2}{8\pi} \equiv -\gamma_e \frac{E^2}{8\pi}, \quad (1.13)$$

where  $\gamma_e$  is the electrostrictive constant and  $E$  is the static electric field strength. The minus sign in Eq.(1.13) reflects the fact that the pressure is reduced in regions of high field strength, hence the fluid is drawn into these regions and the density  $\rho$  is increasing.

---

<sup>a</sup>Electrostriction is the tendency of the materials to become compressed in the presence of electric field.

### Basic equations

Initiated from backward spontaneous Brillouin scattering the stimulated process involves interaction of three waves: two optical (laser and Stokes) and one acoustic. Let us consider them as scalar plane-waves in the form:

$$E_1(z, t) = A_1(z, t)e^{i(k_1 z - \omega_1 t)} + c.c., \quad (1.14 a)$$

$$E_2(z, t) = A_2(z, t)e^{i(-k_2 z - \omega_2 t)} + c.c., \quad (1.14 b)$$

$$\bar{\rho}(z, t) = \rho_0 + \rho(z, t)e^{i(q_B z - \Omega_B t)} + c.c., \quad (1.14 c)$$

propagating along the  $z$ -axis. In Eqs.(1.14 a - 1.14 c) the frequencies and the wave-vectors satisfy energy ( $\omega_1 = \omega_2 + \Omega_B$ ) and momentum ( $k_1 = q_B - k_2$ ) conservation laws. Under the assumption of small Stokes shift ( $\omega = \omega_1 \approx \omega_2$ ) the acoustic frequency is given by Eq.(1.11 b) for backscattering ( $\theta = 180^\circ$ ):  $\Omega_B = 2n\omega v/c$ . The two optical fields are governed by the Maxwell's equations, whereas the acoustic field is described by the Navier-Stokes equation with electrostrictive driving term:

$$\frac{\partial^2 E_i}{\partial z^2} - \frac{n^2}{c^2} \frac{\partial^2 E_i}{\partial t^2} = \frac{4\pi}{c^2} \frac{\partial^2 P_i}{\partial t^2}, i = 1, 2 \quad (1.15 a)$$

$$\frac{\partial^2 \bar{\rho}}{\partial t^2} - \Gamma \nabla^2 \left( \frac{\partial \bar{\rho}}{\partial t} \right) - v^2 \nabla^2 \bar{\rho} = \nabla \cdot \mathbf{f}, \quad (1.15 b)$$

where  $\mathbf{f}$  is the force per unit volume, defined by  $\mathbf{f} = -\nabla p_{st}$ . Substituting Eq.(1.13) into the right-hand side of Eq.(1.15 b) and taking into account that the total optical field is  $E(z, t) = E_1(z, t) + E_2(z, t)$  we obtain an equation for the acoustic field:

$$\frac{\partial^2 \rho}{\partial t^2} + (\Gamma_B - i2\Omega_B) \frac{\partial \rho}{\partial t} - i\Gamma_B \Omega_B \rho = \frac{\gamma_e q_B^2}{4\pi} A_1 A_2^*. \quad (1.16)$$

In Eq.(1.15 a) the polarization due to the density change  $\Delta \bar{\rho} = \bar{\rho} - \rho_0$  is  $P = \Delta \chi E = \frac{\Delta \epsilon}{4\pi} E = \frac{\gamma_e}{4\pi \rho_0} \Delta \bar{\rho} E$ . Then under slowly varying amplitude approximation and taking into account the phase-matched terms in the polarization

$$P_1(k_1, \omega_1) = \rho A_2 e^{i(k_1 z - \omega_1 t)} + c.c.,$$

$$P_2(-k_2, \omega_2) = \rho^* A_1 e^{i(-k_2 z - \omega_2 t)} + c.c.$$

the Maxwell's equations for the optical fields are:

$$\frac{n}{c} \frac{\partial A_1}{\partial t} + \frac{\partial A_1}{\partial z} = i \frac{\gamma_e \omega}{2nc\rho_0} \rho A_2, \quad (1.17 a)$$

$$\frac{n}{c} \frac{\partial A_2}{\partial t} - \frac{\partial A_2}{\partial z} = i \frac{\gamma_e \omega}{2nc\rho_0} \rho^* A_1. \quad (1.17 b)$$

Together Eq.(1.16) and Eqs.(1.17 a, 1.17 b) constitute the set of equations describing the electrostrictive SBS process. This set of three coupled nonlinear partial differential equations is difficult to solve in analytical form. In the following several approximations will be made in order to find solutions in the specific case of steady-state. The most interesting case of SBS under transient conditions is the subject of Chapter 3 of this Thesis and will not be discussed in this introductory Chapter.

**Table 1.1:** Properties of stimulated Brillouin scattering for a variety of materials\* after Ref. [5].

Substance	$\Omega_B/2\pi$ (GHz)	$\Gamma_B/2\pi$ (MHz)	$g_B$ (cm/MW)	$g_B^a(max)/\alpha$ (cm <sup>2</sup> /MW)
LIQUIDS				
CS <sub>2</sub>	5.85	52.3	0.15	0.020
Acetone	4.60	224	0.02	0.022
Toluene	5.91	579	0.013	
CCl <sub>4</sub>	4.39	520	0.006	0.013
Methanol	4.25	250	0.013	0.013
Ethanol	4.55	353	0.012	0.010
Benzene	6.47	289	0.018	0.024
H <sub>2</sub> O	5.69	317	0.0048	0.0008
Cyclohexane	5.55	774	0.0068	
GASES				
CH <sub>4</sub> (140 atm)	0.15	10	0.1	
SOLID-STATE MATERIALS				
Optical glasses	11.0 - 16.0	10 - 106	0.004 - 0.025	
SiO <sub>2</sub> **	23.00	26	0.0045	

\*Values are quoted for a wavelength of 694 nm. The last column gives a parameter used to describe the process of absorptive SBS. To convert to other laser frequencies  $\omega$ , recall that  $\Omega_B \sim \omega$ ,  $\Gamma_B \sim \omega^2$ ,  $g_B$  is independent of  $\omega$ , and  $g_B^a$  is proportional to  $\omega^{-3}$ .

\*\*Values from [8], recalculated for 694 nm.

### Steady-state solution (SBS amplifier)

The assumption of steady-state implies no time dependences of the fields (*i.e.*  $\partial A_i/\partial t \equiv 0, i = 1, 2$ ). It is valid only when the temporal variations of the optical fields are on a time-scale much larger than the phonon lifetime  $\tau_p$ . Hence, in case of CW interaction this approximation is fully justified. Using the relation  $I_i = ncA_iA_i^*/2\pi$  Eqs.(1.17 a,1.17 b) are transformed into a set of propagation equations for the intensities:

$$\frac{dI_1}{dz} = -g_B I_2 I_1, \quad (1.18 \text{ a})$$

$$\frac{dI_2}{dz} = -g_B I_1 I_2, \quad (1.18 \text{ b})$$

where  $g_B = (\gamma_e^2 \omega^2)/(nc^3 v \rho_0 \Gamma_B)$  is the steady-state Brillouin gain due to electrostriction. Typical values for the Brillouin shift  $\Omega_B$ , linewidth  $\Gamma_B$ , and steady-state gain  $g_B$  are shown in Table 1.1 for a variety of substances.

The set of ordinary differential equations (1.18 a, 1.18 b) can be easily solved in case

of constant pump intensity (*i.e.* weak conversion). The solution is an exponential growth (in  $-z$  direction) of the Stokes wave injected in the medium at  $z = 0$ :

$$I_2(z) = I_2(0)e^{-g_B I_1 z}. \quad (1.19)$$

In case of anti-Stokes scattering the discussion above can be repeated and leads to the same analytical result, but for a forward-propagating anti-Stokes wave. Hence the anti-Stokes signal experiences attenuation due to the SBS process.

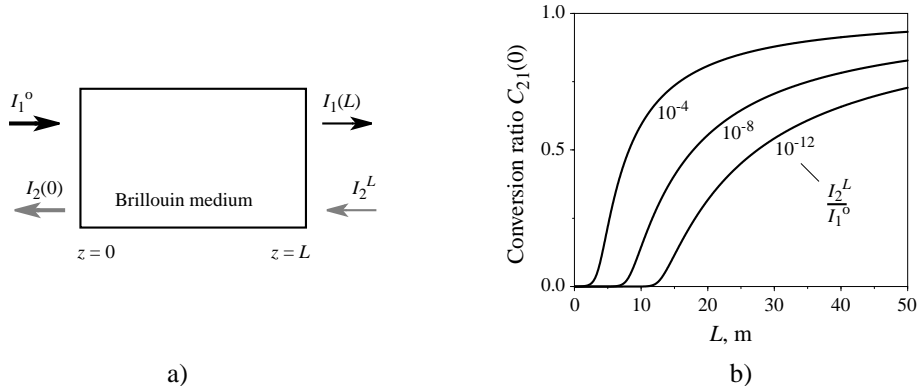


**Figure 1.3:** SBS amplifier; a) - general scheme:  $I_1^0$  and  $I_2^L$  are the boundary conditions, whereas  $C_{21}^0(0) = I_2(0)/I_1(0)$  and  $I_1(L)$  are the solutions; b) - the dependence of the conversion ratio  $C_{21}^0(0)$  on the length of a silica fiber ( $4 \mu\text{m}$  diameter) for different seeding levels and constant (500 mW) pump power.

The assumption of constant pump breaks down in case of strong energy conversion into the Stokes wave [9]. Due to the exponential growth, predicted by Eq.(1.19), the Stokes intensity can become comparable to the pump intensity and pump depletion must be taken into account. Hence, the equations (1.18 a, 1.18 b) have to be solved simultaneously. The solutions with boundary conditions  $I_1(0) = I_1^0$  and  $I_2(0) = I_2^0$  are:

$$I_2(z) = \frac{I_2^0(I_1^0 - I_2^0)}{I_1^0 \exp[g_B(I_1^0 - I_2^0)z] - I_2^0}, \quad (1.20 \text{ a})$$

$$I_1(z) = I_2(z) + I_1^0 - I_2^0. \quad (1.20 \text{ b})$$

These solutions, although mathematically correct, are devoid of physical meaning; the Stokes intensity  $I_2^0$  we have chosen as a boundary condition is not known a priori. A real physical situation with proper boundary conditions is an SBS amplification experiment (*see* Fig. 1.3a), where a weak Stokes wave is injected at the rear end of a Brillouin medium of fixed length  $L$  and its amplification is measured. Hence, the boundary

conditions are  $I_1(0) = I_1^\circ$  for the pump wave and  $I_2(L) = I_2^L$  for the Stokes seed intensity. The unknown variables are the output Stokes intensity  $I_2(0)$  (or the conversion ratio  $C_{21}(0) = I_2(0)/I_1(0)$ ) and the output pump intensity  $I_1(L)$ . From Eqs.(1.20 a, 1.20 b) it follows:

$$I_2^L = \frac{I_1^\circ C_{21}(0)[1 - C_{21}(0)]}{\exp[g_B I_1^\circ L(1 - C_{21}(0))] - C_{21}(0)}, \quad (1.21 \text{ a})$$

$$I_1(L) = I_2^L + I_1^\circ[1 - C_{21}(0)]. \quad (1.21 \text{ b})$$

Eq.(1.21 a) is a transcendental equation for  $C_{21}(0)$ . Its numerical solution in case of silica fiber ( $g_B \approx 5 \times 10^{-3}$  cm/MW) with diameter of 4  $\mu\text{m}$  and 500 mW CW pump power is presented in Fig. 1.3b for different seeding levels  $I_2^L/I_1^\circ$ .

### SBS generator

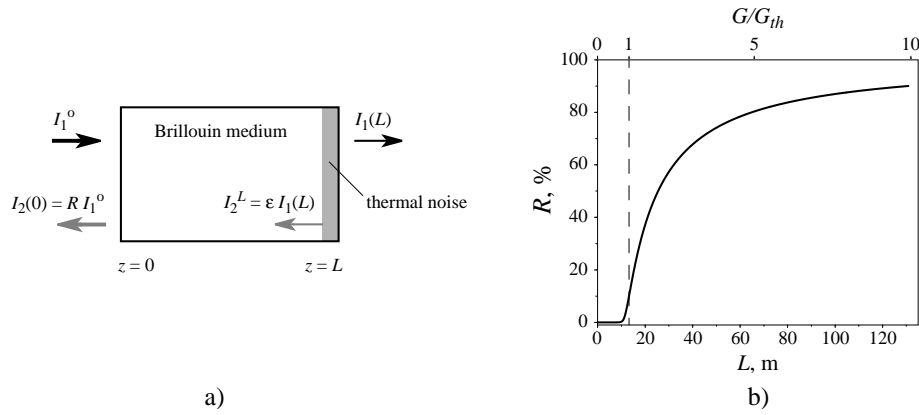


**Figure 1.4:** SBS generator; a) - general scheme; b) - the dependence of the SBS reflectivity on the length of a silica fiber (4  $\mu\text{m}$  diameter) and on the weak-signal gain  $G/G_{th}$  at constant pump power of 500 mW.

When the Stokes signal at the rear end of the medium is not injected from outside, we speak of an SBS generator scheme (see Fig. 1.4a). In this case the spontaneous Brillouin scattering from the thermal noise near  $z = L$  is the source of photons initiating the SBS process. In such experiment we are interested in measuring the reflectivity  $R \equiv I_2(0)/I_1(0)$ , previously defined as the conversion ratio  $C_{21}(0)$ . The equations (1.21 a, 1.21 b) can now be written as:

$$\frac{I_2^L}{I_1^\circ} = \frac{R[1 - R]}{\exp[G(1 - R)] - R}, \quad (1.22 \text{ a})$$

$$I_1(L) - I_2^L = I_1^\circ[1 - R], \quad (1.22 \text{ b})$$

where  $G = g_B I_1^\circ L$  is the gain experienced by the Stokes signal generated at  $z = L$ . Since  $I_2^L$  is essentially a spontaneous scattering signal, Eq.(1.2) can be used in the form  $I_2^L = \varepsilon I_1(L)$ , where  $\varepsilon$  is a factor related to the scattering coefficient (1.1) and its value is of the order of  $10^{-12} - 10^{-11}$ . Under the assumption of low pump depletion (just below threshold) one can use Eq.(1.19) to calculate the amplified spontaneous scattering  $I_2(0) = \varepsilon I_1^\circ \exp[G]$ . Then the reflectivity is  $R = \varepsilon \exp[G]$ . In order to reach threshold for SBS ( $R \approx 1$ ) the pump intensity (when  $L$  is fixed) has to be increased such that the gain  $G$  approaches the value  $G_{th} = -\ln \varepsilon \approx 25$ . By solving Eqs.(1.21 a, 1.21 b) for  $R$  and taking into account the smallness of  $\varepsilon$  we deduce:

$$\frac{G}{G_{th}} = \frac{G_{th}^{-1} \ln R + 1}{1 - R}. \quad (1.23)$$

Eq.(1.23) is a transcendental equation for  $R$  and its solution is shown in Fig. 1.4b in case of 500 mW of CW power entering a single mode silica fiber (4  $\mu\text{m}$  diameter). This example shows that in optical fibers, due to the long interaction length (hundreds of meters and even kilometers), moderate CW powers are sufficient for reaching high reflectivity in steady state SBS generation. The analysis of Eq.(1.23) shows a threshold behavior for the reflectivity  $R$  at  $G/G_{th} = 1$ . For  $G/G_{th} \ll 1$  the reflectivity is  $R = \varepsilon e^G$ , due to amplified spontaneous scattering only. For  $G/G_{th} \gg 1$  (1.23) can be solved for  $R$  yielding:

$$R = 1 - \frac{1}{G/G_{th}}. \quad (1.24)$$

It is clear from (1.24) that in case of high weak-signal gain (long medium, or high input intensity) the reflectivity can become almost unity.

#### *Experimental investigation of SBS*

Stimulated Brillouin scattering was first observed in 1964 in solid-state media (quartz, sapphire) [10], due to the relatively large Brillouin shift compared to liquids or gases (*see* Table 1.1). The experimental setup used by Chiao, Townes, and Stoicheff [10] is shown in Fig. 1.5a, where intense 694 nm radiation from a giant-pulse (Q-switched) ruby laser with a power output of  $\sim 50$  MW during 30 ns was focused inside a crystalline sample. At the focus, assuming no optical distortions, the peak intensity was of the order of  $10^6$  MW/cm<sup>2</sup>. Measurement of the frequency shift of the backscattered signal was done by simultaneous recording the interferograms from two Fabry-Perot interferometers. The lens  $L_1$  collimated the backscattered SBS light. Different laser intensities were sampled by the interferometers using glass-plate beam-splitters and mirrors  $M_1$ ,  $M_2$  having reflectivities 1 and 0.1, respectively. Thus comparing the two interferograms, photographed simultaneously, the radiation coming from the laser and the light scattered from the sample can be clearly distinguished.

A comparison of the two interferograms in Fig. 1.5b, taken with a single laser pulse, made it evident that the inner rings originated from stimulated Brillouin scattering,

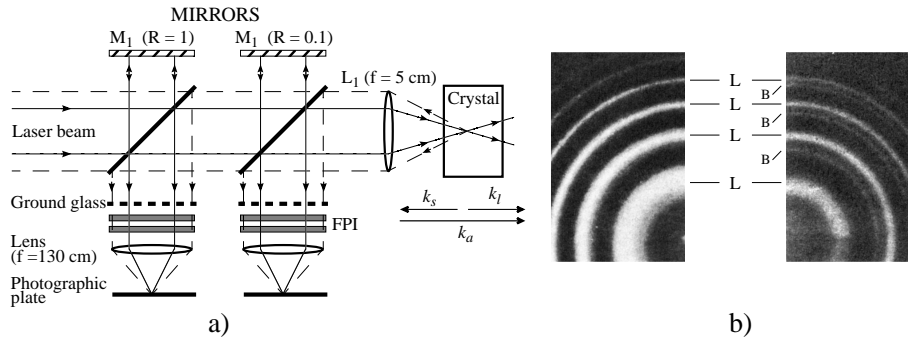


**Figure 1.5:** First experimental observation of stimulated Brillouin scattering [10]; a) - schematic of the experimental arrangement, b) - Fabry-Perot interferograms of the laser radiation (rings labeled L) and of the Brillouin scattered radiation (rings labeled B).

hence identified by B, whereas the rings created by the laser frequency were labeled L. It could also be seen that the Brillouin scattering was very intense, being comparable in intensity with the incident light; a clear signature of a stimulated process. The frequency shift measured on a  $3.15 \text{ cm}^{-1}$  inter-order separation interferometer was approximately 30 GHz. In this first experimental study of SBS quartz and sapphire samples were investigated and the results from the Brillouin shift measurements were compared with theoretical predictions as well as experimental results on spontaneous Brillouin scattering found in Ref. [11].

Apart from the first observation of SBS, the experiment discussed above showed the inapplicability of bulk solid-state materials for reliable long-term operation as SBS generators. Each laser pulse caused extensive internal fracture in the crystal, attributed to the high local stress produced by the intense acoustic wave, in combination with heating resulting from damping of the acoustic oscillations. The latter type of heating is appreciably larger than that due to optical absorption.

The undesirable effect of crystal fracture due to the intense acoustic waves directed the attention towards liquids and gases. In the same year 1964 Garmire and Townes [12] published the results of SBS experiment in liquids. Due to the specifics of their experimental setup, (see Fig. 1.6a), they could observe multiple Stokes frequencies. The incident light was provided by a giant-pulse (Q-switched) ruby laser with a mode-selector plate, ensuring narrow-band ( $0.04 \text{ cm}^{-1}$ ) operation. Liquids were placed in a cell at or near the focal plane of a lens, and the frequencies near  $694.3 \text{ nm}$  were studied with a Fabry-Perot interferometer, placed at sites A, B, or C. Fig. 1.6b shows a typical interferometer pattern, which was generally the same at sites A and C. The multiple Brillouin components seen in Fig. 1.6b were amplified in the same ruby laser crystal. The light follows the path indicated with arrows in Fig. 1.6a and the width of the dashes represents

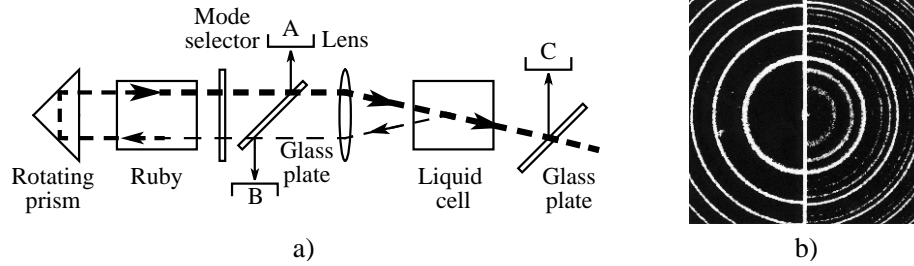


**Figure 1.6:** Higher order SBS experiment in liquids [12]; a) - experimental setup; b) - Fabry-Perot interferograms from site A with water in the liquid cell. Left: below threshold for SBS. Right: above threshold with three Brillouin components in addition to the original laser frequency.

the intensity of the light. The intensity at site B was too weak to be detected. Since the Brillouin shift for most liquids is around  $0.2 \text{ cm}^{-1}$ , a number of orders were covered by the gain curve of the ruby and were amplified. If the observed effect would have been multiple scattering, one would have expected alternating orders in opposite directions (see Chapter 4 of this Thesis), which does not occur under sharp focusing because of the short interaction length. The threshold for the SBS process investigated in this experiment using a 17 cm lens was  $30 \text{ MW/cm}^2$  for carbon-disulfide, while for benzene and other liquids it was approximately  $1200 \text{ MW/cm}^2$  (see Table. 1.1 for respective gain values). Competition with stimulated Raman scattering (SRS) was also observed in liquids with high Raman gain ( $\text{CS}_2$ , nitrobenzene, toluene, benzene, and acetone), whereas at the same powers no SRS was detected in water,  $\text{CCl}_4$ , and methanol.

In the same investigation [12] the authors calculated accurate values for the acoustic wave velocities in a number of liquids on the basis of the frequency-shift measurements. Their results were in agreement with the values, calculated from spontaneous Brillouin spectra, found in Ref. [13]. It was suggested by Wiggins *et al.* [14] that the high gain in the laser could shift the frequencies of the Stokes orders being amplified, thus introducing an error in the frequency measurements. Despite this uncertainty, there was a great interest in the possibility to generate many Stokes components. In further works [15,16], using high resolution grating spectrograph it was discovered, that at high pump energies there were greater number of Stokes-shifted components than can be accounted for on the basis of successive amplification in the laser; a number of anti-Stokes shifted frequencies were observed as well. 15 anti-Stokes and 30 Stokes components were recorded in these experiments. Four-wave-mixing in the focal region was considered as the most probable explanation for the effect observed. A full account on all possible processes, which could lead to anti-Stokes scattering was made by Goldblatt and Hercher [17]. Apart from four-wave-mixing involving forward propagating Stokes orders with comparable intensity, they discussed processes involving window reflection of the first Stokes or of

the laser frequency, and even Rayleigh scattering as a source of backward propagating fundamental frequency, which interacting with the forward-propagating phonons could lead to anti-Stokes scattering. Kyzylasov and Starunov [18] suggested that the interplay between SBS and stimulated Rayleigh-wing scattering (SRwS) could generate high order side-bands as well. In their experiment the SBS was excited in quartz. The output radiation, containing both the fundamental and one Stokes frequency (characteristic for quartz) was focused into a cell, containing  $\text{CS}_2$ . Behind the cell the spectrum was analyzed using either a Fabry-Perot interferometer or a grating spectrograph. The authors observed 3 anti-Stokes and up to 9 Stokes components and attributed this result to amplification through SRwS.

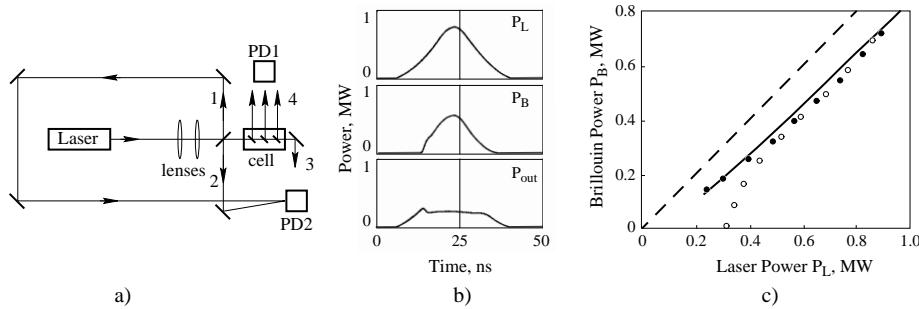


**Figure 1.7:** SBS experiment in the time domain [24]; a) - experimental setup, b) - oscilloscope traces of the laser power  $P_L$ , the SBS power  $P_B$ , and the transmitted laser power  $P_{out}$  in ethyl ether; c) - instantaneous Brillouin power  $P_B$  versus rising ( $\circ$ ) and falling ( $\bullet$ ) instantaneous laser power  $P_L$  in a cell of 50 cm length filled with ethyl ether. The solid line is a calculation, while the dashed line represents 100% conversion efficiency.

After these first experiments focusing on the spectral properties of the SBS signal many more experiments were performed in other solids, liquids [19–24] and gases [25, 26]. One of the first measurements of the temporal and spatial distribution of the scattered signal and Brillouin gain within a cell filled with liquid was presented in 1968 by Maier [24]. In the experimental setup shown in Fig. 1.7a, the laser pulses were provided by a giant-pulse (Q-switched) ruby laser delivering maximum output power of 1 MW, in a nearly Gaussian beam with diameter of 2 mm, and divergence of 1 mrad. A telescope was used to increase the intensity by a factor of 9. After a small (0.5 mm diameter) diaphragm an intense collimated beam was obtained, which entered a cell filled either with ethyl ether, n-hexane, or  $\text{CS}_2$ . A glass plate was used to couple out light from the laser (1 in Fig. 1.7a) and from the backscattered signal (2). The light transmitted through the Brillouin cell (3) was also detected. A movable glass plate immersed in the liquid coupled out the backscattered light at different positions in space (4). The temporal resolution of the detection system was limited by the oscilloscope

rise-time of 300 ps. A large distance between the laser and the liquid cell eliminates multiple scattering amplified in the laser rod.

The experimental setup described above allowed the author to create experimental conditions very close to the theoretically assumed ones for steady-state SBS generator. The results from quantitative time resolved measurements of the laser power  $P_L$ , Brillouin power  $P_B$ , and the transmitted laser power  $P_{out}$  are presented in Fig. 1.7b. It is clearly seen that the instantaneous Brillouin power  $P_B$  after initial exponential growth reaches steady-state and follows closely the pump pulse power distribution  $P_L$  with high conversion efficiency. The transmitted power  $P_{out}$  was strongly attenuated at the onset of SBS. The points obtained from the continuous curves of Fig. 1.7b at different times are shown in Fig. 1.7c. The open circles ( $\circ$ ) represent the rising part of the laser pulse, whereas the full ones ( $\bullet$ ) are measured in the falling part of the pump. The application of the steady-state theory Eqs.(1.22 a, 1.22 b) explains well the data (the solid curve in Fig. 1.7c).

Measurement of the  $z$ -dependence of the instantaneous Brillouin power  $P_B(z)$  yielded experimental values for the weak-signal gain  $G \simeq 30$  for both n-hexane and ethyl ether. Only in the case of  $CS_2$  the values obtained were somewhat lower  $G = 15 - 25$ , a discrepancy attributed to the self-focusing taking place before the onset of SBS, thus initiating the process at lower value of the weak-signal gain.

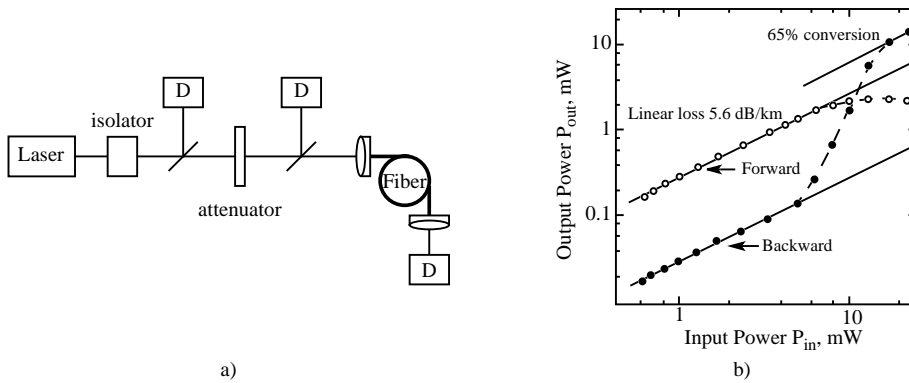


**Figure 1.8:** SBS in optical fibers [28]; a) - experimental setup, b) - transmitted ( $\circ$ ) and reflected ( $\bullet$ ) powers as a function of the input power launched into a 13.6 km long single-mode fiber.

It was not before the development of optical fibers in the early 1970s when SBS was studied for the first time in guided geometry. Pulsed lasers were employed in the beginning, when the production technology was not mature enough and the maximum interaction length was limited by the extremely large losses, typically  $\approx 1300$  dB/km. Ippen and Stolen [27] used a pulsed xenon laser at 535.5 nm as a pump source and fibers of 5.8 m and 20 m length and  $13.5 \mu m^2$  cross-section, measuring threshold powers of

2.3 W and 1 W, respectively. The results of this experiment were in excellent agreement with the steady-state theory of SBS generator, discussed above. The threshold power in case of optical fibers can be calculated according to:

$$P_{th} = \frac{G_{th} A_{eff}}{g_B L_{eff}}, \quad (1.25)$$

where  $A_{eff}$  is the effective fiber cross-section and  $L_{eff} = \alpha^{-1}[1 - \exp(-\alpha L)]$  is the effective interaction length of fiber with length  $L$  and losses  $\alpha$ . The Brillouin shift  $\Omega_B = 32.2$  GHz, measured in Ref. [27] also agreed with the value known for bulk silica.

As fiber technology improved in the 1980s, losses as low as 4 dB/km were achieved in single-mode fibers in the visible. The threshold powers, according to Eq.(1.25) decreased and SBS became accessible for CW lasers. An example of such experiment is shown in Fig. 1.8a where a CW Nd:YAG laser at  $1.32 \mu\text{m}$ , a wavelength of interest for optical fiber communications, was used to produce powers up to 30 mW with 1.6 MHz linewidth [28]. The fiber was 13.6 km long with 0.41 dB/km loss, resulting in an effective length  $L_{eff} = 7.66$  km. The optical isolator prevented the backscattered light from entering the laser. Both transmitted and reflected powers were measured simultaneously at different pump levels. The results are presented in Fig. 1.8b where transmitted power is depicted by open circles ( $\circ$ ), while the reflected power by full ones ( $\bullet$ ). At low input powers the reflected light was simply the 4% reflection from the fiber tip. The Brillouin threshold was reached at an input power of about 5 mW as manifested through the substantial increase in the reflected power, dominated by the backward Stokes generated through SBS. The transmitted power was then depleted and reached saturation level of 2 mW for input power in excess of 10 mW. The SBS reflectivity approached 65%.

As clearly demonstrated, the narrow-band power transmission through optical fibers can be undermined by the SBS process at power levels of the order of tens of milli-Watts for several kilometers long connections. In case of usual laboratory connection of  $\approx 20$  m length the threshold is as low as 500 mW for narrow-band input light.

## 1.2 Applications of SBS

### 1.2.1 Phase conjugation by SBS

Optical phase conjugation is one of the most interesting topics in nonlinear optics [29–31] and probably the most widely used application of SBS. From a mathematical point of view it is the process of creating from an incident optical field

$$\tilde{E}_0(\mathbf{r}, t) = E_0 \epsilon_0 e^{i(\mathbf{k}_0 \cdot \mathbf{r} - \omega_0 t)} + \text{c.c.} \quad (1.26)$$

the wave, complex conjugate of  $\tilde{E}_0$  in the spatial properties:

$$\tilde{E}_c(\mathbf{r}, t) = E_0^* \epsilon_0^* e^{i(-\mathbf{k}_0 \cdot \mathbf{r} - \omega_0 t)} + \text{c.c.} \quad (1.27)$$

In Eqs.(1.26,1.27)  $\mathbf{k}_0$  is the wave-vector of the incident wave,  $\omega_0$  is its carrier frequency, and  $\epsilon_0$  is the polarization vector. It is seen, that the spatial phase conjugation (1.27) is

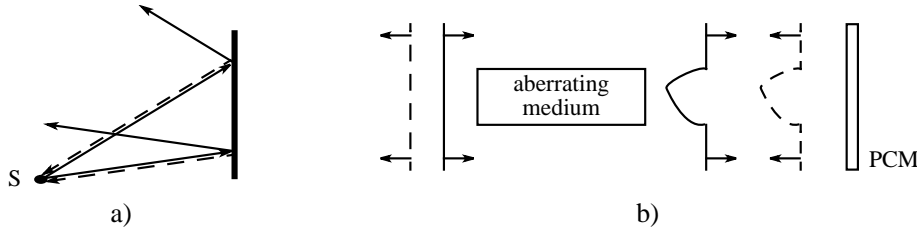


**Figure 1.9:** Optical phase conjugation; a) - comparison between the reflection on a conventional (solid line) and a phase-conjugate mirror (dashed line) of the light emitted from a point source S; b) - wave-front correction by phase-conjugate mirror (PCM).

in fact equivalent to time reversal  $\tilde{E}_c(\mathbf{r}, t) = \tilde{E}_0(\mathbf{r}, -t)$ , i.e. the conjugate wave travels exactly as if it were seen on a backward motion picture.

In order to clarify the action of a phase conjugation device let us consider a mirror, reflecting the light emitted from a point source (Fig. 1.9a). If the reflection were from a conventional mirror the rays would follow the path, depicted by the solid arrows in Fig. 1.9a. In case of a phase conjugate mirror (PCM), upon reflection the rays follow the dashed arrows ( $\mathbf{k}_c = -\mathbf{k}_0$ ), converging at the source S. The action of a perfect phase conjugate mirror is in fact threefold [5]:

*i* -  $E_0$  is replaced by  $E_0^*$ , hence the wavefront is reversed;

*ii* -  $\mathbf{k}_c = -\mathbf{k}_0$ , hence the direction of propagation is reversed;

*iii* - the polarization vector of the outgoing wave is the complex conjugate of  $\epsilon_0$ . The physical consequence of this mathematical representation along with *ii* is that right-hand circularly polarized light remains right-hand circularly polarized upon reflection from a PCM, unlike the reflection from a conventional mirror. The linear polarization state is conserved.

One prominent application of PCM is in correcting wavefront distortions as shown in Fig. 1.9b. The wavefront of a plane wave after passing through an aberrating medium<sup>b</sup> is distorted. Upon reflection from a PCM the reversed wavefront, depicted with a dashed line in Fig. 1.9b, passes again through the same medium. The initial flat wavefront is restored, due to the canceling effect of the aberration acting on the phase conjugate wavefront [32].

There are two processes widely used for generation of phase-conjugate waves: degenerate four-wave mixing and stimulated Brillouin scattering. The degenerate four-wave mixing (DFWM) is often used for its nearly perfect phase conjugation fidelity and the possibility of phase conjugating weak signals [33–35]. The scheme of phase conjugation by DFWM is shown in Fig. 1.10a. The four interacting waves all have the same frequency. If the two pump waves ( $\tilde{E}_1$  and  $\tilde{E}_2$ ) are phase conjugate of one another (for

<sup>b</sup>The thermal lensing effect in powerful amplifier systems is a typical example of aberrating medium, where PCM is used for wavefront correction.

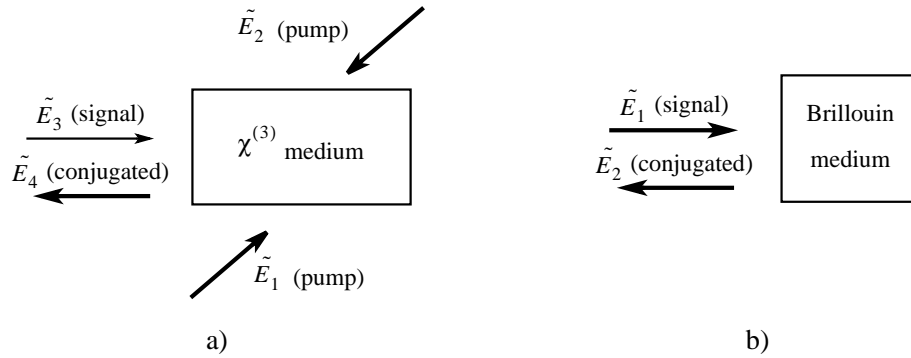


**Figure 1.10:** Phase conjugation; a) - by degenerate four-wave mixing, b) - by SBS.

instance plane waves), the outgoing wave  $\tilde{E}_4$  is phase conjugate to the signal wave  $\tilde{E}_3$ . The phase-matching of the process requires  $\mathbf{k}_1 = -\mathbf{k}_2$  and  $\mathbf{k}_3 = -\mathbf{k}_4$ , thus satisfying condition *ii* for phase conjugation. It can be shown [36] that the evolution of the slowly-varying amplitude  $A_4$  of the output wave  $\tilde{E}_4$  is governed by  $dA_4/dz = -i\kappa A_3^*$ , where  $\kappa = 12\pi\omega A_1 A_2 / (nc)$ . Hence, conditions *i* and *iii* are fulfilled as well. The first experimental realization of phase conjugation by DFWM was reported in 1977 [35]. The authors used  $\text{CS}_2$  as  $\chi^{(3)}$  nonlinear medium and a conventional mirror to create the two plane counter-propagating pump waves  $\tilde{E}_1$  and  $\tilde{E}_2$ .

In Fig. 1.10b the scheme of PCM, based on stimulated Brillouin scattering is presented. However, from the equations governing the process of SBS and described in the preceding section it is not clear why the scattered signal  $\tilde{E}_2$  should be phase conjugate of the incident wave  $\tilde{E}_1$ .

The observations in the early experiments on SBS showed that the backscattered light followed very closely the path of the pump beam, an effect initially attributed to the geometry of the interaction. It was not before 1972 when it was realized for the first time that under proper conditions the Stokes wave in SBS was indeed phase conjugate. Zel'dovich *et al.* [37] performed the experiment, shown in Fig. 1.11a where the beam from a Q-switched ruby laser was aberrated by means of an etched glass plate (A) and subsequently focused into a methane filled cell. Both the Stokes and the laser beams were monitored on photo cameras. The results are presented in Fig. 1.11b. Photo 1 was the laser beam profile of divergence  $0.14 \times 1.3$  mrad, whereas 2 was the backscattered beam. The perfect wavefront reconstruction is evident. However, if the beam was not initially aberrated, camera 1 recorded the beam profile 3, which did not reproduce the pump beam. When the methane cell was replaced by a conventional mirror with aberrator inserted, camera 1 recorded a large spot of the aberrated laser beam. On the basis of these observations the authors came to the conclusion that the aberrated beam was better phase conjugated than the unaberrated one; a conclusion which reflects the fact that phase conjugation is not an inherent property of the SBS process.

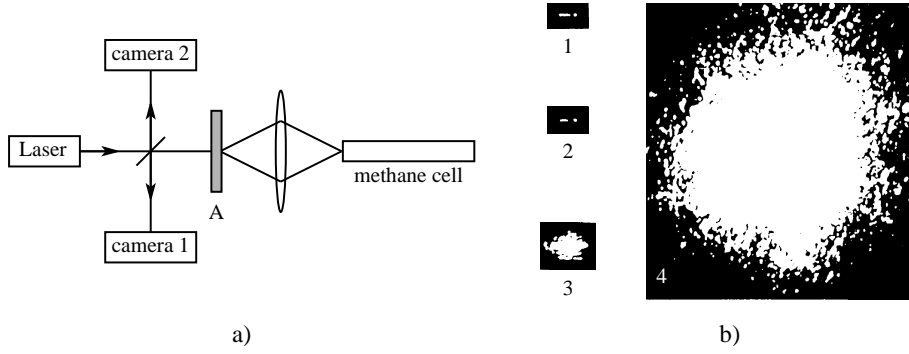


**Figure 1.11:** Phase conjugation with SBS [37]; a) - experimental setup, b) - beam profiles recorded in the experiment (*see* the text).

In the focal region of a lens the aberrated beam creates highly inhomogeneous intensity distribution (volume speckle pattern). Since the local gain of the SBS process is huge and depends on the local intensity, the volume gain distribution will follow the nonuniform pump distribution and will transfer into the Stokes field only this part of the spontaneous noise whose wavefront matches exactly the incident wavefront (condition *i*). The condition *ii* is automatically fulfilled for SBS, due to its backscattering gain. Only condition *iii* cannot be satisfied in all cases.

The polarization properties of SBS become clear analyzing Eqs.(1.16, 1.17 a, and 1.17 b). The driving term in the Navier-Stokes equation (1.16) is  $\mathbf{A}_1 \mathbf{A}_2^*$ . It is the interference between  $\mathbf{A}_1$  and  $\mathbf{A}_2^*$  which through electrostriction creates the acoustics field. Since the disturbance of the density  $\Delta \bar{\rho}$  is a scalar, then the change in the dielectric constant is of scalar nature and the response of the medium at the Stokes-shifted frequency is:

$$\frac{d\mathbf{A}_2}{dz} = \frac{1}{2} G \mathbf{A}_1 (\mathbf{A}_1^* \cdot \mathbf{A}_2). \quad (1.28)$$

Let us consider two orthogonal polarizations  $\mathbf{e}_1$  and  $\mathbf{e}_2$ . If the laser is linearly polarized along  $\mathbf{e}_1$  ( $\mathbf{A}_1(z) = \mathbf{e}_1 A_1(z)$ ) and the Stokes has in general arbitrary polarization  $\mathbf{A}_2(z) = s_1(z)\mathbf{e}_1 + s_2(z)\mathbf{e}_2$ , Eq.(1.28) has the solution:

$$\mathbf{A}_2(z) = s_2(0)\mathbf{e}_2 + s_1(0)e^{gz/2}\mathbf{e}_1, \quad g = G|A_1|^2. \quad (1.29)$$

This means that the component  $s_2\mathbf{e}_2$  orthogonal to the laser polarization is not amplified, whereas the component  $s_1\mathbf{e}_1$  experiences all the gain. Therefore, SBS being scattering from a scalar field, does not alter the polarization state of the wave and acts as a conventional mirror for polarization. Right-hand circularly polarized pump beam is converted into left-hand circularly polarized Stokes beam, thus violating condition *iii* and resulting in an imperfect phase conjugation for any other polarization than linear.

This fact makes it possible to fully separate circularly polarized laser beam from the phase conjugate Stokes one on the basis of their different polarizations (*see* Chapter 2).

### 1.2.2 Pulse compression by SBS

The idea of compressing laser pulses in the course of stimulated backscattering dates from the late 1960s when experiments on pulse compression in traveling-wave Raman amplifiers were conducted by Maier *et al.* [38] and many others [39–41]. It was noted that backward Raman scattering could efficiently compress (50 - 70%) a seeded weak Stokes pulse, thus producing an intense short pulse with duration limited by the decay time of the vibrational excitation in the medium (of the order of pico-seconds). This efficiency, combined with powerful excimer lasers (typically KrF at 248 nm), was used in attempts to create high-peak intensity short ultraviolet pulses for laser assisted nuclear fusion experiments [42, 43]. After nearly a decade of development the idea was abandoned due to complications arising from competing nonlinearities (two-photon absorption, optical breakdown, and self-focusing) and most notably the generation of super-fluorescent second Stokes radiation during the compression process.

The possibility to compress pulses by means of stimulated backscattering is not restricted to Raman scattering only. It was theoretically predicted for SBS as well, but it was not before 1980 when the first experimental demonstration was reported by Hon [44]. The use of SBS offers several potential advantages [45] over compressor systems based upon stimulated Raman scattering (SRS). Firstly, the production of second Stokes is not a serious problem, because SBS occurs only in backward direction, unlike SRS where the forward gain is usually stronger than backward [42]. Tapered waveguide geometry was used in the first experiments in order to keep the peak intensity of both the pump and Stokes pulses below threshold for second backward Stokes generation. Secondly, the quantum efficiency of the SBS process is almost 100% since the Stokes frequency  $\omega_s$  is approximately equal to the laser frequency  $\omega_L$ . Thirdly, the fact that the SBS is initiated from spontaneous scattering avoids the necessity of injection of weak Stokes pulse as required in SRS based compressors. Fourthly, since the Stokes beam under proper conditions is the phase conjugate of the input beam, compensation for inhomogeneities automatically takes place.

In Hon's experiment [44] a 20 ns pulse with 200 mJ pulse energy from a single-longitudinal mode Nd:YAG laser was directed into a 1.3 m long tapered glass-tube placed inside a methane cell, pressurized at 120 atm. The pulses, detected on a fast photo-diode and 500 MHz oscilloscope are shown in Fig. 1.12a. The "Input 1" and "Throughput" stand for the laser pulse of 20 ns duration and the transmitted part of the pump after the wave-guide, respectively. The sudden drop of the throughput is a signature of the onset of SBS. Up to 70% conversion was achieved in this experiment. The compressed phase conjugate pulse (denoted by "SBS 1" in Fig. 1.12a) consists of a spike of  $2 \pm 0.5$  ns duration (approximately 10 times as short as the pump pulse) followed by a tail, closely reproducing the laser-pulse profile. After allowing the backscattered pulse to enter the laser and to be amplified ("Input 2") it was again directed into the wave-guide for second compression. The compressed pulse ("SBS 2") was a single pulse of  $\sim 2$  ns duration; a

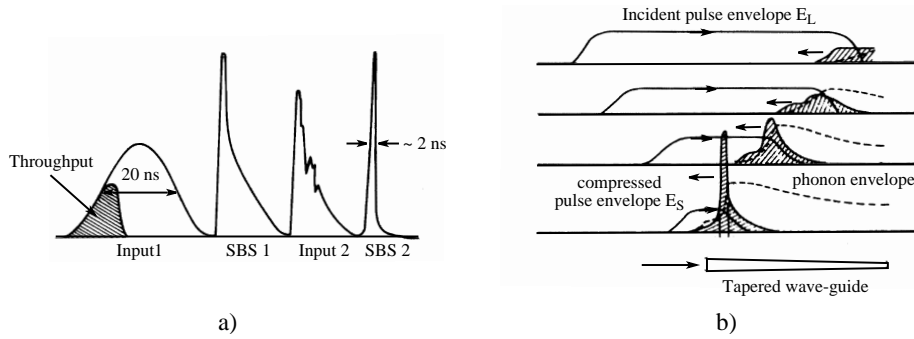


**Figure 1.12:** Pulse compression by SBS [44]; a) - Input, throughput, and SBS signals in two-step pulse compression; b) - Time sequence of SBS compression of a square incident pulse in a tapered wave-guide.

compression ratio of 10 was achieved. The odd shape of the amplified compressed pulse (“Input 2”) was attributed to the fact that the Brillouin-shifted frequency of “SBS1” did not match any of the longitudinal modes of the laser. It was the short coherence length of “Input 2” which was probably responsible for the low conversion efficiency in the second compression.

For better understanding the evolution of the interaction leading to pulse compression, the time sequences containing the three interacting fields (laser, Stokes, and acoustic) are presented in Fig. 1.12b. Here we quote the original paper [44], containing the following explanation: “As the SBS pulse, created by the leading edge of the pump pulse sweeps backward, it beats with the remainder of the incident wave to create a strong acoustic wave (with  $q_B \sim 2k_L$  and  $\Omega_B \sim 2n\omega_L v/c$ ), which in turn acts as a bulk grating to reflect the incident wave further to strengthen the SBS wave coherently . . . It is postulated that the leading edge of the phonon envelope forms the mirror that reflects and, owing to its growing reflectivity, compresses the pulse”.

There are two important characteristics in the pulse compression process: the compression ratio  $\tau_{in}/\tau_{out}$  and the energy conversion efficiency  $E_{in}/E_{out}$ , where  $\tau$  and  $E$  stand for pulse duration and energy in the pulse, respectively, whereas the sub-script *in/out* refers to laser/Stokes. In a tapered waveguide, both the compression ratio and the reflectivity can be controlled by either changing the degree of the taper or by gain saturation that tends to sharpen the leading edge of the pulse as it is amplified [45]. The energy conversion efficiency is generally somewhat less than 100%, principally due to the initial build-up of the Stokes pulse from noise, during which time the laser pulse passes out of the guide with low depletion. To increase the conversion efficiency at high input powers a sharp focusing in a cell (generator) is usually used, preceded by a long cell (amplifier), where the actual compression takes place (see Fig. 1.13a). In the focal region of the lens L the very leading part of the front edge of the pump pulse generates

the Stokes pulse which, being phase conjugate of the pump, sweeps backwards through the amplifier cell depleting the laser pulse. Using a two-cell generator-amplifier setup [46] both high conversion efficiency and high compression ratios have been achieved [47–49] (*see also* Chapter 2 of this Thesis).

Competing nonlinear processes in the generator cell inevitably limit the scalability of the two-cell SBS pulse compressor to higher powers. To avoid this constraint a modification has been suggested in Ref. [47] where a small portion of the pump beam is directed into the generator cell, while the remainder of the laser pulse is used to pump the amplifier cell. Up to 25 J energy in 15 ns was compressed to 600 ps applying such modification.

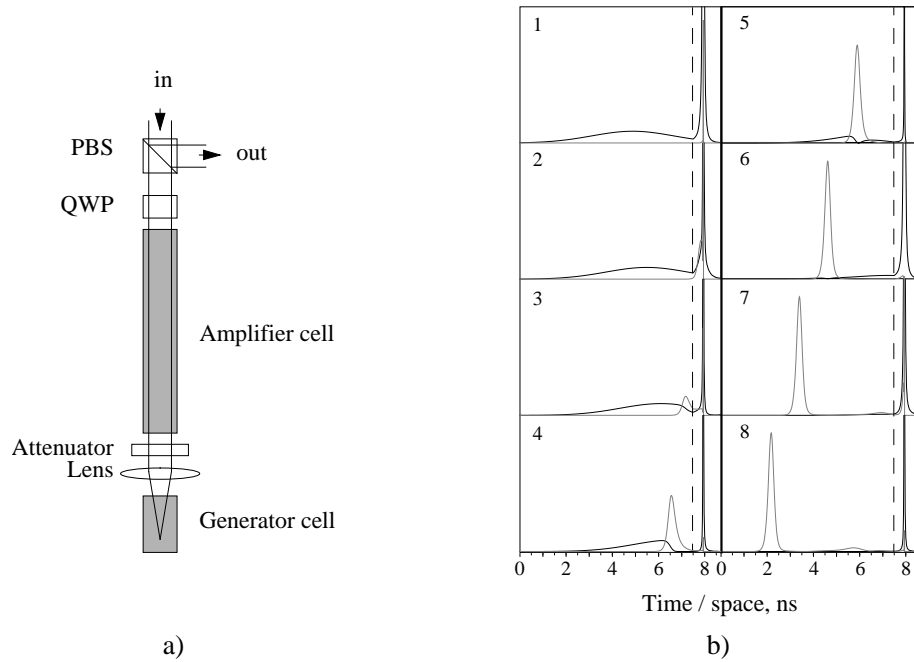


**Figure 1.13:** Two-stage generator-amplifier setup; a) - Experimental arrangement: PBS - polarization beam-splitter, QWP - quarter-wave plate; b) - A time sequence of the modeled pulse compression by SBS in focusing geometry. The evolution stages of the compression follow the Arabic numerals.

Modeling of the SBS compression, involving transient effects [50] (*see also* Chapter 3 of this Thesis), results in the evolution, presented in Fig. 1.13b. The input pulse is of 5 ns duration and 300 mJ energy (typical output of a commercially available injection seeded Q-switched Nd:YAG laser), propagating through water as a Brillouin medium is focused by a lens ( $f = 10$  cm). The lens's position in space is depicted by a dashed line. The

laser pulse is drawn in black, whereas the Stokes pulse is in gray throughout all stages in Fig. 1.13b. In stage 1 the leading edge of the laser pulse has already entered the focal region, which results in very high peak intensity at the focal plane of the lens. A narrow, intense Stokes signal is therefore generated. Being phase conjugate it follows the path of the pump-pulse and in stage 3 it has passed the lens and has entered the amplifier region. Its peak intensity at that moment is higher than the intensity of the pump pulse and, as seen in stage 4, after the peak of the Stokes pulse the pump pulse is fully depleted, thus providing no gain for the trailing edge of the Stokes. As a consequence, only the leading edge of the Stokes pulse is amplified and at the end of the interaction it is effectively compressed. The output pulse duration in this case is  $\sim 300$  ps (compression ratio of 17) and the energy conversion efficiency is  $\sim 98\%$ . If we recall that the phonon life-time in water at 532 nm is  $\tau_p = 295$  ps a conclusion can be drawn, that the pulse compression is limited by the phonon lifetime itself. In most of the experimental realizations of pulse compression this is indeed true. By changing the pump energy or by modifying the geometry of the experiment, one can tailor the compressed pulse duration over a wide range [51]. The possibility for SBS pulse compression below the phonon lifetime limit is discussed in Chapter 3 of this Thesis.

### 1.2.3 Other applications

#### *Brillouin-enhanced-four-wave mixing*

One of the main advantages of phase conjugation by degenerate four-wave mixing (DFWM) over SBS phase conjugation is the possibility of conjugating weak beams; the possibility to produce *in principle* infinitely large reflectivity. In *practice* the experimental realizations rarely reach 100. This is because the conditions required to achieve high reflectivities are extremely precise; in experiments involving real Gaussian beams it is not possible to achieve these conditions with sufficient precision [52].

The Brillouin-enhanced four-wave mixing (BEFWM) is a form of nearly-degenerate four-wave mixing in which the four beams are coupled by the Brillouin nonlinearity [53]. The incoming signal beam has a Brillouin frequency-shift with respect to one of the pump beams in a geometry, similar to the one drawn in Fig. 1.10a, so that the interference pattern they produce moves at acoustic velocity and drives an acoustic wave. This scatters the second pump beam to form the conjugate beam. High reflectivity ( $\sim 10^6$ ) can experimentally be achieved by BEFWM phase conjugation. This is because the reflectivity results from an instability in which the conjugate intensity grows exponentially in time until pump beam depletion prevents further growth. Providing that the pump beams exceed a certain critical intensity, it is found that whatever the strength of the input signal the conjugate intensity will grow until the pump beams are significantly depleted. It can be shown, that maximum conjugate power is obtained if an anti-Stokes signal creates a Stoke conjugate, while the minimum signal requirement is achieved if a Stokes-shifted signal is used.

The first experimental realization of BEFWM using two pumps of the same frequency and a suitable Brillouin-shifted signal beam was reported in 1980 by Bepalov *et al.* [54]

who achieved reflectivity of the order of 20. High reflectivity BEFWM conjugation was reported soon after by Andreev *et al.* [55] with a value of  $7 \times 10^5$  measured.

BEFWM has got many applications ranging from phase conjugating and amplifying very weak signals ( $\approx 4 \times 10^{-17}$  J) [56] to phase locking of laser beams [57]. The latter is used for vector phase conjugation [58, 59] and beam combination [60, 61]. As discussed above, the phase conjugation by SBS is a scalar phase conjugation, for it does not conjugate the polarization state. In addition, conventional SBS has a random overall phase that can fluctuate in time. It is possible to split a beam into two orthogonal polarizations, conjugate each using scalar phase conjugation, and recombine them such that they emulate vector phase conjugator. This can only be achieved if the phases of both beams are locked together [58]. BEFWM can be successfully used as a phase controlled scalar conjugator, since in this scheme the conjugate signal does not build up from noise, thus retaining a control over its phase via the characteristics of the pump beams.

### *Brillouin fiber-lasers and mode-locking*

The Brillouin gain can be used to make Brillouin lasers by placing the Brillouin medium inside a cavity [62]. The gain of the order of  $5 \times 10^{-3}$  cm/MW requires long interaction length in order to achieve oscillation. This can be easily done in optical fibers, where the pump and the Stokes can propagate together for a long distance. Both ring-cavity and linear configurations have been demonstrated so far. Linear cavity fiber-lasers exhibit features qualitatively different from those in ring configuration, because of the simultaneous propagation of pump and Stokes waves in both directions. Through cascade SBS multiple Stokes orders are generated, whereas four-wave mixing is responsible for anti-Stokes generation. The output of such a laser consists of many Stokes and anti-Stokes frequencies, whose number depends on the pump power. In one experiment [63] up to 14 spectral lines were observed, 10 of which on the Stokes side, in a 20 m long fiber inside a Fabry-Perot cavity pumped by a CW argon-ion laser at 514.5 nm.

The simultaneous presence of many spectral lines in the output of the Brillouin fiber-laser offers the possibility to obtain ultrashort pulses, provided the laser can be mode-locked. This idea was investigated in the 1970s, but unfortunately the outcome was not encouraging. Partial mode-locking was observed by Kawasaki *et al.* [64], but the process turned out to be not very stable. This can be understood if we recall the frequency dependence of the Stokes shift  $\Omega_B = 2\omega_0 nv/c$ , which implies that higher-order Stokes frequencies, being pumped by waves at different wavelengths will be shifted differently. As a result the cascaded SBS will not produce equidistant modes and the SBS mode-locking will not be stable. For more qualitative analysis let us calculate the set of frequencies, generated in a cascaded SBS and compare them to an equidistant comb of frequencies  $\bar{\omega}_m = \omega_0 - m\Omega_B$  which would be produced by an ideal mode-locked laser. Since the Stokes shifts are not identical for each order, the set of frequencies is:

$$\omega_m = \omega_0 - \sum_{j=0}^{m-1} \Omega_j,$$

where  $\Omega_j = 2\omega_j nv/c$  is the Stokes shift when pumping with frequency  $\omega_j$ . Taking into account the relations:

$$\Omega_j = 2(\omega_{j-1} - \Omega_{j-1})nv/c = \Omega_{j-1} \left(1 - \frac{2nv}{c}\right) = \Omega_B \left(1 - \frac{2nv}{c}\right)^j.$$

The Stokes shifts form a geometrical progression, while the Stokes orders are partial sums over the elements of this progression. The shift of the  $m$ -th Stokes frequency  $\omega_m$  from its ultimate position for mode-locking  $\bar{\omega}_m$  then is:

$$\Delta\omega_m = \omega_m - \bar{\omega}_m = \Omega_B \left[ m - \sum_{j=0}^{m-1} \left(1 - \frac{2nv}{c}\right)^j \right] \approx m(m-1)\Omega_B \frac{nv}{c} + \mathcal{O}_2 \left(\frac{2nv}{c}\right).$$

If  $m$  is large enough,  $\Delta\omega_m$  can become greater than the Brillouin linewidth  $\Gamma_B$ , hence no mode-locking can occur for order numbers higher than  $m$ . Calculating the number of orders which can be efficiently mode-locked in case of silica fiber with  $\Omega_B/2\pi = 31.6$  GHz,  $\Gamma_B/2\pi = 42$  MHz,  $n = 1.45$ , and sound velocity  $v = 5.96$  km/s [62] we find:

$$m(m-1) = \frac{\Gamma_B c}{nv\Omega_B}; \quad m \approx 7.$$

The small number of Stokes orders suitable for mode-locking is the factor limiting the proper operation of the mode-locked Brillouin fiber-lasers. In case of water at 532 nm, due the order of magnitude larger Brillouin linewidth  $\Gamma_B/2\pi = 540$  MHz, characteristic for liquids, the number of Stokes orders, which can *in principle* be mode-locked is 105. If those modes could be mode-locked *in practice* the output of such device would consist of a train of pico-second pulses. Unfortunately the focused geometry for observing SBS in liquids does not allow for long interaction lengths. The idea of pumping with non-diffracting beams, which is the subject of Chapter 4 of this Thesis may be suitable for experimental realization of Brillouin mode-locking in the future.

### 1.3 High-order harmonic generation

When an atom is exposed to an intense laser field, it develops a time-dependent dipole moment and radiates odd harmonics of the incident laser frequency. At low and moderate intensities ( $10^{13}$  to  $10^{14}$  W/cm<sup>2</sup>) this process has been studied extensively in the past using pico-second pulses [65–67]. Nowadays, the femto-second laser systems are capable of producing intensities up to  $10^{18}$  W/cm<sup>2</sup>. At such excitation level the atom can radiate harmonics with energies even above its ionization limit [68–70]. The process is accompanied and competes with ionization, but the conversion efficiency is still at a useful level. In the majority of the experiments high-order harmonic generation is achieved by focusing high peak intensity pulses into an expanding gas jet in vacuum. In this case the phase matching is dominated by the phase shift of the laser field passing through the focus (*i.e.* Guoy phase shift) [71, 72]. Some enhancement comes from positioning the focus slightly before the gas jet [73], but in general the divergence determines the interaction length.

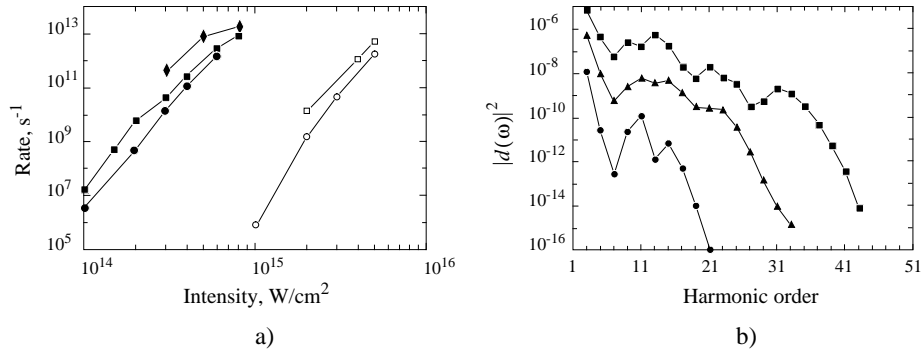


**Figure 1.14:** a) - Calculated ionization rates for He at 248 nm ( $\blacklozenge$ ), at 527 nm ( $\blacksquare$ ), and at 1053 nm ( $\bullet$ ); and for He<sup>+</sup> at 248 nm ( $\square$ ), and at 527 nm ( $\circ$ ); b) - Single-electron harmonic spectra  $|d(\omega)|^2$  for He at  $1 \times 10^{14} \text{ W}/\text{cm}^2$  ( $\bullet$ ), at  $3 \times 10^{14} \text{ W}/\text{cm}^2$  ( $\blacktriangle$ ), and at  $6 \times 10^{14} \text{ W}/\text{cm}^2$  ( $\blacksquare$ ). After Ref. [74].

Rare gases are preferentially used in these experiments for their high ionization limit, compared to other atoms. Helium, being the neutral atom with largest ionization potential ( $I_p = 24.6 \text{ eV}$ ) along with its only two electrons is a good test medium for studying high-harmonic generation [74]. Because the  $I_p$  of an ion is much larger, one can expect that much higher-order harmonics will be generated from ions. However, the ion has a lower polarizability, hence the conversion efficiency will be lower. When interacting with an intense laser field, both neutral atoms and their ions can contribute to the yield. The bound electrons tunnel through or flow over the suppressed Coulomb barrier, thus making direct transition to the continuum. The photoemission requires a transition from the continuum back to the ground state when the electron is near the nucleus [75], therefore the harmonic signal observable in an experiment is limited to the single-atom response. In Fig. 1.14a the calculated ionization rates in He and He<sup>+</sup> for different wavelengths as a function of the laser intensity are presented [74]. It is clearly seen that at a given intensity the ionization rate for He is considerably higher than that in He<sup>+</sup>. In case of He<sup>+</sup>, being one-electron system, the result is achieved by direct integration of the time-dependent Schrödinger equation, where in neutral He the single-active-electron approximation is applied. The resulting time-dependent induced dipole moment  $d(t)$  after Fourier transform yields the single atom photoemission rate  $|d(\omega)|^2$ . Fig. 1.14b shows the calculated harmonic intensities for He at 527 nm and intensities of  $1 \times 10^{14} \text{ W}/\text{cm}^2$  ( $\bullet$ ), at  $3 \times 10^{14} \text{ W}/\text{cm}^2$  ( $\blacktriangle$ ), and at  $6 \times 10^{14} \text{ W}/\text{cm}^2$  ( $\blacksquare$ ). From those graphs three important features of the harmonic spectra are seen: a rapid decrease of the intensity of the 5th and 7th harmonics, followed by a plateau of relatively constant intensity, and then a sharp cutoff at a specific harmonic order. At  $6 \times 10^{14} \text{ W}/\text{cm}^2$ , for instance, the cutoff begins at the 33rd harmonic. The same calculation for He<sup>+</sup> at 527 nm and intensity of  $5 \times 10^{15} \text{ W}/\text{cm}^2$  produces the same ionization

rate ( $\sim 2 \times 10^{12} \text{ s}^{-1}$ ) as for He at  $6 \times 10^{14} \text{ W/cm}^2$ , but the extent of the plateau is up to 500 eV.

There are two regularities seen in Fig. 1.14b. Both the extent of the plateau and its average intensity are bigger for higher laser intensities. The former is explained assuming that the maximum energy which can be emitted by an atom during the process of harmonic generation is equal to the energy difference between the ground state of the atom ( $-I_p$ ) and the maximum kinetic energy which the released into the continuum electron can acquire during the process of acceleration in the laser electric field ( $3U_p = 3I/(4\omega^2)$ ) [76]:

$$E_{max} \approx I_p + 3U_p, \quad (1.30)$$

where  $U_p = I/(4\omega^2)$  is the ponderomotive shift of the ionization potential. The cutoff energy scales linearly with the applied laser intensity and is proportional to  $\lambda^2$ . The latter dependence makes infrared pulses favorable for high-order harmonic generation.

Concerning the second regularity seen in Fig. 1.14b, a comparison between the overall plateau intensity and the ionization rate as a function of the laser intensity (see Fig. 1.14a) yields similar behavior for both quantities, i.e. the intensity of the plateau is proportional to the ionization rate. Hence, the processes responsible for harmonic emission and ionization are coupled. This rather qualitative picture of high-order harmonic generation describes very well most of the experimental observations and Eq.(1.30) is widely used for calculating the extent of the plateau.

In the microscopic theory presented so far the geometry of the interaction was not taken into account. In order to investigate phase-matched harmonic generation one has to consider parameters as material dispersion of the medium and beam geometry. As mentioned above, the Guoy phase shift in focused Gaussian beam is the predominant factor causing phase mismatch. In order to avoid this limitation the beam is focused just before the gas jet in most of the experiments. Working somewhat outside the confocal region requires even higher peak intensity. Alternative approach involves the use of a hollow waveguide filled with gas [77]. The plane wave nature of the mode makes it possible to ballance, over an extended interaction length, the positive dispersion of the neutral gas with the negative dispersion of both the waveguide and the free electrons [78,79]. The propagation constant  $k$  of the fundamental wave traveling through a hollow waveguide of radius  $a$  filled with a gas is  $k^2 = n^2 k_0^2 - (u_{11}/a)^2$  [80], where  $n$  is the refractive index of the medium,  $k_0$  is the propagation constant in vacuum, and  $u_{11} = 2.405$  is the first zero of the Bessel function  $J_0(r)$ . In case of partially ionized gas the index of refraction is  $n = 1 + P[(1 - \eta)\kappa(\lambda) - \eta N r_e \lambda^2 / 2\pi] + (1 - \eta)n_2 I$  [79], where  $P$  is the pressure in atmospheres,  $\eta \in (0, 1)$  - the ionization fraction,  $N$  - the number density at one atmosphere,  $\kappa(\lambda)$  is the neutral gas dispersion,  $r_e = 2.82 \times 10^{-13} \text{ cm}$  - the classical electron radius,  $n_2$  - the nonlinear refractive index, and  $I$  is the local laser intensity. Consequently, the propagation constant can be written in the form:

$$k \approx \frac{2\pi}{\lambda} + \frac{2\pi P(1 - \eta)\kappa(\lambda)}{\lambda} + \frac{2\pi(1 - \eta)n_2 I}{\lambda} - P\eta N r_e \lambda - \frac{u_{11}^2 \lambda}{4\pi a^2}, \quad (1.31)$$

where the right-hand side terms correspond to vacuum, neutral gas dispersion, nonlinear refractive index, plasma dispersion, and waveguide dispersion, respectively. The phase mismatch for the  $q$ th harmonic generation then is  $\Delta k = k_q - qk = qk_0[n(\lambda_q) - n(\lambda_0)]$ , or

$$\Delta k \approx q \frac{u_{11}^2 \lambda_0}{4\pi a^2} + N_e r_e (q\lambda_0 - \lambda_q) - q \frac{2\pi N_a}{\lambda_0} [\kappa(\lambda_0) - \kappa(\lambda_q)], \quad (1.32)$$

where  $N_a$  and  $N_e$  are the number density of the neutral atoms and the electrons, respectively. The growth of the harmonic intensity during the propagation through a hollow fiber with length  $L$ , taking into account absorption  $\alpha$  is [79]:

$$|E|^2 \approx N_a^2 |\chi_{\text{eff}}^{(q)} E_0^s|^2 \left( \frac{1 + e^{-2\alpha L} - 2e^{-\alpha L} \cos \Delta k L}{\alpha^2 + \Delta k^2} \right), \quad (1.33)$$

where the effective power of the nonlinearity  $s = 5$  is usually used in for single-atom response above  $10^{13}$  W/cm<sup>2</sup> [72, 81, 82]. Eq.(1.33) shows that the harmonic intensity is determined by the shorter of the coherence length ( $1/\Delta k$ ) and the absorption depth ( $1/2\alpha$ ). Hence, the strong absorption of gases for photon energies above their ionization potential limits the yield that can be obtained [79, 83].

Recent experiments [77, 79] have shown that good phase matching can be achieved for harmonic generation in a hollow waveguide, where the ionization fraction is kept below 10%. Under proper conditions of phase matching the harmonic yield was proven to be only limited by the absorption depth for a fiber of 3 cm length and Argon as a nonlinear medium [79]. By varying the gas pressure, the harmonic signal for orders 19 - 47 (from  $< 4.5$  mJ, 20 fs, 800 nm) can be increased by 2 - 3 orders of magnitude, compared to that of a gas jet. In our future experiments with powerful 300 ps Fourier-transform limited pulses, tunable within the Ti:Sapphire amplification range (*see* Chapter 7), we will implement both schemes for harmonic generation and determine which one will suit better our regime of expected greater ionization. In the case of hollow waveguide when high ionization fraction ( $\eta > 80\%$ ) is expected, quasi-phase matching technique can be applied as well [84].

## References

- [1] W. Kaiser and M. Maier, “*Stimulated Rayleigh, Brillouin and Raman spectroscopy*” in *Laser Handbook*, F. T. Arecchi and E. O. Schilz-DuBois, Eds. Amsterdam, North-Holland, vol. **2**, 1077 (1972).
- [2] P. Debye, “*Polar molecules*” (Dover Publications Inc.; New York 1929).
- [3] A. Einstein, *Ann. Phys. (Leipzig)* **33**, 1275 (1910).
- [4] L. Landau and G. Placzek, *Phys. Z. Sovietunion* **5**, 172 (1934).
- [5] R. W. Boyd, “*Nonlinear Optics*” (Academic Press Inc. 1996), Chapter 8.
- [6] I. L. Fabelinskii, “*Molecular Scattering of Light*” (Plenum Press, New York, 1968).
- [7] L. Brillouin, *Ann. Phys. (Paris)* **17**, 88 (1922).
- [8] D. Heiman, D. S. Hamilton, and R. W. Hellwarth, *Phys. Rev. B* **19**, 6583 (1979).
- [9] C. L. Tang, *J. Appl. Phys.* **37**, 2945 (1966).

- [10] R. Y. Chiao, C. H. Townes, and B. P. Stoicheff, Phys. Rev. Lett. **12** 592 (1964).
- [11] R. S. Krishnan, Proc. Indian Acad. Sci. **A41** 91 (1955).
- [12] E. Garmire, C. H. Townes, Appl. Phys. Lett. **5**, 84 (1964).
- [13] K. F. Herzfeld and T. A. Litovitz, “*Absorption and Dispersion of Ultrasonic Waves*” (Academic Press, New York, 1959).
- [14] T. A. Wiggins, R. V. Wick, D. H. Rank, and A. H. Günther, Appl. Opt. **4**, 1203 (1965).
- [15] R. V. Wick, D. H. Rank, and T. A. Wiggins, Phys. Rev. Lett. **17**, 466 (1966).
- [16] T. A. Wiggins, R. V. Wick, N. D. Foltz, C. W. Cho, and D. H. Rank, J. Opt. Soc. Am. **57**, 661 (1967).
- [17] N. Goldblatt and M. Hercher, Phys. Rev. Lett. **20**, 310 (1968).
- [18] Yu. I. Kyzylasov and V. S. Starunov, JETP Lett. **7**, 123 (1968) [In Russian: Письма в ЖЭТФ **7**, 160 (1968)].
- [19] R. G. Brewer and K. E. Reickhoff, Phys. Rev. Lett. **13**, 334 (1964).
- [20] A. S. Pine, Phys. Rev. **149**, 113 (1966).
- [21] J. Walder and C. L. Tang, Phys. Rev. **155**, 318 (1967).
- [22] J. L. Emmett and A. L. Schawlow, Phys. Rev. **170**, 358 (1968).
- [23] M. Denariez and G. Bret, Phys. Rev. **171**, 160 (1968).
- [24] M. Maier, Phys. Rev. **166**, 113 (1968).
- [25] E. E. Hagenlocker and W. G. Rado, Appl. Phys. Lett. **7**, 236 (1965).
- [26] D. H. Rank, T. A. Wiggins, R. V. Wick, D. P. Eastman, and A. H. Günther, J. Opt. Soc. Am. **56**, 174 (1966).
- [27] E. P. Ippen and R. H. Stolen, Appl. Phys. Lett. **21**, 539 (1972).
- [28] D. Cotter, Electron. Lett. **18**, 495 (1982).
- [29] B. Ya. Zel’dovich, N. F. Pilipetskii, and V. V. Shkunov, “*Principles of Phase Conjugation*” in *Series in Optical Sciences* (Springer-Verlag, Berlin Heidelberg 1985).
- [30] B. Ya. Zel’dovich, N. F. Pilipetskii, and V. V. Shkunov, “*Experimental Investigation of Wave-Front Reversal under Stimulated Scattering*” in *Optical Phase Conjugation* Ed. R. A. Fisher (Academic Press Inc. London 1983) p. 135.
- [31] R. W. Hellwarth, “*Phase Conjugation by Stimulated Backscattering*” in *Optical Phase Conjugation* Ed. R. A. Fisher (Academic Press Inc. London 1983) p. 169.
- [32] O. Yu. Nosach, V. I. Popovichev, V. V. Ragul’skii, and F. S. Faizullof, JETP Lett. **16**, 435 (1972) [In Russian: Письма в ЖЭТФ **16**, 617 (1972)].
- [33] R. W. Hellwarth, J. Opt. Soc. Am. **67**, 1 (1977).
- [34] A. Yariv and D. M. Pepper, Opt. Lett. **1**, 16 (1977).
- [35] D. M. Bloom and G. C. Bjorklund, Appl. Phys. Lett. **31**, 592 (1977).
- [36] D. M. Pepper and A. Yariv, “*Optimal Phase Conjugation Using Three-Wave and Four-Wave Mixing via Elastic Photon Scattering in Transparent Media*” in *Optical Phase Conjugation* Ed. R. A. Fisher (Academic Press Inc. London 1983) p. 24.
- [37] B. Ya. Zel’dovich, V. I. Popovichev, V. V. Ragul’skii, and F. S. Faizullof, JETP Lett. **15**, 109 (1972) [In Russian: Письма в ЖЭТФ **15**, 160 (1972)].
- [38] M. Maier, W. Kaiser, and J. A. Giordamine, Phys. Rev. Lett. **17**, 1275 (1966); M. Maier, W. Kaiser, and J. A. Giordamine, Phys. Rev. **177**, 580 (1969).
- [39] W. H. Culver, J. T. A. Vanderslice, and V. W. T. Townsend, Appl. Phys. Lett. **12**, 189 (1968).
- [40] R. V. Johnson and J. H. Marburger, Phys. Rev. A **4**, 1175 (1971).
- [41] R. W. Minck, E. E. Hagenlocker, and W. G. Rado, J. Appl. Phys. **38**, 2254 (1967).
- [42] J. R. Murray, J. Goldhar, D. Eimerl, and A. Szóke, IEEE J. Quantum Electron. **15**, 342 (1979).

- [43] J. J. Ewing, R. H. Haas, J. C. Swingle, E. V. George, and W. F. Krupke, *IEEE J. Quantum Electron.* **15**, 368 (1979).
- [44] D. T. Hon, *Opt. Lett.* **5**, 516 (1980).
- [45] M. J. Damzen and H. Hutchinson *IEEE J. Quantum Electron.* **19**, 7 (1983).
- [46] G. J. Crofts, M. J. Damzen, and R. A. Lamb, *J. Opt. Soc. Am. B* **8**, 2282 (1991).
- [47] C. Brent Dane, W. A. Neuman, and L. A. Hackel, *IEEE J. Quantum Electron.* **30**, 1907 (1994).
- [48] S. Schiemann, W. Ubachs, and W. Hogervorst, *IEEE J. Quantum Electron.* **33**, 358 (1997).
- [49] D. Neshev, I. Velchev, W. A. Majewski, W. Hogervorst, and W. Ubachs, *Appl. Phys. B* **68**, 671 (1999).
- [50] I. Velchev, D. Neshev, W. Hogervorst, and W. Ubachs, *IEEE J. Quantum Electron.* **35**, 1812 (1999).
- [51] S. Schiemann, W. Hogervorst, and W. Ubachs, *IEEE J. Quantum Electron.* **34**, 407 (1998).
- [52] G. Grynberg, B. Kleinmann, M. Pinard, and P. Verkerk, *Opt. Lett.* **8**, 614 (1983).
- [53] A. M. Scott and K. D. Ridley, *IEEE J. Quantum Electron.* **25**, 438 (1989).
- [54] V. I. Bespalov and G. A. Pasmanik, *Bull. Acad. Sci. USSR Phys. Ser. A* **17** (1980); [In Russian: *Известия Академии Наук СССР, серия Физическая* **44** 1572 (1980)].
- [55] N. F. Andreev, V. I. Bespalov, A. M. Kiselev, A. Z. Matveev, G. A. Pasmanik, and A. A. Shilov, *JETP Lett.* **32**, 625 (1981); [In Russian: *Письма в ЖЭТФ* **32**, 639 (1980)].
- [56] N. F. Andreev, V. I. Bespalov, M. A. Dvoretzky, and G. A. Pasmanik, *IEEE J. Quantum Electron.* **25**, 346 (1989).
- [57] M. W. Bowers and R. W. Boyd, *IEEE J. Quantum Electron.* **34**, 634 (1998).
- [58] N. G. Basov, V. F. Efimkov, I. G. Zubarev, A. V. Kotov, S. I. Mikhailov, and M. G. Smirnov, *JETP Lett.* **28**, 197 (1978).
- [59] M. W. Bowers, R. W. Boyd, and A. K. Hankla, *Opt. Lett.* **22**, 360 (1997).
- [60] M. Valley, G. Lombardi, and R. Aprahamian, *J. Opt. Soc. Am. B* **3**, 1492 (1986).
- [61] D. L. Carroll, R. Johnson, S. J. Pfeifer, and R. H. Moyer, *J. Opt. Soc. Am. B* **9**, 2214 (1992).
- [62] G. P. Agrawal, *“Nonlinear Fiber Optics”*, (Academic, 1995).
- [63] O. Hill, D. C. Johnson, and B. S. Kawasaki, *Appl. Phys. Lett.* **29**, 185 (1976).
- [64] B. S. Kawasaki, D. C. Johnson, Y. Fujii, and O. Hill, *Appl. Phys. Lett.* **32**, 429 (1978).
- [65] A. McPherson, G. Gibson, H. Jara, U. Johann, T. S. Luk, I. A. McIntyre, K. Boyer, and C. K. Rhodes, *J. Opt. Soc. Am. B* **4**, 595 (1987).
- [66] A. L’Huillier, K. J. Schafer, and K. C. Kulander, *J. Phys. B* **24**, 3165 (1991).
- [67] A. L’Huillier, K. J. Schafer, and K. C. Kulander, *J. Phys. B* **24**, 3315 (1991).
- [68] J. J. Macklin, J. D. Kmetec, and C. L. Gordon III, *Phys. Rev. Lett.* **70**, 766 (1993).
- [69] J. Zhou, J. Peatross, M. M. Murnane, H. C. Kapteyn, and I. P. Christov, *Phys. Rev. Lett.* **76**, 752 (1996).
- [70] C. Spielmann, H. Burnett, R. Sartania, R. Koppitsch, M. Schnurer, C. Kan, M. Lenzner, P. Wobrauschek, and F. Krausz, *Science* **278**, 661 (1997).
- [71] A. L’Huillier, X. F. Li, L. A. Lompre, *J. Opt. Soc. Am. B* **7**, 527 (1990).
- [72] A. L’Huillier, K. J. Schafer, and K. C. Kulander, *Phys. Rev. Lett.* **66**, 2200 (1991).
- [73] A. L’Huillier and P. Balcou, *Phys. Rev. Lett.* **70**, 774 (1993).
- [74] J. L. Krause, K. J. Schafer, and K. C. Kulander, *Phys. Rev. Lett.* **68**, 3535 (1992).
- [75] J. L. Krause, K. J. Schafer, and K. C. Kulander, *Phys. Rev. A* **45**, 4998 (1992).
- [76] T. F. Gallagher, *Phys. Rev. Lett.* **61**, 2304 (1988).
- [77] A. R. Rundquist, C. G. Durfee, Z. H. Chang, C. Herne, S. Backus, M. M. Murnane, and H. C. Kapteyn, *Science* **280**, 1412 (1998).

- [78] C. G. Durfee, S. Backus, M. M. Murnane, and H. C. Kapteyn, *Opt. Lett.* **22**, 1565 (1997).
- [79] C. G. Durfee, A. R. Rundquist, S. Backus, C. Herne, M. M. Murnane, and H. C. Kapteyn, *Phys. Rev. Lett.* **83**, 2187 (1999).
- [80] E. A. J. Marcatili and R. A. Schmelzter, *Bell Syst. Tech. J.* **43**, 1783 (1964).
- [81] K. C. Kulander and B. W. Shore, *Phys. Rev. Lett.* **62**, 524 (1989).
- [82] K. C. Kulander and B. W. Shore, *J. Opt. Soc. Am. B* **7**, 502 (1990).
- [83] E. Constant, D. Garzella, P. Breger, E. Mvel, Ch. Dorrer, C. Le Blanc, F. Salin, and P. Agostini, *Phys. Rev. Lett.* **82**, 1668 (1999).
- [84] I. Christov, H. C. Kapteyn, and M. M. Murnane, *Optics Express* **3**, 360 (1998).

## Chapter 2

# SBS pulse compression to 200 ps in a compact single-cell setup.\*

Temporal compression of nanosecond pulses from a commercial Q-switched Nd:YAG laser at 2nd and 3rd harmonic into the sub-nanosecond regime is demonstrated. In a geometry consisting of a single cell only, compression in several liquid media is investigated. For both 532 and 355 nm smooth and reliable operation is obtained with output pulses as short as 200 ps. A new concept is proposed to separate SBS-pulses from the pump beam at low optical losses.

### 2.1 Introduction

Stimulated Brillouin scattering (SBS) is a nonlinear optical process, discovered already in the first decade of laser physics, i.e. in the 1960s. For an introduction to the physics underlying SBS we refer to the book of Boyd [1]. Since its invention the main application of SBS has been in optical phase conjugation. In the past two decades the use of SBS for the compression of laser pulses has been investigated theoretically and experimentally [2–6] for various types of lasers and active media. Dane *et al.* [7] demonstrated pulse compression at very high energies, while Fedosjevs and Offenberger [8] achieved compressibility by a factor of 60. As a third application of SBS we mention its use to filter spontaneous emission from a laser beam [9].

Various geometries of SBS laser-pulse compressors have been proposed, usually showing the features of a generator for a SBS-backscattered wave followed by amplification in one or more stages. Damzen and Hutchinson [10] investigated the special design of a tapered waveguide. Recently Schiemann *et al.* [11] reported on a compact generator-amplifier setup (CGAS) in which efficient compression of 532 nm pulses from a Nd:YAG laser was achieved. Following up on the CGAS-design we present a simplified SBS-scheme consisting of a single cell and using a limited number of optical components only. In this setup we demonstrate efficient compression of pulses of 4-5 ns duration from an injection-seeded Nd:YAG-laser at its 2nd and 3rd harmonics. The SBS-behaviour in water, methanol, ethanol and CCl<sub>4</sub> is investigated. Particularly the relation between the phonon lifetime, i.e. the relaxation damping time of hypersound in the liquid, and optimum compressibility has been studied. This phonon lifetime  $\tau_p$  is a material property of the medium, which scales with wavelength as [1, 5]:

$$\tau_p = \tau'_p (\nu'/\nu)^2. \quad (2.1)$$

Hence at shorter wavelengths as well as in CCl<sub>4</sub> with the shortest phonon lifetime among the media investigated in this study, the highest compression is expected.

---

\*Applied Physics B68 (4) 671-675 (1999).

At both wavelengths, 532 and 355 nm, we provide a prescription to achieve pulse durations of 200 ps, which may turn Nd:YAG-lasers, available in many laboratories, into more versatile tools for dynamical and nonlinear optics studies. Also we propose an alternative method for separating the compressed Stokes pulses from the incident pump beam. Usually the beams are separated by polarization; we suggest to take advantage of the frequency shift of the SBS-output.

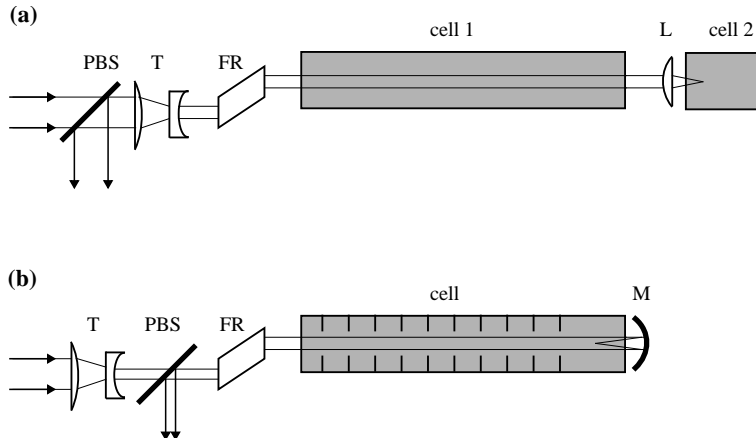


**Figure 2.1:** Geometrical configurations for SBS compressors. a) two-cell compact generator-amplifier setup (CGAS) as used previously by our group [11] with circularly polarized light; b) single-cell geometry used in the present study (T - telescope, PBS - polarizing beam splitter, FR - Fresnel rhomb, L - lens, M - mirror).

## 2.2 Experimental setup and measurement methods

The geometries of relevance for the present experiments are schematically depicted in Fig. 2.1. In our previous work [11] SBS-pulse compression was demonstrated in a compact generator-amplifier setup (CGAS), depicted in Fig. 2.1a. The CGAS consists of two separate cells filled with liquid: one for the generation of the SBS-Stokes pulse and the other for amplification, without use of attenuators. The underlying concept of this approach is that the necessary attenuation of the pump beam propagating towards the oscillator results from pump depletion induced by the SBS-amplification. In Fig. 2.1b we introduce a simplified geometry based on a single cell involving a concave mirror, coated for high reflectivity at 532 or 355 nm, that redirects the generated SBS-pulse through the same cell for amplification. Again, as discussed in [11] two basic ideas determine the choice of focal length of the reflecting mirror and the cell length. The focussing in the oscillator part may be chosen as tight as possible, such that the very leading edge of the pump beam reaches SBS-threshold in the focus. A lower limit to

the focal length is, however, determined by the restriction that optical breakdown in the medium must be prevented. With available cleaning methods to filter solid particulates from the liquid (poresize 200 nm) focal lengths of 10 cm can be combined with pulse energies of up to 300 mJ, while avoiding optical breakdown for more than 99% of the pulses. The cell length is chosen such that the phase-conjugate SBS-pulse folds on to the entire counter-propagating pump beam for amplification. At the same time scattering losses, of both pump and Stokes beams, are minimized by keeping the cell as short as possible. Since SBS-oscillation starts from the leading edge of the propagating pulse an optimum is expected for a spatial length of the pulse of  $(c/n)\tau$ , where  $\tau$  is the pulse duration at full-width-half-maximum (FWHM) and  $n$  the index of refraction of the liquid medium. For a pulse duration of 5 ns (FWHM) and a typical index of refraction of  $n = 1.3 - 1.5$  the cell length was taken at 1.1 m. The linearly polarized beam from the laser passes through a Fresnel rhomb to transform the beam pumping the SBS-process into a circular polarization state. The generated SBS-beam can be separated from the pump beam using a thin-film polarizing beam splitter, under optimized angles ( $60^\circ$  for 532 nm and  $50^\circ$  for 355 nm). To preserve the circular polarization the beams pass the window surfaces of the cell under normal incidence.

A telescope is used to resize the laser beam diameter. In this way the optimal energy density is adjusted to achieve maximum compression of the input pulse as discussed in [11]. The peak intensity of the pump pulse in the collimated arm should be kept below the SBS-threshold to avoid diffuse SBS, which perturbs proper pulse compression. A further improvement in the setup involves ten diaphragms inserted in the cell preventing Rayleigh scattered light to be guided from the cell walls into the interaction region. This resulted in a considerable decrease of scattered photons from the cell, hampering the data acquisition.

Pulse compression was investigated for two different wavelengths. Both the second and third harmonics of an injection-seeded, Q-switched Nd:YAG laser (Spectra-Physics, Quanta-Ray GSR 330-10) were used to pump the SBS-process. Injection seeded operation of the Nd:YAG laser is necessary to prohibit mode-beating, which gives rise to competing nonlinearities and optical breakdown. The experiments were performed at a repetition rate of 10 Hz. Measurements of the spatial beam profile were performed using photo-sensitive paper, while a CCD camera (Hitachi VK-M98E) with a large active area window was used for online monitoring. An investigation of SBS pulse compression as a function of spatial position in the transverse profile was performed by extracting part of the beam using a short, multimode optical fiber of  $\sim 100 \mu\text{m}$  core-diameter. It was verified, by monitoring femtosecond pulses at various input intensities, that the dispersion and nonlinear effects in this fiber are negligible.

Temporal characteristics of the pulses were measured with three different techniques. Firstly, a fast oscilloscope (Tektronix TDS 680B - 1GHZ, 5Gs) combined with a fast photodiode (Hamamatsu G4176 - 100 ps) was employed for online registration of pulse durations. The temporal resolution of this system was evaluated by monitoring pulses (100 fs) from a femtosecond laser to be 430 ps. It was also used to measure pump-pulse durations. Secondly, a sampling oscilloscope (Tektronix 7904 equipped with 7S11 sampler and S6 sampling head) was used in combination with a 100 ps photodiode.

**Table 2.1:** Indices of refraction  $n$ , at temperatures of 25 °C, and values for the phonon lifetimes  $\tau_p$  (in ps) at the two relevant wavelengths. Values of  $\tau_p$  are obtained from Ref. [1] after wavelength scaling.

liquid	$n$	$\tau_p$ (532 nm)	$\tau_p$ (355 nm)
water	1.333	295	131
ethanol	1.359	265	118
methanol	1.326	374	166
CCl <sub>4</sub>	1.460	180	80

Because of the low repetition rate of the laser source and the time jitter of the trigger this measurement gives a relatively low signal-to-noise ratio; moreover the sampling oscilloscope does not provide single-shot pulse information. An advantage of this device is the absolute accuracy of its time base.

The actual data on SBS-compression delivering the shortest pulses were taken with a streak camera (Hadland IMACON 500 - 20 ps). The two-dimensional streak-images on the phosphor were monitored with a CCD-camera and fed, via a frame-grabber, into a PC for data analysis. Temporal calibration of the streak camera was performed by comparing measurements with those of the sampling oscilloscope. The intensity scale of the streak camera was calibrated by simultaneously measuring long laser pulses with the 1 GHz oscilloscope.

Prior to the measurements of SBS pulse compression some spatial and temporal characteristics of the pump beam were determined. The spatial profile at the entrance of the amplifier cell corresponds to a Super-Gaussian shape (third power) with FWHM of 6.6 mm for the second harmonic (532 nm), while the third harmonic is closer to Gaussian. The pulse has a Gaussian temporal profile with a FWHM  $\sim 5.0$  ns for the green and slightly shorter ( $\sim 4.6$  ns) for the UV. Due to the injection-seeding the Nd:YAG laser runs in a single longitudinal mode with a frequency spectrum close to Fourier-transform limited.

### 2.3 Results and discussion

Experiments on SBS pulse compression were performed for four different liquid media: water, methanol, ethanol and carbon-tetrachloride (CCl<sub>4</sub>) and for two wavelengths (532 and 355 nm). Refractive indices for these substances and values for the phonon lifetimes, extracted from Ref. [1] and corrected for the wavelength dependence following Eq. (2.1), are presented in Table 2.1.

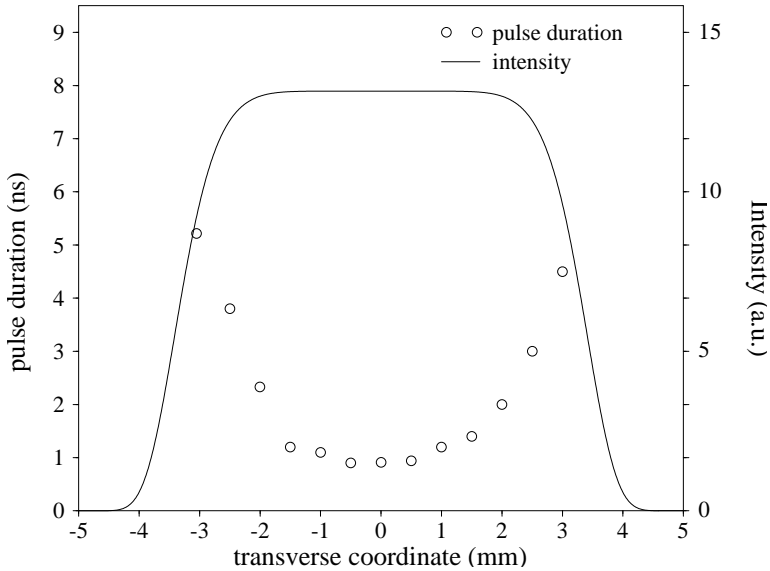


**Figure 2.2:** Compression of the laser pulse *vs.* transverse coordinate; data taken for water as SBS-medium and pump pulse at 532 nm with 6 ns duration. (a) a fit through the measured pump beam profile; (b) experimental data on pulse durations of compressed pulses. Temporal resolution of the detection system for this measurement is 430 ps; therefore the energy density in the compressor was adjusted for a Stokes pulse duration not shorter than 1 ns.

### 2.3.1 Transverse beam profile effect in SBS

In the theoretical investigation of SBS-compression usually a plane-wave approximation is considered. This simplification of the problem to a single dimension implies a uniform compression over the transverse profile of the laser beam. We studied the effect of the varying intensity over the spatial beam profile experimentally, using a short multi-mode optical fiber to extract light from a specific point in the beam and a photodiode combined with the 1 GHz oscilloscope (time resolution 430 ps) for registration. In this way we measured the local compression factor for green pulses (532 nm) of FWHM = 6.6 mm using water as SBS-medium; only for this specific measurement pump pulses of 6 ns duration were used. We reduced the laser intensity to a level where compression yields pulses not shorter than 1 ns. The results of measurements on the transverse beam profile dependence are presented in Fig. 2.2. It is clearly seen that the beam is highly compressed in the vicinity of the center, while in the wings the compression is much less. Fig. 2.2 shows that the central part, defined by the inner 4 mm of the diameter, is compressed close to the minimum pulse duration. When we operate the laser closer to the optimum compression energy (see below) the region of shortest pulse duration

**Table 2.2:** Results of the SBS-processes studied;  $E_{th}$  is the threshold energy for the formation of a phase-conjugated SBS-Stokes pulse;  $E_{opt}$  is the pulse energy for which SBS-compression is optimal (both  $E_{th}$  and  $E_{opt}$  given for spatial beam of FWHM = 6.6 mm); Reflectivity  $R$  holds for energy  $E_{opt}$  (including 35% optical losses);  $\tau_t$  refers to a *typical* (*i.e.* average) observation of Stokes pulse durations.

liquid	$E_{th}$ (mJ)	$E_{opt}$ (mJ)	$R$ (%)	$\tau_t$ (ps)
SBS at 532 nm				
water	1.75	180 (10)	57.9	325
methanol	0.62	84 (5)	54.0	366
ethanol	0.63	67 (5)	56.7	-
$\text{CCl}_4$	1.0	65 (5)	56.9	200
SBS at 355 nm				
water	1.9	87 (5)	43.5	200
methanol	0.5	39 (3)	41.9	-

is even broader than 4 mm. In previous work [12] we have investigated the dependence of compressibility on averaged beam intensity. The theoretical prediction that at pump intensities below an optimum value compression is less efficient was experimentally verified. With the model of Refs. [11, 12] the present results on the dependence of compressibility on local intensity can be understood in a quantitative sense.

Spatial beam profiles of the incident pump beam as well as the SBS-reflected beam were measured in the form of single-shot imprints in photosensitive paper. These imprints show, in a qualitative sense, that the beam quality is preserved by the compression process. In the following we present only data pertaining to the central part of the beam.

### 2.3.2 Pulse compression at 532 nm for various liquids

In Fig. 2.3 some *typical* results on pulse compression at 532 nm are presented; the pictures correspond to single shot measurements taken with the streak camera. Measurements of SBS threshold, optimal energy, energy of the SBS compressed beam and the reflectivity of the setup for four different liquids are presented in Table 2.2. Energies and intensities of the pulses can be related by accounting for the beam diameter of FWHM=6.6 mm. As shown previously [11, 12] optimum compressibility is obtained at a certain pump beam intensity. For a fixed beam diameter (as in the present study) this corresponds to a certain optimal energy ( $E_{opt}$ ); in practical applications the beam diameter can be adjusted such that  $E_{opt}$  matches the pump intensity for optimum compression. A combination of maximum energy and optimal compression (for the fixed beam of FWHM=6.6 mm) is achieved in water, while the shortest pulses were obtained in  $\text{CCl}_4$ . In the experiments on pulse compression in water and ethanol the process of Stimulated Raman Scatter-

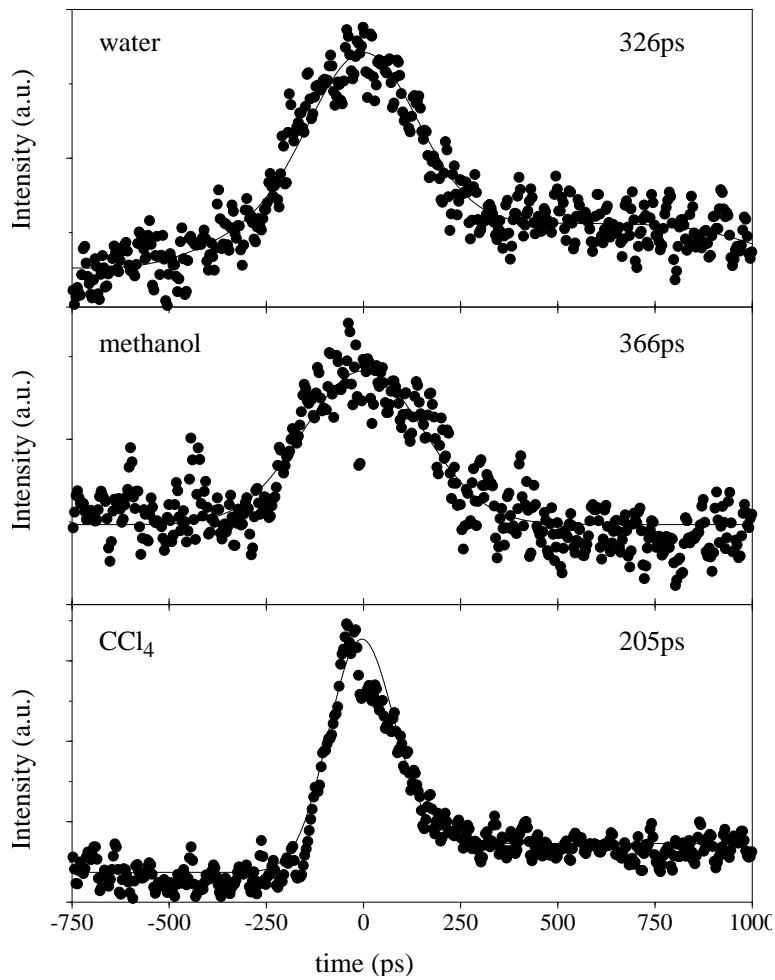


**Figure 2.3:** Streak camera recordings of *typical* SBS-Stokes pulses measured for a pump wavelength at 532 nm using three different media.

ing (SRS) competes with SBS. In the case of water at optimal incident energy SRS is weak and does not influence SBS pulse compression. However in the case of ethanol intense red SRS-flashes were observed, accompanied by temporal fragmentation of the SBS backscattered pulse. This makes ethanol an unreliable SBS-medium, in contrast to water and methanol. The optimum reflectivities, of about 57%, seem to be small. However, the optical losses in the setup, where no anti-reflection coated optics was used, were estimated to be 35%, so that the intrinsic SBS-reflectivity is evaluated to be more

than 90%.

An important finding in the pulse duration measurements is the spread in the output pulse durations. The results presented in Fig. 2.3 and the values for the pulse duration (FWHM) listed in Table 2.2 are *typical*, i.e. averaged over a large number of measurements. While in methanol the most probable pulse duration obtained was 366 ps (Fig. 2.3b), we did observe pulses as short as 330 ps. The same holds for the other liquids. An exceptionally short pulse (of 110 ps) was observed in  $\text{CCl}_4$ , where the average value is 200 ps (Fig. 2.3c). Apparently there is a statistical spread in pulses emanating from a SBS-compressor. This spread is likely to be related to the origin of the pulses, a build-up from noise. This issue, first addressed by Buzelis *et al.* [13], remains a subject for future experimental and theoretical studies.

Although the issue is debated in literature [2–4,6,10,11] the phonon lifetime is often considered as a lower limit to pulse compression in SBS. Here we find experimentally SBS-compressed pulses with duration notably shorter than the phonon lifetime. The typical averaged values for the pulse duration as experimentally observed indeed are limited by the phonon lifetime. When comparing the results of minimum Stokes pulse duration in the various liquids (*see* Table 2.2) the trend indeed follows the phonon lifetimes (*see* Table 2.1).

### 2.3.3 Pulse compression at 355 nm

In the UV region at 355 nm shorter pulses are expected from the SBS-compressor due to the shorter phonon lifetime at higher frequencies (*see* Eq. (2.1)). Some practical restrictions may be expected from enhanced Rayleigh scattering and from photochemistry induced by the high intensity UV laser beam. A practical problem encountered during the measurements was the low transmittivity for UV of the streak-camera optics, which gave rise to an increased noise in the data.

The experiments were performed in water and methanol and the results for the SBS-threshold, optimal energy and reflectivity are included in Table 2.2. The values of the optimal energy were derived from measurements using the 1 GHz oscilloscope. Streak camera pictures could only be measured for compression in water where the output energy is just sufficiently high to extract a curve from the noise. A typical example is shown in Fig. 2.4. In methanol smooth operation of the SBS-compressor was verified with measurements using the photodiode; however, due to the lower value of  $E_{opt}$  the output energy was insufficient to determine a value for the optimum compression with the streak camera. While in water the average pulse duration was 200 ps, pulses as short as 180 ps were observed, again indicating a spread in the Stokes pulse durations. The expectation that in the UV region shorter pulses may be generated is confirmed in this experiment.

While the experiments in water and methanol produced smooth SBS-pulses with reasonable pulse-to-pulse fluctuations no reliable measurements could be performed on  $\text{CCl}_4$  in combination with 355 nm pulses. In the latter case the liquid turned yellow after irradiation with UV giving rise to strong absorption and hence prohibiting proper SBS-compression measurements. Whether this is caused by UV-induced photochemistry

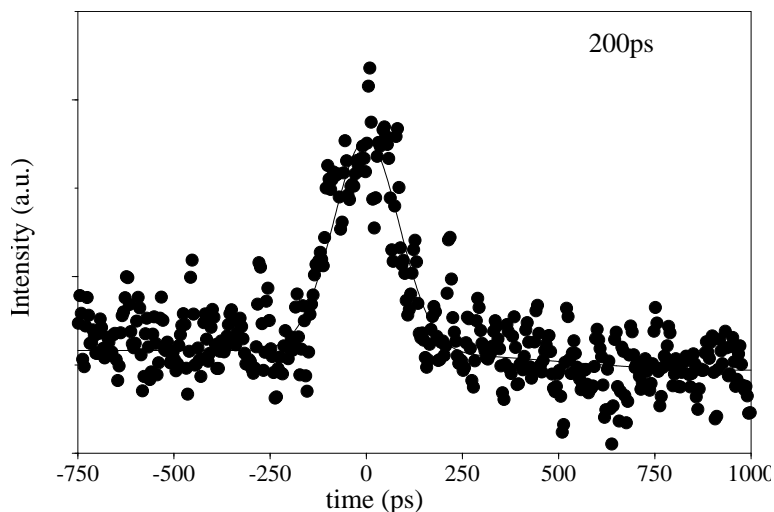


**Figure 2.4:** Streak camera recording of a typical pulse measured in water for a pump wavelength at 355 nm.

in the  $\text{CCl}_4$  liquid, or by the effects of the intense Rayleigh scattered light on to the viton O-rings sealing the cell could not be unambiguously decided.

### 2.3.4 Proposal for a simplified low-loss SBS-geometry

In Fig. 2.1b a compact single-cell configuration was presented, which is demonstrated to be a useful tool for SBS-compression. In Fig. 2.5 we propose another single-cell setup for SBS, which has not been tested yet, but that may have some advantages over the design presently used. The optical losses in the present setup can be further reduced by mounting the concave retroreflecting mirror, which in fact separates the oscillator from the amplifier, inside the liquid, therewith reducing the number of optical elements. We have not attempted this in the setup of Fig. 2.1b, since we do not have access to a highly reflecting concave mirror fulfilling the more rigorous demands with respect to damage threshold for operation inside a liquid.

To our knowledge, in all setups reported in literature for SBS pulse compression the Stokes beam is separated from the pump beam by its polarization; hence a number of polarization components is usually required. Now, for a new separation method, we propose to take advantage of the frequency shift over several GHz (depending on the medium) of the Stokes beam. An etalon may be inserted under a specific angle (again depending on the Stokes shift) in the beam to fully transmit the pump wave and reflect the Stokes wave. Demands on the damage threshold and optical quality of the etalon coating are high; in an attempt to demonstrate this method with a commercial etalon it

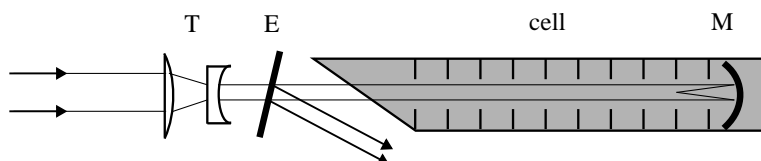


**Figure 2.5:** Proposal for a simplified single-cell SRS-configuration to be used with linearly polarized light and low optical losses; T-telescope; M-mirror; E-etalon.

was severely damaged. In principle this scheme possesses intrinsically low optical losses and could be successfully applied where high reflectivity is required. An advantage is that the polarization of incident and Stokes pulse may remain linear; this will allow for the use of a Brewster cut window at the entrance of the compressor. An additional feature is that the SRS-process occurs on a single transverse mode giving rise to a higher SRS-gain than for circularly polarized light.

## 2.4 Conclusion

A new setup for SRS pulse compression has been demonstrated, providing pulses as short as 200 ps at two different wavelengths. The pulse compression in different liquids was investigated. Laser pulses at 532 and 355 nm of 4-5 ns duration may be compressed to 200 ps for a reliable and smooth operation at 10 Hz repetition rate. We have shown that optimum SRS-compression occurs in a flat-topped inner region of the transverse beam profile; for applications of compressed pulses the outer wings of the beam may be filtered away. For the 3rd harmonic at 355 nm water appears to be the appropriate medium, while at the 2nd harmonic at 532 nm  $\text{CCl}_4$  may be favorably used. In previous work [12] we have demonstrated the possibility of continuously tuning the pulse duration between the duration of the lower limit (now 200 ps) and the duration of the incident pump beam, by varying the diameter of the pump beam. These experiments on SRS pulse compression provide a recipe for equipping commercially available Q-switched injection-seeded Nd:YAG lasers, in use in many laboratories around the world, with an extension of a short-pulse option. Such an option, consisting of a single cell filled with liquid and some polarization optics, transforms common lasers into more versatile tools for dynamical and nonlinear optics studies.

## Acknowledgments

This work was carried out with a research grant from the Netherlands Foundation for Research of Matter (FOM). D.N. thanks the Atomic Physics research group at the Vrije Universiteit Amsterdam for the warm hospitality during his research stay and the Netherlands Organization for International Cooperation in Higher Education (NUFFIC) for financial support.

## References

- [1] R. W. Boyd, “*Nonlinear Optics*”, (Academic press, 1993).
- [2] D. T. Hon, *Opt. Lett.* **5**, 516 (1980).
- [3] V. A. Gorbunov, S. B. Papernyi, V. F. Petrov, V. R. Startsev, *Sov. J. Quantum Electron.* **13**, 900 (1983).
- [4] A. A. Offenberger, D. C. Thompson, R. Fedosejevs, B. Harwood, J. Santiago, H.R. Manjunath, *IEEE J. Quantum Electron.* **29**, 207 (1993).
- [5] A. I. Erokhin, V. I. Kovalev, F. S. Faizullof, *Sov. J. Quantum Electron.* **16**, 872 (1986).
- [6] M. A. Davydov, F. K. Shipilov, T. A. Shmaonov, *Sov. J. Quantum Electron.* **30**, 1907 (1994).
- [7] C. B. Dane, W. Neuman, L. Hackel, *IEEE J. Quantum Electron.* **30**, 1907 (1994).
- [8] R. Fedosjevs, A. A. Offenberger, *IEEE J. Quantum Electron.* **21**, 1558 (1985).
- [9] C. K. Ni, A. H. Kung, *Opt. Lett.* **21**, 1673 (1996).
- [10] M. J. Damzen, H. Hutchinson, *IEEE J. Quantum Electron.* **19**, 7 (1983).
- [11] S. Schiemann, W. Ubachs, W. Hogervorst, *IEEE J. Quantum Electron.* **33**, 358 (1997).
- [12] S. Schiemann, W. Hogervorst, W. Ubachs, *IEEE J. Quantum Electron.* **34**, 407 (1998).
- [13] R. Buzelis, A.S. Dementev, E.K. Kosenko, E. Muraskas, *Sov. J. Quantum Electron.* **25**, 540 (1995) [in Russian: *Квантовая Электроника* **22**, 567 (1995)].



## Chapter 3

# Pulse compression to the sub-phonon lifetime region by half-cycle gain in transient stimulated Brillouin scattering.\*

A new approach to the transient pulse compression by stimulated Brillouin scattering (SBS) is presented. The theoretical analysis involving the time-dependent SBS gain in explicit form leads to a nonlinear system of partial differential equations, solved numerically by a generalization of the split-step method. It is shown theoretically and confirmed experimentally that the phonon lifetime is not always an appropriate parameter that determines the lower limit to the pulse duration in SBS compressors. A half-cycle gain regime is found for pulses shorter than the phonon lifetime. Hence, under proper conditions, pulses as short as half the acoustic period can be produced.

### 3.1 Introduction

The phenomenon of stimulated Brillouin scattering (SBS) in liquid or gaseous media is nowadays widely used as a tool to compress nanosecond laser pulses down to the sub-nanosecond region with remarkable conversion efficiency, theoretically reaching 100%. The first experimental result, some 20 years ago [1], inspired many attempts to develop a theory explaining the physical background of the process of pulse compression. Although most of the theories available are in good agreement with experimental results, they fail in treating the problem in the fully transient regime, where the compressed pulse is found to be shorter than the phonon lifetime of the medium. In this Chapter we present a new analysis of the equations as well as a numerical method for modeling the compression in transient regime. A double compressor experiment is conducted in order to confirm the theoretical and numerical results.

### 3.2 Theory of transient SBS

We consider the SBS process involving two classical optical fields  $E_1$  (laser) and  $E_2$  (Stokes) governed by Maxwell's equations, coupled through the process of electrostriction with an acoustic field  $\bar{\rho}$ , obeying the Navier-Stokes equation. Since our model is 1 + 1 dimensional, these three fields are represented as scalar plane waves, possessing time

---

\*abridged version of this Chapter is published in IEEE Journal of Quantum Electronics **35** (12) 1812-1816 (1999).

and propagation co-ordinates only:

$$E_1(z, t) = A_1(z, t)e^{i(k_1 z - \omega_1 t)} + c.c., \quad (3.1 a)$$

$$E_2(z, t) = A_2(z, t)e^{i(-k_2 z - \omega_2 t)} + c.c., \quad (3.1 b)$$

$$\bar{\rho}(z, t) = \rho_0 + \rho(z, t)e^{i(q_B z - \Omega_B t)} + c.c.. \quad (3.1 c)$$

In Eqs.(3.1 a-3.1 c) the frequencies and the wave-vectors satisfy energy ( $\omega_1 = \omega_2 + \Omega_B$ ) and momentum ( $k_1 = q_B - k_2$ ) conservation laws. Under the assumption of small Stokes shift ( $\omega = \omega_1 \approx \omega_2$ ) the acoustic frequency is given by  $\Omega_B = 2n\omega v/c$ , where  $v$  is the speed of hyper-sound in the medium. The slowly varying amplitude approximation is applied for both laser and Stokes fields. For the acoustic field this approximation is not valid as long as its spectral width is usually only an order of magnitude smaller than the main frequency  $\Omega_B$ . Following these remarks we write the equations in the form:

$$\frac{n}{c} \frac{\partial A_1}{\partial t} + \frac{\partial A_1}{\partial z} = i \frac{\gamma_e \omega}{2nc\rho_0} \rho A_2, \quad (3.2 a)$$

$$\frac{n}{c} \frac{\partial A_2}{\partial t} - \frac{\partial A_2}{\partial z} = i \frac{\gamma_e \omega}{2nc\rho_0} \rho^* A_1, \quad (3.2 b)$$

$$\frac{\partial^2 \rho}{\partial t^2} + (\Gamma_B - i2\Omega_B) \frac{\partial \rho}{\partial t} - i\Gamma_B \Omega_B \rho = \frac{\gamma_e q_B^2}{4\pi} A_1 A_2^*, \quad (3.2 c)$$

retaining the second order time derivative in the Navier-Stokes equation (3.2 c). The only restriction imposed on the acoustic field is the approximation of non-moving phonons, which is well justified on a time scale of several hundred picoseconds [2]. In Eqs.(3.2 a-3.2 c)  $n$  is the refractive index of the medium,  $c$  - the speed of light,  $\gamma_e$  - the electrostrictive constant,  $\rho_0$  - the unperturbed density and  $\Gamma_B$  the Brillouin line-width [2]. This set of coupled nonlinear differential equations is difficult to solve generally and analytical solutions have been found in specific situations only. The steady state solution, for example, has been extensively investigated [2, 3]. A solution in the case of undepleted pump has also been found [4]. Despite all these attempts no general approach to the problem has been proposed so far. In the following we present an analysis of the system (3.2 a-3.2 c) under no additional approximations, revealing the physical background underlying the process of transient pulse compression by SBS.

Eq.(3.2 c) we solve in the frequency domain, thus obtaining the spectrum  $\tilde{\rho}(z, \Omega)$  of the acoustic field as a function of detuning ( $\Omega$ ) from the Stokes resonance:

$$\tilde{\rho}(z, \Omega) = -\frac{\gamma_e q_B^2}{4\pi\Omega_B} \tilde{g}(\Omega) \cdot \widetilde{A_1 A_2^*}, \quad (3.3 a)$$

$$\tilde{g}(\Omega) = \frac{\Omega_B}{(\Omega - \Omega_B)^2 - \Omega_B^2 - i\Gamma_B(\Omega - \Omega_B)}, \quad (3.3 b)$$

The function  $\tilde{g}(\Omega)$  is the spectral gain profile of the SBS process possessing two resonances of widths  $\Delta\Omega_{FWHM} = \Gamma_B$  at  $\Omega = 0$  and  $\Omega = 2\Omega_B$  corresponding to Stokes and anti-Stokes scattering respectively (*see* Fig. 3.1).

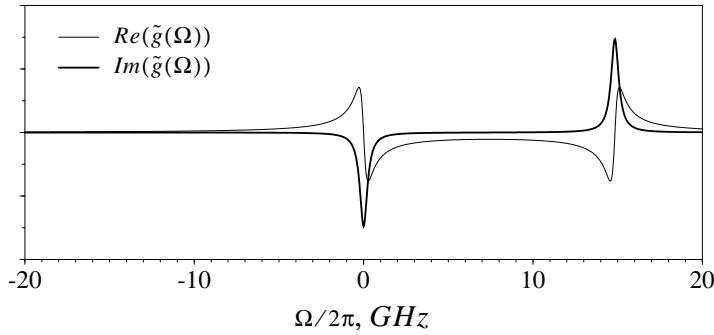


**Figure 3.1:** Real (thin line) and imaginary (thick line) parts of the SBS gain calculated for water at  $\lambda = 532$  nm. The Stokes shift is  $\Omega_B/2\pi = 7.42$  GHz. The Brillouin line-width is  $\Gamma_B = 539$  MHz

Inverse Fourier transformation of (3.3 a) and (3.3 b), performed analytically (see Appendix 3.I), gives the exact solution of the Navier-Stokes equation:

$$\rho(z, t) = -\frac{\gamma_e q_B^2}{4\pi\Omega_B} g(t) \otimes (A_1 A_2^*), \quad (3.4 a)$$

$$g(t) = \begin{cases} 0 & , t < 0 \\ \frac{-\sqrt{2\pi}\Omega_B}{\sqrt{\Omega_B^2 - \frac{\Gamma_B^2}{4}}} e^{-\frac{\Gamma_B}{2}t} e^{i\Omega_B t} \sin\left(\sqrt{\Omega_B^2 - \frac{\Gamma_B^2}{4}}t\right) & , t \geq 0 \end{cases} \quad (3.4 b)$$

where  $\otimes$  denotes convolution. The fact that the gain function (3.4 b) is zero for  $t < 0$  removes the integration over the *future* ( $\tau > t$ ) of the optical fields in (3.4 a):

$$\rho(z, t) = -\frac{\gamma_e q_B^2}{4\pi\Omega_B} \frac{1}{\sqrt{2\pi}} \int_{-\infty}^t g(t - \tau) A_1(z, \tau) A_2^*(z, \tau) d\tau. \quad (3.5)$$

This expression is a direct consequence from both the *locality* (phonon is generated at a fixed coordinate  $z$  only if at a certain moment  $t_0$  both Stokes and laser fields are present) and *inertia* of the phonons (the acoustic field exists even after the optical fields have been removed and vanishes exponentially in time (3.4 b)). The latter determines the time scale of the acousto-optical interaction known as phonon lifetime ( $\tau_p = 1/\Gamma_B$ ). It is usually regarded as a limiting factor to the pulse duration in SBS pulse compressors [6,7]. It is important to note that Eqs.(3.4 a-3.4 b) give general solution of the Navier-Stokes equation without any restriction to the time scale used. In the particular case of CW interaction (3.4 a) is transformed into the well known steady state solution where the convolution integral (3.5) is easy to solve. This results in an expression for the acoustic wave no longer depending on time:

$$\rho(z) = -\frac{\gamma_e q_B^2}{4\pi\Omega_B} A_1 A_2^* \left( -\frac{i}{\Gamma_B} \right). \quad (3.6)$$

Then the system (3.2 a,3.2 b) for the optical fields, written in terms of intensities ( $I_i = \frac{nc}{2\pi} A_i A_i^*$ ) describes a pure gain(loss) process:

$$\frac{dI_1}{dz} = -g_B I_2 I_1, \quad \frac{dI_2}{dz} = -g_B I_1 I_2, \quad (3.7)$$

where  $g_B = (\gamma_e^2 \omega^2)/(nc^3 v \rho_0 \Gamma_B)$  is the steady state Brillouin gain. The system (3.7) is discussed widely in the literature taking into account the depletion of the pump wave. It is found to describe the SBS process for CW interaction in optical fibers [5] as well as in the pulsed regime on a time scale much larger than the phonon lifetime  $\tau_p$  in the medium.

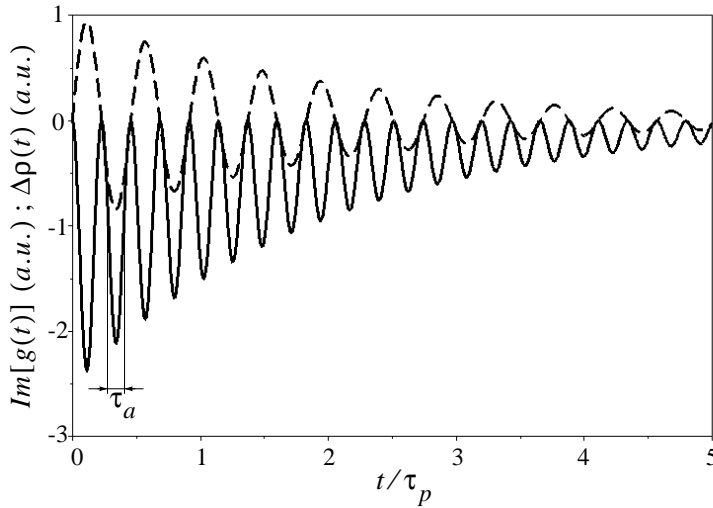


**Figure 3.2:** Imaginary part of the gain function  $g(t)$  (solid line) and the acoustic field  $\Delta\rho(t)$  (dashed line) generated by a short  $\delta$ -like pulse in water for  $\lambda = 532$  nm. Note that the ratio  $\tau_p/\tau_a$  is a material property.

Another important feature of the steady state solution appears in Eq.(3.6). The fact that the convolution integral ( $-i/\Gamma_B$ ) is both *imaginary* and *negative* leads to the pure gain(loss) system (3.7). In the opposite case when a short  $\delta$ -like pulse is propagating through a Brillouin medium, the convolution integral is proportional to the gain function  $g(t)$  itself. The analysis of its imaginary part shows (Fig. 3.2) that it is always *negative*, reaching maximum absolute values when the density deviation from  $\rho_0$  has a maximum and vanishes exponentially in time. This result is important in showing two time scales for the interaction of light pulses with a Brillouin active medium: first the decay-time of the acoustic field  $\tau_p = 1/\Gamma_B$ , and second the duration of one oscillation of the gain function equal to  $\tau_a = \pi/(2\Omega_B)$ . For pulses longer than  $\tau_p$  the interaction is limited by the decay time of the acoustic field. This effect was observed in all attempts to compress

pulses with a duration of several nano-seconds in liquid media (with phonon lifetimes in the order of several hundred pico-seconds) [6,7]. However, if the incident pulse is shorter and its duration is on the order of  $\tau_a$ , it cannot experience gain due to lack of time to build up an acoustic field. Consequently, the real physical limit to the pulse duration in a compressor setup is not the phonon lifetime  $\tau_p$ , but the acoustical half-cycle duration  $\tau_a$ . A conclusion along these lines was first drawn by Hon [1] without any mathematical derivation. Later this problem was addressed in Refs. [8–10] on a qualitative level as well.

The system (3.2 a - 3.2 c) can be rewritten in the form:

$$\frac{\partial}{\partial t} A_1(z, t) + \frac{c}{n} \frac{\partial}{\partial z} A_1(z, t) = -i\alpha \frac{c}{n} \varrho(z, t) A_2(z, t), \quad (3.8 \text{ a})$$

$$\frac{\partial}{\partial t} A_2(z, t) - \frac{c}{n} \frac{\partial}{\partial z} A_2(z, t) = -i\alpha \frac{c}{n} \varrho^*(z, t) A_1(z, t), \quad (3.8 \text{ b})$$

$$\varrho(z, t) = \frac{1}{\sqrt{2\pi}} \int_{-\infty}^t g(t - \tau) A_1(z, \tau) A_2^*(z, \tau) d\tau, \quad (3.8 \text{ c})$$

where  $\alpha = \frac{1}{2} g_B \Gamma_B$  is the coupling constant and  $\varrho = \frac{vc^2}{\gamma_e \omega} \rho$ . It was discussed in detail in [8] that under transient conditions the physically important parameter is the product  $g_B \Gamma_B$  instead of the steady state gain coefficient  $g_B$  alone. In a transient regime, the integral (3.8 c) plays an important role in the model described. It can be considered as a *memory* of the system, stored into the acoustic field  $\varrho(z, t)$  which depends strongly on the past values of the product  $A_1(z, \tau) A_2^*(z, \tau)$  for times  $\tau \in (t - \tau_p, t)$ . In the non-transient regime  $\tau_p$  is much shorter than the pulse durations and the acoustic field depends on the present values of the product  $A_1(z, t) A_2^*(z, t)$  only, thus simplifying the problem to a system which is easy to model without computing the integral (3.8 c) [7].

### 3.3 Numerical model

The system (3.8 a-3.8 c) we solve numerically by a generalization of the split-step method [5] usually used for modeling pulse propagation in optical fibers. We extended the applicability of this method to our case of two nonlinearly coupled (through the integral (3.8 c)) partial differential equations. As long as the phonons do not propagate and their lifetime cannot be neglected with respect to the pulse durations, it is obvious that the fields evolve in time only, whereas in systems with short response time (Kerr nonlinearity) the evolution in time can be replaced by evolution in space (along the  $z$  co-ordinate). Consequently, the system (3.8 a, 3.8 b) describes the evolution of the spatial distribution (along  $z$  axis) of the fields in time.

By introducing a *propagation operator*  $\hat{P} = \frac{c}{n} \frac{\partial}{\partial z}$  and a *nonlinearity operator*  $\hat{N} = -i\alpha \frac{c}{n} \varrho$ , Eqs.(3.8 a, 3.8 b) can be rewritten in vector form:

$$\frac{\partial}{\partial t} \begin{pmatrix} A_1 \\ A_2 \end{pmatrix} = \left( \begin{bmatrix} 0 & \hat{N} \\ -\hat{N}^* & 0 \end{bmatrix} + \begin{bmatrix} -\hat{P} & 0 \\ 0 & \hat{P} \end{bmatrix} \right) \begin{pmatrix} A_1 \\ A_2 \end{pmatrix}. \quad (3.9)$$

The split-step method gives an approximate solution of the Eq.(3.9) by assuming that for a small time increment  $\Delta t$  the propagation and the nonlinearity act independently

(see Fig. 3.3 a). Under this assumption the evolution of the optical fields in time is given by:

$$\begin{pmatrix} A_1(z, t + \Delta t) \\ A_2(z, t + \Delta t) \end{pmatrix} = \exp \left\{ \begin{bmatrix} 0 & \hat{N} \\ -\hat{N}^* & 0 \end{bmatrix} \Delta t \right\} \cdot \exp \left\{ \begin{bmatrix} -\hat{P} & 0 \\ 0 & \hat{P} \end{bmatrix} \Delta t \right\} \times \begin{pmatrix} A_1(z, t) \\ A_2(z, t) \end{pmatrix}. \quad (3.10)$$

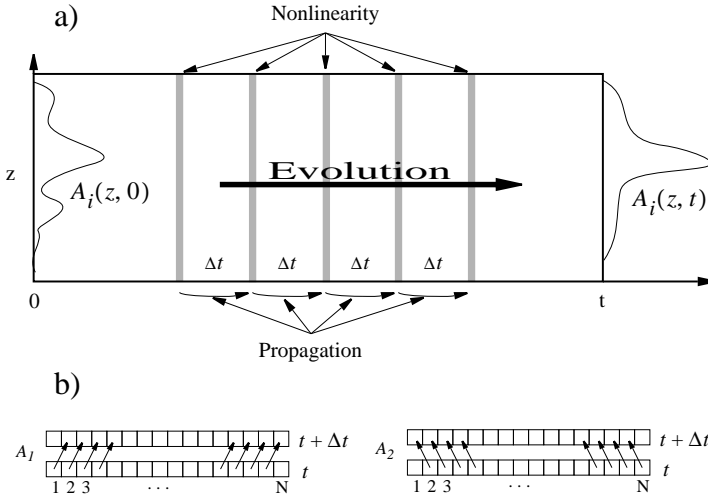


**Figure 3.3:** The split-step method; a) - the action of the propagation and the nonlinearity operators is split in time; b) - the action of the propagation operator is simply a shift in the discretization bins of the two fields ( $A_1$ -laser,  $A_2$ -Stokes) if  $\Delta z = c\Delta t/n$ .

In Eq.(3.10) the propagation exponent operator acts first, followed by the nonlinearity exponent operator as shown in Fig. 3.3 a. The fact that the operators  $\hat{P}$  and  $\hat{N}$  are non-commuting is the predominant error source in the split-step method limiting the accuracy to second order in step size  $\Delta t$  [5]. It is easy to prove that the propagation exponent operator causes a shift  $z \pm c\Delta t/n$  in the spatial part of the fields, where “+” is for the Stokes field and “-” for the laser field (see Appendix 3.II). The nonlinearity exponent operator can be presented in explicit form using trigonometric functions (see Appendix 3.II). Inserted in (3.10) this results in:

$$\begin{pmatrix} A_1(z, t + \Delta t) \\ A_2(z, t + \Delta t) \end{pmatrix} = \begin{bmatrix} \cos(\theta) & -i\frac{\rho}{|\rho|} \sin(\theta) \\ -i\frac{\rho^*}{|\rho|} \sin(\theta) & \cos(\theta) \end{bmatrix} \cdot \begin{pmatrix} A_1(z - \frac{c}{n}\Delta t, t) \\ A_2(z + \frac{c}{n}\Delta t, t) \end{pmatrix}, \quad (3.11)$$

where  $\theta = \alpha|\rho|\frac{c}{n}\Delta t$ . The implementation of Eq.(3.11) gives the time evolution of both pump and Stokes fields in each step. The method is applicable only if the spatial grid

spacing  $\Delta z$  is equal to  $c\Delta t/n$ , allowing for the introduction the spatial shifts  $z \pm c\Delta t/n$  without additional calculations (*see* Fig. 3.3b). Reducing the step size the memory consumption increases, thus limiting the speed and accuracy of the calculation. This constraint could be eliminated by using fast Fourier transformations [5] for calculation of the action of the propagation exponent operator in (3.10). In our case the computer memory available was enough to obtain good accuracy by lowering the step size. We used directly Eq.(3.11) to model the process of SBS-pulse compression. On each step the accuracy was monitored by the conservation of the number of photons. Another accuracy check necessary when using the split-step method is recalculation with two-fold reduced step size. Both checks showed good accuracy with moderate memory consumption and speed of calculation.

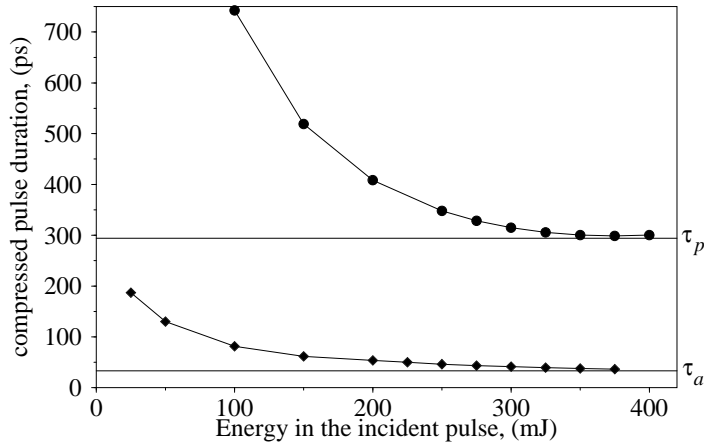


**Figure 3.4:** Calculated compressed pulse duration *vs.* energy in the incident pulse for a 10 mm beam diameter; circles - input pulse of 5 ns; diamonds - input pulse of 600 ps duration.

### 3.4 Results and Discussion

The experimental situation modeled is a generator-amplifier setup [7], where the laser beam is focused by a lens in water as a Brillouin active medium. The Stokes signal generated in the focal region propagates backwards, depleting the remainder of the pump pulse on its way [1, 7, 8]. As a result of this interaction the front edge of the Stokes pulse is amplified only, leading to pulse compression. In our model a Gaussian beam/pulse at 532 nm of 5 ns (FWHM) duration with up to 300 mJ/pulse is focused by a 10 cm lens in water. The Brillouin shift is  $\Omega_B/2\pi = 7.42$  GHz and the Brillouin line-width is  $\Gamma_B/2\pi = 539$  MHz extracted from Ref. [2] after wavelength correction for  $\lambda = 532$  nm. In Fig. 3.4 a graph of the calculated compressed pulse duration *vs.*

energy in the input pulse is presented. Circles and diamonds correspond to input pulse duration of 5 ns and 600 ps, respectively. It is clearly seen, that in case of 5 ns input pulse the limit to the pulse compression is set by the phonon lifetime  $\tau_p$ . This result is in agreement with all available experimental results on compression of long ( $\tau \gg \tau_p$ ) pulses [6, 7]. The situation is different for a 600 ps input pulse, which enters directly the transient regime. In this case our model predicts compressed pulses much shorter than  $\tau_p$ . As discussed above, the duration  $\tau_a$  of one oscillation of the gain function  $g(t)$  is assumed to be the limit to transient pulse compression. It can be seen from Fig. 3.4 that increasing the energy in the input pulse, the compressed pulse duration is indeed limited by  $\tau_a$ .

The behavior of the conversion efficiency in fully transient regime is difficult to predict on a time scale shorter than  $\tau_p$ . The Eqs.(3.4 a,3.4 b) suggest that pulses shorter than  $\tau_a$  experience reduced gain, and therefore, the conversion efficiency is considerably lower. Between the two limits our numerical experiment showed no significant deviation from 98% maximum efficiency.

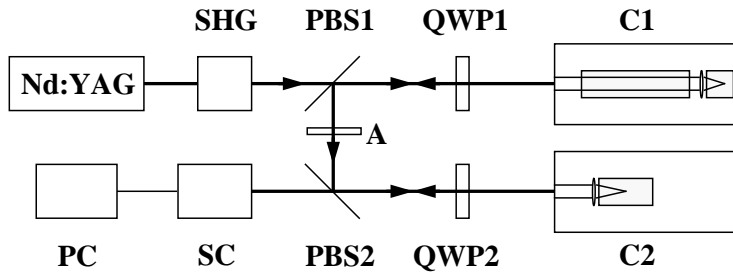


**Figure 3.5:** Experimental setup of double compressor. SHG - second harmonic generation stage, PBS - polarizing beam splitter, QWP - quarter-wave plate, A - attenuator, C - Brillouin compressor, SC - streak camera, PC - personal computer.

### 3.5 Experiment

To compress a pulse shorter than the phonon lifetime, we performed a double compression experiment. The setup is shown in Fig. 3.5. The output of injection seeded Nd:YAG laser was frequency doubled ( $\lambda = 532$  nm) and compressed to 600 ps (FWHM) with 5 mJ energy in the pulse. Water was used as Brillouin medium in a second compressor stage (C2), where the pulse was further compressed. The output pulse duration was measured with a streak camera read by computer. The uncertainty in this single-shot measurement is determined by the statistical error in the fitting procedure. In Fig. 3.6 a streak camera trace of the two-fold compressed pulse is presented, measured to be 160(10) ps (FWHM). This value is much shorter than the phonon lifetime in water  $\tau_p = 295$  ps [2], thus experimentally proving our prediction that the limit to the pulse compression in

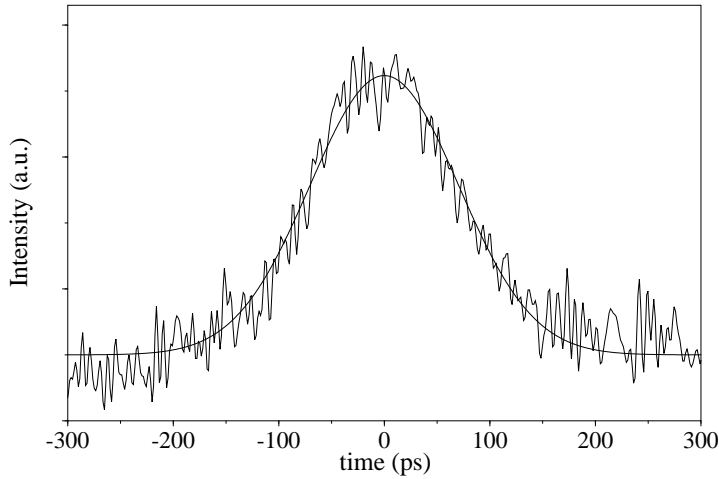


**Figure 3.6:** Streak camera trace of the secondary compressed pulse in water. The measured pulse duration (FWHM) is 160(10) ps much shorter than the phonon lifetime  $\tau_p$ .

this case is not set by the phonon lifetime. Even shorter pulses could in principle be achieved at higher pulse energies down to the theoretical limit  $\tau_a = 34$  ps for water at 532 nm. The true experimental limit, however is determined by the competition with Raman scattering and optical breakdown. The first one could be eliminated by choosing a low Raman gain liquid or an atomic gas as a Brillouin medium. The optical breakdown limitation we overcome by filtering the liquid down to 200 nm particle size, using pulses with smooth temporal profile and limiting (by the attenuator A) the energy in the second compressor stage (C2) to 5 mJ/pulse.

### 3.6 Conclusions

In conclusion we have theoretically analyzed and numerically modeled the pulse compression by stimulated Brillouin scattering in the fully transient regime. By introducing a time-dependent gain, explicitly presented by Eq.(3.4 b), we found a regime where the pulses are compressed in a half-cycle time  $\tau_a$ . In a double compression experiment we demonstrated the accessibility of the time region below  $\tau_p$  when the initial pulse duration is on the order of the phonon lifetime.

### Appendix 3.I

In this Appendix we analytically derive Eq.(3.4 b) as a Fourier-image of its spectral representation (3.3 b). In the beginning, in order to avoid any possible ambiguity regarding

the sign of the frequencies in the Fourier domain, we shall define direct and inverse Fourier transformations as follows:

$$\text{direct Fourier transform} \quad \tilde{\Psi}(\Omega) = \mathcal{F}(\Psi(t)) = \frac{1}{\sqrt{2\pi}} \int_{-\infty}^{\infty} \Psi(t) e^{-i\Omega t} dt, \quad (3.12 \text{ a})$$

$$\text{inverse Fourier transform} \quad \Psi(t) = \mathcal{F}^{-1}(\tilde{\Psi}(\Omega)) = \frac{1}{\sqrt{2\pi}} \int_{-\infty}^{\infty} \tilde{\Psi}(\Omega) e^{i\Omega t} d\Omega. \quad (3.12 \text{ b})$$

Then, according to this definition, we can write an expression for Dirac's  $\delta$ -function:

$$\delta(t) = \frac{1}{2\pi} \int_{-\infty}^{\infty} e^{i\Omega t} d\Omega, \quad (3.13 \text{ a})$$

$$\tilde{\delta}(\Omega) = \frac{1}{\sqrt{2\pi}}, \quad (3.13 \text{ b})$$

and convolution:

$$\Psi_1(t) \otimes \Psi_2(t) = \frac{1}{\sqrt{2\pi}} \int_{-\infty}^{\infty} \Psi_1(t - \tau) \Psi_2(\tau) d\tau. \quad (3.14)$$

First and second derivative operators in the frequency domain are simply multiplication by  $i\Omega$  and  $-\Omega^2$ , respectively, which applied to the Navier-Stokes equation (3.2 c) lead to the expression (3.3 a). The inverse Fourier transform of the spectral gain profile (3.3 b) can be performed analytically, involving (according to Eq. (3.12 b)) the solution of the integral:

$$g(t) = \frac{1}{\sqrt{2\pi}} \int_{-\infty}^{\infty} \frac{\Omega_B e^{i\Omega t}}{(\Omega - \Omega_B)^2 - \Omega_B^2 - i\Gamma_B(\Omega - \Omega_B)} d\Omega = \frac{1}{\sqrt{2\pi}} \oint_L f(\hat{\Omega}) d\hat{\Omega}. \quad (3.15)$$

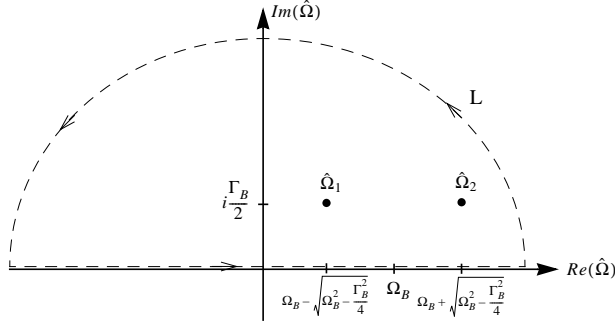


**Figure 3.7:** Integration contour for calculation of the inverse Fourier transform of (3.3 b)

The integrand in (3.15) is the complex function:

$$f(\hat{\Omega}) = \frac{\Omega_B e^{i\hat{\Omega} t}}{(\hat{\Omega} - \hat{\Omega}_1)(\hat{\Omega} - \hat{\Omega}_2)}, \quad (3.16)$$

which has two poles:

$$\begin{aligned}\hat{\Omega}_1 &= \Omega_B - \sqrt{\Omega_B^2 - \frac{\Gamma_B^2}{4}} + i\frac{\Gamma_B}{2}, \\ \hat{\Omega}_2 &= \Omega_B + \sqrt{\Omega_B^2 - \frac{\Gamma_B^2}{4}} + i\frac{\Gamma_B}{2},\end{aligned}$$

shown as dots in Fig. 3.7. The integration we perform along the contour  $L$  depicted in Fig. 3.7 as well. Since  $f(\hat{\Omega})$  is analytical in the upper semi-plane ( $Im(\hat{\Omega}) > 0$ ) if  $t \geq 0$ , for  $t < 0$  the whole integral is zero. After the integration using the *Theorem of residues*, Eq.(3.15) transforms into:

$$g(t) = \frac{1}{\sqrt{2\pi}} \oint_L f(\hat{\Omega}) d\hat{\Omega} = \begin{cases} 0 & , t < 0 \\ \sqrt{2\pi}i \left( \text{Res}f(\hat{\Omega})|_{\hat{\Omega}=\hat{\Omega}_1} + \text{Res}f(\hat{\Omega})|_{\hat{\Omega}=\hat{\Omega}_2} \right) & , t \geq 0 \end{cases} \quad (3.17)$$

The sum of the two residues is:

$$\begin{aligned}\sum_{j=1}^2 \text{Res}f(\hat{\Omega})|_{\hat{\Omega}=\hat{\Omega}_j} &= \frac{\Omega_B}{\hat{\Omega}_2 - \hat{\Omega}_1} (e^{i\hat{\Omega}_2 t} - e^{i\hat{\Omega}_1 t}) = \\ &= \frac{i\Omega_B}{\sqrt{\Omega_B^2 - \frac{\Gamma_B^2}{4}}} e^{-\frac{\Gamma_B}{2}t} e^{i\Omega_B t} \sin\left(\sqrt{\Omega_B^2 - \frac{\Gamma_B^2}{4}}t\right),\end{aligned}$$

which inserted into (3.17) leads to:

$$g(t) = \begin{cases} 0 & , t < 0 \\ \frac{-\sqrt{2\pi}\Omega_B}{\sqrt{\Omega_B^2 - \frac{\Gamma_B^2}{4}}} e^{-\frac{\Gamma_B}{2}t} e^{i\Omega_B t} \sin\left(\sqrt{\Omega_B^2 - \frac{\Gamma_B^2}{4}}t\right) & , t \geq 0 \end{cases}$$

## Appendix 3.II

This Appendix is devoted to the derivation of the evolution equation (3.11) from the vectorial differential equation (3.9). It is in the heart of the split-step method to separate the action of the free propagation

$$[\tilde{\mathcal{P}}] = \begin{bmatrix} -\hat{P} & 0 \\ 0 & \hat{P} \end{bmatrix}, \quad \hat{P} = \frac{c}{n} \frac{\partial}{\partial z} \quad (3.18)$$

and the nonlinearity

$$[\tilde{\mathcal{N}}] = \begin{bmatrix} 0 & \hat{N} \\ -\hat{N}^* & 0 \end{bmatrix}, \quad \hat{N} = -i\alpha \frac{c}{n} \rho. \quad (3.19)$$

within each step  $\Delta t$ . Then our differential equation (3.9) has the form:

$$\frac{\partial}{\partial t} \begin{pmatrix} A_1(z, t) \\ A_2(z, t) \end{pmatrix} = ([\tilde{\mathcal{N}}] + [\tilde{\mathcal{P}}]) \cdot \begin{pmatrix} A_1(z, t) \\ A_2(z, t) \end{pmatrix}$$

with a solution:

$$\begin{aligned} \begin{pmatrix} A_1(z, t + \Delta t) \\ A_2(z, t + \Delta t) \end{pmatrix} &= \exp([\tilde{\mathcal{N}}]\Delta t + [\tilde{\mathcal{P}}]\Delta t) \cdot \begin{pmatrix} A_1(z, t) \\ A_2(z, t) \end{pmatrix} = \\ &= \exp([\tilde{\mathcal{N}}]\Delta t) \cdot \exp([\tilde{\mathcal{P}}]\Delta t) \cdot \begin{pmatrix} A_1(z, t) \\ A_2(z, t) \end{pmatrix}, \end{aligned} \quad (3.20)$$

which is equivalent to Eq. (3.10). The action of the propagation exponent operator  $\exp([\tilde{\mathcal{P}}]\Delta t)$  can be performed in the Fourier space, where differentiation is simply multiplication by  $i\Omega_z$ .

$$\begin{aligned} \exp([\tilde{\mathcal{P}}]\Delta t) \begin{pmatrix} A_1(z, t) \\ A_2(z, t) \end{pmatrix} &= \mathcal{F}_{(z)}^{-1} \begin{bmatrix} e^{-i\Omega_z \frac{c}{n} \Delta t} & 0 \\ 0 & e^{i\Omega_z \frac{c}{n} \Delta t} \end{bmatrix} \mathcal{F}_{(\Omega_z)} \begin{pmatrix} A_1(z, t) \\ A_2(z, t) \end{pmatrix} = \\ &= \mathcal{F}_{(z)}^{-1} \begin{bmatrix} e^{-i\Omega_z \frac{c}{n} \Delta t} \tilde{A}_1(\Omega_z, t) & 0 \\ 0 & e^{i\Omega_z \frac{c}{n} \Delta t} \tilde{A}_2(\Omega_z, t) \end{bmatrix} = \\ &= \frac{1}{\sqrt{2\pi}} \begin{bmatrix} \int_{-\infty}^{\infty} \tilde{A}_1(\Omega_z, t) e^{i\Omega_z(z - \frac{c}{n} \Delta t)} d\Omega_z & 0 \\ 0 & \int_{-\infty}^{\infty} \tilde{A}_2(\Omega_z, t) e^{i\Omega_z(z + \frac{c}{n} \Delta t)} d\Omega_z \end{bmatrix} = \\ &= \begin{pmatrix} A_1(z - \frac{c}{n} \Delta t, t) \\ A_2(z + \frac{c}{n} \Delta t, t) \end{pmatrix}. \end{aligned} \quad (3.21)$$

The latter shows that the free propagation due to the operator  $\hat{P} = \frac{c}{n} \frac{\partial}{\partial z}$  causes a shift of  $\frac{c}{n} \Delta t$  in the spatial part of the field.

The nonlinearity exponent operator  $\exp([\tilde{\mathcal{N}}]\Delta t)$ , which appears on the right-hand side of Eq. (3.20), can be expressed in a terms of a single matrix, using the following relations for the odd and even powers of  $[\tilde{\mathcal{N}}]\Delta t$ :

$$\begin{aligned} ([\tilde{\mathcal{N}}]\Delta t)^{2n} &= (-1)^n |\hat{N}|^{2n} \Delta t^{2n} [\tilde{\mathbf{1}}], \quad [\tilde{\mathbf{1}}] = \begin{bmatrix} 1 & 0 \\ 0 & 1 \end{bmatrix}; \\ ([\tilde{\mathcal{N}}]\Delta t)^{2n+1} &= (-1)^n |\hat{N}|^{2n+1} \Delta t^{2n+1} \frac{[\tilde{\mathcal{N}}]}{|\hat{N}|}, \quad |\hat{N}| = \alpha \frac{c}{n} |\varrho|. \end{aligned}$$

The Taylor's expansion for the exponent gives:

$$\begin{aligned}
\exp([\tilde{\mathcal{N}}]\Delta t) &= \sum_{n=0}^{\infty} \frac{([\tilde{\mathcal{N}}]\Delta t)^n}{n!} = \\
&= \left( \sum_{n=0}^{\infty} \frac{(-1)^n |\hat{N}|^{2n} \Delta t^{2n}}{(2n)!} \right) [\tilde{\mathbf{1}}] + \left( \sum_{n=0}^{\infty} \frac{(-1)^n |\hat{N}|^{2n+1} \Delta t^{2n+1}}{(2n+1)!} \right) \frac{[\tilde{\mathcal{N}}]}{|\hat{N}|} = \\
&= \cos(|\hat{N}|\Delta t)[\tilde{\mathbf{1}}] + \frac{\sin(|\hat{N}|\Delta t)}{|\hat{N}|} [\tilde{\mathcal{N}}] = \begin{bmatrix} \cos(\alpha|\varrho|\frac{c}{n}\Delta t) & \frac{-i\varrho}{|\varrho|} \sin(\alpha|\varrho|\frac{c}{n}\Delta t) \\ \frac{-i\varrho^*}{|\varrho|} \sin(\alpha|\varrho|\frac{c}{n}\Delta t) & \cos(\alpha|\varrho|\frac{c}{n}\Delta t) \end{bmatrix}. \quad (3.22)
\end{aligned}$$

Substitution of (3.21) and (3.22) into Eq. (3.20) yields the evolution equation (3.11).

### Acknowledgment

This work was financially supported by the Netherlands Foundation for Fundamental Research on Matter (FOM).

### References

- [1] D. T. Hon, *Opt. Lett.* **5**, 516 (1980).
- [2] R. W. Boyd, *“Nonlinear Optics”* (Academic, 1996), Chapter 8.
- [3] W. Kaiser, M. Maier, *“Laser Handbook”* (North-Holland, Amsterdam 1972) vol. 2.
- [4] D. N. Ghosh Roy, D. V. G. L. N. Rao, *J. Appl. Phys.* **59**, 332 (1986).
- [5] G. P. Agrawal, *“Nonlinear Fiber Optics”* (Academic, 1995).
- [6] C. Brent Dane, W. A. Neuman, L. A. Hackel, *IEEE J. Quantum Electron.* **30**, 1907 (1994) (and references therein).
- [7] S. Schiemann, W. Ubachs, W. Hogervorst, *IEEE J. Quantum Electron.* **33**, 358 (1997).
- [8] M. J. Damzen, H. Hutchinson, *IEEE J. Quantum Electron.* **19**, 7 (1983).
- [9] V. A. Gorbunov, S. B. Papernyi, V. F. Petrov, V. R. Startsev, *Sov. J. Quantum Electron.* **13**, 900 (1983).
- [10] R. Fedosejevs, A. A. Offenberger, *IEEE J. Quantum Electron.* **21**, 1558 (1985).



# Chapter 4

## Higher-order stimulated Brillouin scattering with Bessel beams.\*

We report on an experimental investigation of stimulated Brillouin scattering pumped with a Bessel beam. Due to the extended interaction length along the diffraction-free propagation, higher-order Stokes components are generated in a bulk Brillouin-active medium with odd and even orders propagating in opposite directions. The spatial, spectral and temporal properties of the interacting waves are discussed.

### 4.1 Introduction

Stimulated Brillouin scattering (SBS) first attracted the attention of the laser-physics community by its phase conjugation properties, an effect widely used for wavefront correction in powerful amplifier systems. In the 1970s SBS was studied in optical fibers, where long interaction lengths can be achieved, lowering significantly the SBS threshold. Effects as higher-order Stokes and anti-Stokes generation [1], four-wave-mixing and self-phase modulation were investigated [2]; the concepts of a Brillouin fiber-laser and Brillouin mode-locking were also introduced [3]. In the 1980s the first experimental observation of pulse compression by SBS was published [4], which triggered a great interest with the prospect of achieving high peak intensities with nearly 100% conversion efficiency. During the two decades that followed, pulse energies of more than 1 J were compressed [5], sub-phonon lifetime pulses were achieved [6], and compression ratios greater than 20 realized using Gaussian beams.

In the late 1980s the concept of diffraction-free beams was introduced by Durnin *et al.* [7]. They pointed out that the Helmholtz equation, apart from its trivial plane-wave solution, possesses a whole class of diffraction-free solutions, the simplest of them being a monochromatic wave propagating along the  $z$  axis with amplitude:

$$\Phi(\rho, \theta, z; k) = \exp(i\beta z) J_0(\alpha \rho), \quad (4.1)$$

where  $\rho^2 = x^2 + y^2$ ,  $\alpha^2 + \beta^2 = k^2$  and  $J_0$  is the zero-order Bessel function. This wave has a central maximum with half-width  $\sim \alpha^{-1}$  surrounded by concentric ring-shaped maxima with amplitudes decaying as  $\rho^{-1/2}$ . The total energy of such beam is infinite, since each lobe carries approximately the same energy as the preceding one [8]. Alternatively, in the Fourier-space, a beam defined by Eq. (4.1), can be considered as a superposition of infinite number of plane waves (each carrying infinite energy) with

---

\*Opt. Lett. **26** (8), 530-532 (2001).

wave-vectors lying on the surface of a cone. This fact makes it practically impossible to generate a non-diffracting beam over an infinite propagation distance.

If the Bessel beam is modulated by a Gaussian function  $\exp(-\rho^2/w^2)$ , the total energy in the beam is finite. This makes Bessel-Gauss beams [9] experimentally feasible and limits the diffraction-free propagation to distances  $L = w/\gamma$ , where  $\gamma$  is the angular half-aperture of the cone of the Bessel beam ( $\alpha = k \sin(\gamma)$ ). A Bessel-Gauss beam with  $w = 5$  mm and cone angle of  $2\gamma = 2.5^\circ$  is nearly non-diffracting over a distance  $L \approx 25$  cm, creating an intense line-focus with constant diameter of few micrometers. The application of such a beam in nonlinear processes offers a number of unique possibilities [10–17]. Important advantages of Bessel pump beams over Gaussian ones are: *i* the scattering products in the far field can be spatially separated from the pump beam; *ii* the pump beam experiences no self-phase-modulation, due to the fact that it traverses the long line-focus at an angle, resulting in high peak power interaction length on the order of the line-focus diameter (i.e. few microns), whereas for the on-axis scattered beam the interaction length is  $\sim L$ . In the case of third-harmonic generation the non-collinear phase-matching within the conical beam showed the novel effect of self-phase-matching [10,11], which led to high ( $\sim 1.5\%$ ) tripling efficiencies achieved in experiments [10,12]. Stimulated Raman scattering has been investigated as well [13–16] and higher-order Stokes and anti-Stokes components have been observed on axis and on cones of different apex angles. The spatial separation in the far field proved important in the case of stimulated Rayleigh-wing scattering, where the frequency-shifted forward-scattered signal was observed on axis and its spatial and spectral properties investigated [17]. In this Chapter we present experimental results on the properties of SBS, pumped with a Bessel beam.

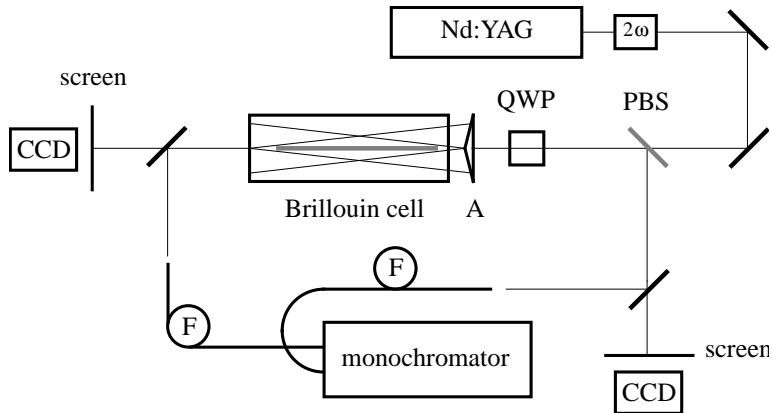


**Figure 4.1:** Scheme of the experimental setup: PBS - polarization beam-splitter; QWP - quarter wave-plate; A -  $2.5^\circ$  quartz axicon; CCD - CCD-camera for beam profile recording; F - bare-tip single-mode fiber. A double fiber-input monochromator is used for frequency measurements.

## 4.2 Experimental setup

The experimental setup is shown in Fig. 4.1. A frequency doubled, Q-switched and injection seeded Nd:YAG laser (Quanta Ray GCR-330) provides Fourier-transform limited pulses of 6 ns duration at 532 nm. The Gaussian beam of 8 mm diameter passing through a quartz axicon (conical lens) with an apex angle of  $175^\circ$  is converted into a nearly Bessel-Gauss beam of  $w = 5$  mm and  $\gamma \approx 1.25^\circ$ . The entire region of diffraction-free propagation is covered by a 30 cm Brillouin cell filled with distilled and filtered (200 nm particle size) water. In our experiment water was preferentially used for its moderate Brillouin gain  $g_B = 0.0048$  cm/MW, low phonon lifetime  $\tau \approx 300$  ps, relatively large Brillouin shift  $\Omega_B = 7.4$  GHz [18] and low Raman gain. Liquids like acetone, methanol and ethanol exhibit an order of magnitude higher Brillouin gain [18], but the competition with Raman scattering at very low powers makes them not suitable for Brillouin scattering experiments. The backscattered beam is extracted by its polarization. The beam profiles of both the forward and backward scattered beams are recorded with a CCD camera. Light from localized regions within both forward and backward scattered beams is extracted by bare-tip single-mode fibers and transported into a grating monochromator equipped with CCD camera at the exit for spectral analysis. Multi-mode fibers were used in order to send light for pulse duration measurements on a fast photodiode (Hamamatsu G4176 - 100 ps) read by a fast digitizing oscilloscope (Tektronix TD680B - 1 GHz, 5 Gs).

## 4.3 Results and discussion

First, the phase-conjugation property of the Stokes signal was investigated. As shown in Fig. 4.2a the backscattered beam has a ring shape unlike the Gaussian pump beam, reflection of which is placed on the right-hand side of the SBS beam. No phase conjugation was observed just above the SBS threshold. This can be explained in the following way: due to the non-collinear phase-matching in the Brillouin cell, a backscattered signal is generated on axis, hence a strong Gaussian-like backward scattered Stokes beam is created and after passing again through the axicon is transformed into a Bessel-Gauss beam, which in the far-field has a ring shape (Fig. 4.2a) and divergence  $\approx 10$  mrad. It is somewhat less than the pump-beam divergence of  $\approx 17$  mrad (Fig. 4.2c), due to the intrinsic initial divergence of the SBS beam emerging from the narrow line-focus in the cell. After increasing the pump-pulse energy the backward propagating first Stokes reaches threshold for second-order Stokes generation in forward direction - a highly-directional Gaussian-like beam seen in the center of Fig. 4.2d. The spectrum of the forward on-axis beam is shown in Fig. 4.3a, where a single line, shifted by  $-2\Omega_B$  from the laser frequency  $\omega_L$ , is seen. Further increase of the input pulse energy leads to reaching a third threshold when the second-order Stokes pulse due to its extended propagation distance in the line-focus can generate a third-order Stokes pulse in the backward direction. A spectrum of the backscattered beam is shown in Fig. 4.3b, where the presence of two frequencies  $\omega_L - \Omega_B$  and  $\omega_L - 3\Omega_B$  is evident. In order to visualize better the position of the odd-order Stokes frequencies we focused the backscattered beam, containing the

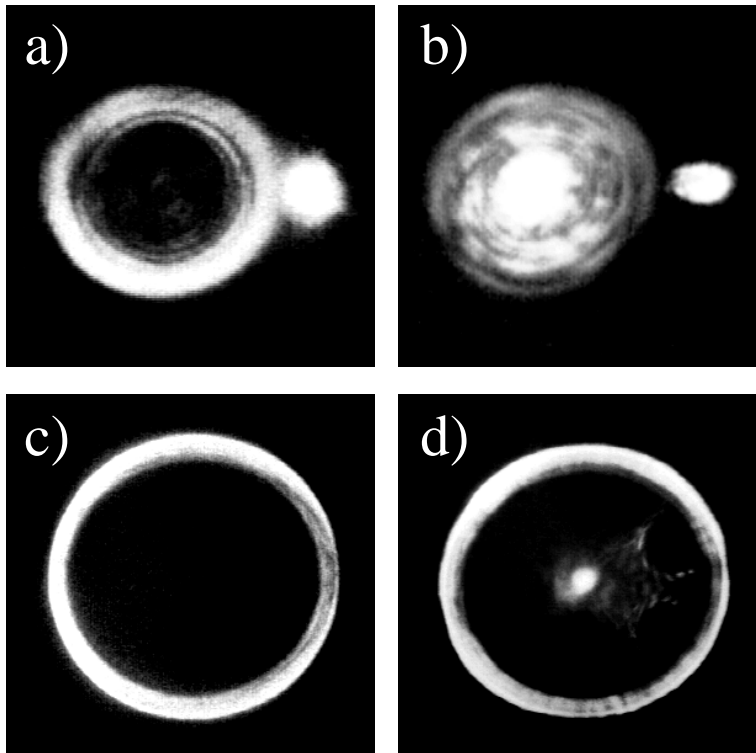


**Figure 4.2:** Far-field images of the output beams: a) backward SBS at low peak power above the threshold (no phase conjugation); b) backward SBS at high energy in the pulse; c) pump beam; d) pump beam (ring) and second SBS (central spot) above the second threshold.

first and third-order Stokes, into the single-mode fiber used as input for the monochromator. Due to forward four-wave-mixing in the fiber [2] many equidistant frequencies, separated by  $2\Omega_B$  are generated, forming the frequency ‘ruler’ shown in Fig. 4.3c.

By increasing the pump pulse energy the backscattered output beam changes its intensity distribution featuring an intense central maximum surrounded by a halo (Fig. 4.2b), again far from phase-conjugation as compared to the input beam. By increasing the peak intensity not only the central lobe, but also adjacent secondary rings reach SBS threshold in the colinear phase-matching geometry, thus providing conditions for better phase-conjugation. This effect was more clearly observed, when the ring beam, created by the axicon was sharply focused into the Brillouin cell. The line-focus in that case was very short (equal to the Rayleigh range of the envelope Gaussian beam), thus none of the higher-order interactions, described above could take place. The output

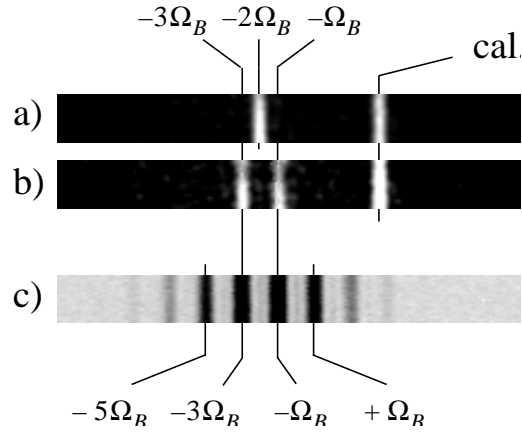


**Figure 4.3:** Spectra, recorded by the grating monochromator: a) - central spot in forward direction where second Stokes frequency is visible; b) - backward scattered beam with third and first Stokes frequencies; c) - four-wave-mixing inside the fiber used as a ‘ruler’ for the relative frequency measurements. The line, denoted by *cal.* is a reference frequency.

SBS beam observed was phase-conjugated to the input beam. In this study, however, we are interested in the SBS with diffraction-free beams while the latter case, although leading to improved phase-conjugation, is a Gauss-dominated Bessel-Gauss beam, which is similar to most experimental realizations of phase conjugation with phase-distorted Gaussian beams.

Temporal profile measurements of typical pulses recorded in backward (Fig. 4.4a) and forward (Fig. 4.4b,c) direction reveal similarities with SBS in optical fibers. In Fig. 4.4a and Fig. 4.4b regular sub-pulses are clearly seen, separated by  $\approx 1.3$  ns, which is exactly the line-focus length  $L$  in the Brillouin cell. The formation of sub-structure can be considered as an onset of Brillouin mode-locking, analogous to the same effect observed in optical fibers [3]. The advantage of using a Bessel beam in a bulk medium is, however, that high energy pulses can be studied without self-phase-modulation or optical damage in a gain-guided geometry [15]. In Fig. 4.4c the pulse shapes, recorded in the inner (dashed line) and the outer (solid line) part of the forward ring are shown (*see also* Fig. 4.2d). The inner part of the ring, being an image of the wings of the Gaussian pump beam, does not reach SBS threshold (due to its low intensity) and, therefore, the pulse-shape reproduces exactly the pump pulse. The outer part of the ring is an image of the central part of the pump beam, and is therefore affected by the interaction - the sharp cut-off observed reflects the onset of the SBS process. In contrast to SBS with Gaussian beams, where practically all the pump energy is transferred into the backward Stokes beam, in our case, due to the second-order Stokes generation, the forward output efficiency remains high.

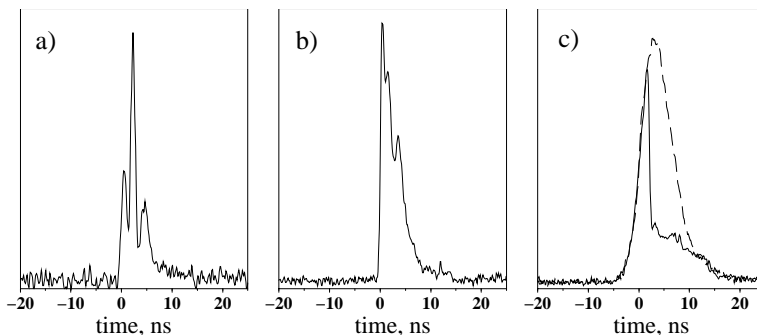


**Figure 4.4:** Typical temporal pulse shapes: a) backward scattered pulse; b) forward scattered second Stokes; c) pulse shape in the forward ring - the outer part (solid line) takes part in the stimulated scattering, whereas the inner part (dashed line) is not affected by the interaction.

## 4.4 Conclusions

In conclusion, we have investigated the spatial, spectral and temporal properties of the process of stimulated Brillouin scattering pumped by a Bessel-Gauss beam. The poor phase-conjugation fidelity of the backscattered signal is attributed to the non-colinear nature of the scattering process, involving a conical beam. Due to the extended ( $\approx 30$  cm) interaction region, along the diffraction-free propagation of the pump beam, a unique possibility to observe higher-order SBS is created, which in case of focused Gaussian beam is not feasible in pure form. Stokes orders as high as third were recorded.

### Acknowledgments

The authors are grateful to V. Tugbaev (Minsk) for providing the axicon and to Netherlands Foundation for Fundamental Research on Matter (FOM) for financial support.

### References

- [1] K.O. Hill, D.C. Johnson, B.S. Kawasaki, *Appl. Phys. Lett.* **29**, 185 (1976).
- [2] P. Labudde, P. Anliker, H.P. Weber, *Opt. Commun.* **32**, 385 (1980).
- [3] B.S. Kawasaki, D.C. Johnson, Y. Fujii, K.O. Hill, *Appl. Phys. Lett.* **32**, 429 (1978).
- [4] D.T. Hon, *Opt. Lett.* **5**, 516 (1980).
- [5] C. Brent Dane, W.A. Newman, L.A. Hackel, *IEEE J. Quantum Electron.* **30**, 1907 (1994).
- [6] I. Velchev, D. Neshev, W. Hogervorst, W. Ubachs, *IEEE J. Quantum Electron.* **35**, 1812 (1999).
- [7] J. Durnin, J.J. Miceli Jr., J.H. Eberly, *Phys. Rev. Lett.* **58**, 1499 (1987); *J. Opt. Soc. Am. A* **4**, 651 (1987).
- [8] J. Durnin, J.J. Miceli Jr., J.H. Eberly, *Opt. Lett.* **13**, 79 (1988).

- 
- [9] F. Gori, G. Guattari, C. Padovani, *Opt. Commun.* **64**, 491 (1987).
  - [10] B. Glushko, B. Kryzhanovsky, and D. Sarkisyan, *Phys. Rev. Lett.* **71**, 243 (1993).
  - [11] S.P. Tewari, H. Huang, R.W. Boyd, *Phys. Rev. A* **51**, R2707 (1995).
  - [12] C. Altucci, R. Bruzzese, D. D'Antuoni, C. de Lisio, S. Solimeno, *J. Opt. Soc. Am. B* **17**, 34 (2000).
  - [13] S. Klewitz, P. Leiderer, S. Herminghaus, S. Sogomonian, *Opt. Lett.* **21**, 248 (1996)
  - [14] L. Niggel and M. Maier, *Opt. Lett.* **22**, 910 (1997).
  - [15] L. Niggel and M. Maier, *Opt. Commun.* **154**, 65 (1998).
  - [16] V. Vaičaitis, A. Stabinis, A. Marcinkevičius, V. Jaritus, *Opt. Commun.* **178**, 461 (2000);
  - [17] S. Sogomonian, R. Barillè, G. Rivoare, *Opt. Commun.* **157**, 182 (1998); R. Barillè, S. Sogomonian, G. Rivoare, *J. Opt. Soc. Am. B* **16**, 1139 (1999).
  - [18] R.W. Boyd, *“Nonlinear Optics”* (Academic press, 1992).



## Chapter 5

# A Dense Grid of Reference Iodine Lines for Optical Frequency Calibration in the Range 571-596 nm.\*

A high precision dense grid of reference lines in the hyperfine structure of the  $B-X$  system of molecular iodine ( $^{127}\text{I}_2$ ) is presented. A simple parameterization has been derived, predicting the hyperfine line positions of the “t” components for vibrational bands (13-1) up to (18-1) and rotational quantum numbers  $J=(9-140)$ . The analysis in this Chapter is based on Doppler-free saturation spectroscopy spectra used for calibration of more than 100 new components in the hyperfine structure of  $^{127}\text{I}_2$ . The data presented contains a prediction (with 2 MHz accuracy) for the positions of 1584 “t” components in the rotational structure of iodine, covering the wavelength interval 571-596 nm.

### 5.1 Introduction

In a large part of the optical spectrum, extending from the green to the near infrared (500-900 nm) the absorption spectrum of molecular iodine [1–3] has become a convenient reference standard for calibration purposes and is widely used in laser spectroscopic studies. Throughout the entire range this Doppler broadened absorption spectrum (with an absolute accuracy of 60 MHz [4]) provides a suitable accuracy for studies in which pulsed dye lasers are employed. Particularly the fact that iodine has several lines per  $\text{cm}^{-1}$  makes this molecule such a useful standard. However, for precision measurements with CW-lasers that have typical bandwidths of 1 MHz the accuracy provided by the Doppler broadened lines is insufficient. Even in precision experiments where pulsed-dye amplified lasers of 100 MHz bandwidth are used [5–8] the  $\text{I}_2$ -reference lines are the limiting factor to the accuracy.

For higher precision experiments the iodine molecule remains a good candidate for a wavelength standard. Individual hyperfine components of rotational lines measured by saturation spectroscopy provide a reliable and reproducible standard that is even used in the *mise en pratique* of the definition of the Metre [9]. Over the years several of such lines were calibrated with sub-MHz accuracy, usually for specific purposes in precision experiments [10–19]. Recently Sansonetti [20] reported the calibration of 102  $\text{I}_2$ -hyperfine components in the yellow-red range of the spectrum with sub-MHz accuracy, thus providing a useful tool for calibration. Still this collection is insufficient for on-line calibration in many laser spectroscopic studies, mainly due to the large (up to  $50 \text{ cm}^{-1}$  in Ref. [20]) gaps between the lines. Most CW-lasers allow for continuous scans of only

---

\*Journal of Molecular Spectroscopy **187** (1) 21-27 (1998).

one or few  $\text{cm}^{-1}$ ; moreover the accuracy is lost when multiply overlapping scans are necessary to reach a calibrated line.

In the present study we present a grid of reference iodine ( $^{127}\text{I}_2$ ) lines, which is accurate (2 MHz absolute accuracy) and dense (at least one reference line in each  $\text{cm}^{-1}$ ). The accuracy of this standard is dependent on previous absolute calibrations as well as on the unperturbed molecular structure of the  $B-X$  system of the  $^{127}\text{I}_2$ -molecule. The rotational structure and the hyperfine structure in the (13-1), (14-1), (15-1), (16-1), (17-1) and (18-1) bands of the  $B-X$  system is analyzed for  $P(J)$  and  $R(J)$  lines up to  $J = 140$ . Molecular parameters are derived that predict line positions of individual hyperfine components to within 2 MHz. If only a single hyperfine component per rotational line is counted, this procedure yields more than 1500 useful reference lines in a range of about  $700 \text{ cm}^{-1}$ , covering the wavelength range 571-596 nm. This standard represents more than an order of magnitude improvement over the accuracy of the  $\text{I}_2$ -atlas and should be useful in many studies where high precision is required.

## 5.2 Experimental

The experimental setup is schematically shown in Fig. 5.1. A stabilized CW ring-dye-laser (Spectra-Physics 380D) running on Rhodamine 6G and continuously tunable over  $1 \text{ cm}^{-1}$  supplies the narrow bandwidth ( $\sim 1 \text{ MHz}$ ) radiation. The laser beam is split, as shown in Fig. 5.1, and about 10 mW is used for recording  $\text{I}_2$ -saturation spectra. Differential absorption is monitored on two photodiodes, where one of the probe beams is overlapped in the  $\text{I}_2$ -cell ( $\sim 10 \text{ cm}$  length) with a mechanically chopped (800 Hz) saturating beam. The differential signal is electronically filtered and stored in a computer. The sealed  $\text{I}_2$ -cell is used at room temperature vapour pressure. From the kHz-precision studies of Bordé *et al.* [21] we conclude that at our measuring conditions aiming at an accuracy of 2 MHz no pressure-induced or intensity-induced effects play a role.

Apart from the purpose of a coarse tuning needed to identify the resonances, no absolute wavelength measurements were performed in our experiment. The concept of the present method involves only relative frequency measurements with a stabilized (75 cm length) etalon with respect to calibrated absolute frequency points derived from the literature [18, 20]. The etalon is pressure and temperature stabilized and further actively locked to the output of a He-Nelaser (Fig 5.1). A  $^3\text{He}$ - $^{22}\text{Ne}$  laser is actively locked to the “B”-component of  $^{129}\text{I}_2$  following the procedures of Schweitzer *et al.* [22]. Before each measurement session the Free Spectral Range (FSR) of the etalon is determined, resulting in values of 148.9560(5) MHz, with small day-to-day variations. For this purpose accurately calibrated  $\text{I}_2$ -lines Refs. [13, 18, 20] were used. It is essential for a derivation of absolute frequencies that both the He-Ne laser and the etalon are kept in lock during an entire measurement session.

Subsequently computer-controlled scans of  $\text{I}_2$ -lines were recorded in saturated absorption, with simultaneous detection of marker fringes of the etalon. In some cases overlapping scans were used to record the desired spectral line. After linearization of the scan by fitting a spline function through the marker positions, the relative position

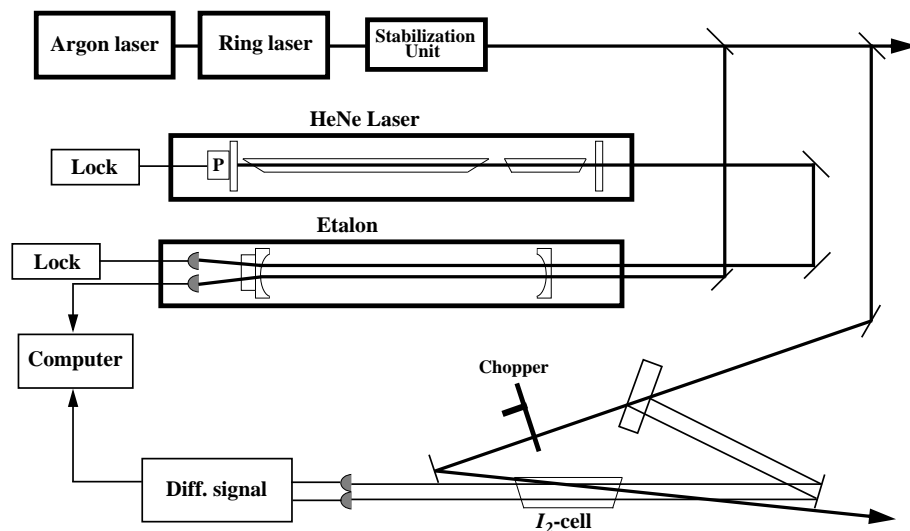
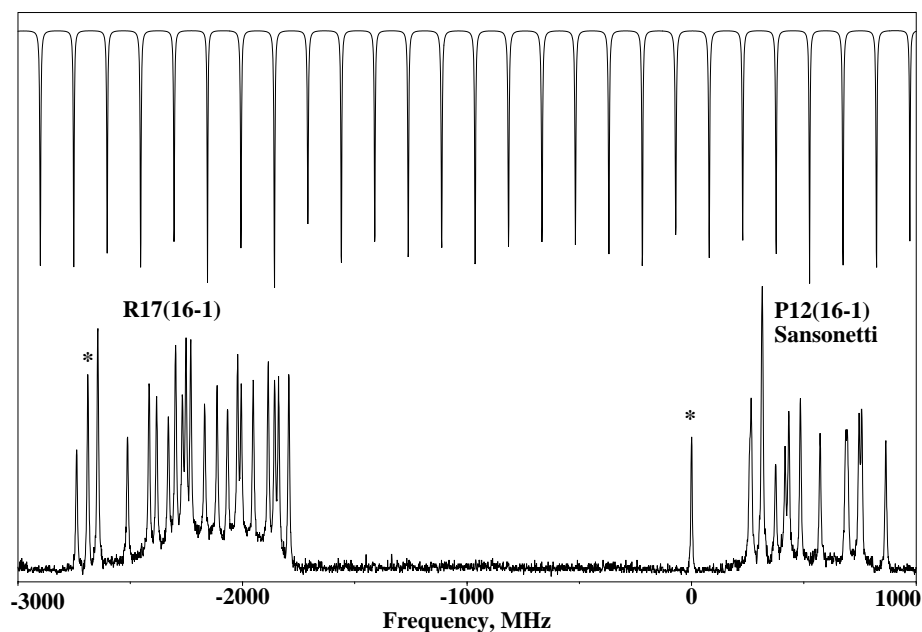


Figure 5.1: Scheme of the experimental setup.

(between two markers) of a fixed component of each  $I_2$ -line is determined by means of a computerized fitting and interpolation procedure. In this way well-calibrated hyperfine components (“reference” lines) and new lines were recorded. While the integer number of fringes separating these lines from reference lines is determined with the aid of the  $I_2$ -atlas the fractional values (to within 1% of FSR) give an improved calibration. Only when the separation exceeds several  $\text{cm}^{-1}$  the error in the FSR contributes to the final uncertainty. In two cases long overlapping scans of  $10 \text{ cm}^{-1}$  were performed with the goal of calibrating an  $I_2$ -component close to a frequency of special interest. First, the frequency of a component at  $1/10$  of the  $1^1S-2^1P$  resonance line of helium [6, 7] was recorded in overlapping scans starting at the R99 “i” (15-1) line accurately calibrated by Grieser *et al.* [18]. Secondly, the  $I_2$ -component R100 “t” (14-0) at  $1/6$  the frequency of the Q-branch of the L-X(0,0) band of CO [8] was recorded with respect to the P98 “t” (14-0) line provided by Sansonetti [20]. Data from these procedures are included in the present analysis.

An example is shown in Fig. 5.2 displaying a single scan over two rotational lines - R(17) of (16-1) band and one of the reference lines - P12(16-1), measured by Sansonetti [20] with accuracy of 1 MHz (the “t” components are denoted by \*). The scan axis is calibrated to the reference line using the FSR of the etalon. In this way the absolute frequency of R17 “t” (16-1) is determined with an accuracy of about 2 MHz.

Through frequency separation measurements hyperfine components of selected P( $J$ ) and R( $J$ ) lines in the (13-1) to (18-1) bands were recorded and calibrated (Table 5.1). The estimated absolute accuracy varies in the range 1-5 MHz. Except for the two wavelength ranges mentioned above always lines were recorded close to calibrated lines



**Figure 5.2:** Simultaneous scan over two lines (R17 and P12) in the  $B-X$  (16-1) band of  $I_2$  (lower trace) and the fringes of a stabilized etalon (upper trace). The “t” components are denoted by \*. Note that for the R(17) line all 21 transitions corresponding to  $\Delta F = \Delta J = +1$  are resolved.

presented in literature [11, 13, 18, 20]. In all cases the “t”-component was selected for calibration. For convenience and to avoid any confusion, two typical hyperfine spectral structures, for odd and even  $J$ , are displayed in Fig. 5.3, with the identification of hyperfine components (“a”-“u”) adopted from Sansonetti [20]. For low  $J$  ( $J < 20$ ) these typical shapes of the rotational lines undergo changes and more hyperfine components become resolved (see Fig. 5.2, where all 21 hyperfine components of R17(16-1) can be seen).

**Table 5.1:** Measured transition frequencies in this study.

Transition	“t” component, MHz	Transition	“t” component, MHz
P(9) 13-1	509601977.9(1.6)	P(65) 16-1	517185695.6(1.3)
R(9) 13-1	509632429.0(1.9)	R(69) 16-1	517217059.9(1.2)
R(13) 13-1	509609972.0(2.0)	P(93) 16-1	515659358.7(1.5)
P(15) 13-1	509545298.7(2.3)	R(116)16-1	514370607.9(1.1)
R(15) 13-1	509594978.1(1.6)	R(121)16-1	513979201.2(1.2)
P(18) 13-1	509508487.7(1.6)	P(124)16-1	513350047.8(1.1)

**Table 5.1:** Measured transition frequencies in this study. (*continued*)

Transition	“t” component, MHz	Transition	“t” component, MHz
P(20) 13-1	509480808.2(1.9)	P(132)16-1	512647155.5(1.0)
R(20) 13-1	509546506.3(2.5)	R(136)16-1	512701376.6(1.1)
R(23) 13-1	509509886.3(1.7)	R(137)16-1	512610634.7(1.3)
R(25) 13-1	509482330.8(1.9)	P(8) 17-1	521586497.4(4.4)
P(27) 13-1	509364143.8(2.7)	R(14) 17-1	521575692.3(4.5)
R(32) 13-1	509366084.1(2.5)	R(15) 17-1	521567120.5(4.5)
R(38) 13-1	509241911.8(2.5)	P(22) 17-1	521418244.1(2.2)
P(39) 13-1	509092511.4(2.4)	P(42) 17-1	520948096.8(1.1)
R(44) 13-1	509095072.1(2.6)	R(54) 17-1	520705108.8(1.7)
P(44) 13-1	508952596.1(3.0)	P(64) 17-1	520117714.3(3.9)
P(46) 13-1	508892223.1(3.0)	R(68) 17-1	520143711.2(3.9)
R(49) 13-1	508955369.9(2.7)	R(6) 18-1	524475481.8(4.3)
R(51) 13-1	508895076.1(2.9)	R(8) 18-1	524468252.9(4.2)
P(65) 13-1	508192805.3(1.6)	R(18) 18-1	524390857.2(4.0)
R(75) 13-1	507974147.3(2.0)	P(19) 18-1	524319179.5(3.9)
R(79) 13-1	507785131.1(2.2)	R(24) 18-1	524311394.2(3.0)
R(83) 13-1	507585929.2(1.8)	P(27) 18-1	524177555.9(3.4)
R(87) 13-1	507376523.8(1.4)	R(31) 18-1	524187351.0(2.5)
R(91) 13-1	507156900.2(1.8)	P(31) 18-1	524090221.6(3.3)
P(99) 13-1	506369955.4(1.2)	R(40) 18-1	523978221.5(2.0)
R(104)13-1	506372344.2(1.3)	P(42) 18-1	523793188.2(1.8)
R(107)13-1	506175873.2(1.6)	R(46) 18-1	523807726.7(1.8)
R(111)13-1	505904887.9(1.6)	P(47) 18-1	523630566.8(1.3)
P(111)13-1	505550262.0(1.8)	R(50) 18-1	523680231.5(1.5)
R(116)13-1	505551619.9(1.9)	R(54) 18-1	523541657.9(1.2)
P(119)13-1	504952280.2(3.3)	R(56) 18-1	523468212.5(1.3)
P(123)13-1	504637769.6(1.1)	R(60) 18-1	523312993.5(1.8)
R(128)13-1	504637640.5(1.2)	P(61) 18-1	523083220.3(1.1)
R(130)13-1	504476197.9(1.6)	R(63) 18-1	523189287.3(1.6)
P(67) 14-1	511156922.0(1.1)	R(64) 18-1	523146661.6(1.1)
P(68) 14-1	511111745.3(1.1)	R(71) 18-1	522828790.3(1.5)
P(69) 14-1	511065923.3(1.1)	R(76) 18-1	522580821.6(2.0)
P(70) 14-1	511019455.2(1.4)	P(81) 18-1	522065155.8(3.3)
R(72) 14-1	511154541.7(1.2)	R(82) 18-1	522260185.6(2.5)
R(73) 14-1	511109285.1(1.3)	P(86) 18-1	521767018.7(2.0)
R(74) 14-1	511063381.3(1.1)	R(88) 18-1	521914325.2(1.5)
P(92) 14-1	509833399.7(1.1)	P(98) 18-1	520979920.4(3.2)
P(15) 15-1	515641846.2(2.4)	R(98) 18-1	521281620.3(1.4)
P(16) 15-1	515629854.0(1.2)	R(100)18-1	521146613.6(1.2)
R(19) 15-1	515651560.1(1.4)	P(101)18-1	520767302.1(1.4)
R(20) 15-1	515640121.4(1.3)	R(104)18-1	520868103.6(1.3)

**Table 5.1:** Measured transition frequencies in this study. (*continued*)

Transition	“t” component, MHz	Transition	“t” component, MHz
R(21) 15-1	515628031.0(1.3)	P(104)18-1	520548328.3(2.2)
P(117)15-1	511044175.2(1.1)	P(105)18-1	520473922.7(2.2)
R(121)15-1	511103398.7(1.5)	R(110)18-1	520429053.2(1.3)
R(136)15-1	509850059.7(1.3)	R(113)18-1	520199924.4(1.5)
P(11) 16-1	518650204.9(1.3)	R(114)18-1	520122122.2(1.8)
R(17) 16-1	518637995.9(1.7)	R(116)18-1	519964376.7(1.7)
R(18) 16-1	518627631.3(1.5)	R(119)18-1	519722396.0(2.1)
P(21) 16-1	518525170.7(1.9)	P(123)18-1	519013099.8(3.6)
R(26) 16-1	518520828.6(1.3)	R(124)18-1	519304761.9(2.4)
P(30) 16-1	518355932.5(1.8)	R(132)18-1	518599137.6(1.4)
R(35) 16-1	518349878.8(1.8)		

### 5.3 Data analysis

In the analysis of their spectra Gerstenkorn and Luc [1] performed a fit to the rovibronic structure of the  $B$ - $X$  system of  $I_2$  with energy representations:

$$E_{X_{\nu''}} = E_{\nu''} + B_{\nu''}J(J+1) - D_{\nu''}J^2(J+1)^2 + H_{\nu''}J^3(J+1)^3, \quad (5.1 \text{ a})$$

$$E_{B_{\nu'}} = E_{\nu'} + B_{\nu'}J(J+1) - D_{\nu'}J^2(J+1)^2 + H_{\nu'}J^3(J+1)^3 + L_{\nu'}J^4(J+1)^4 + M_{\nu'}J^5(J+1)^5, \quad (5.1 \text{ b})$$

for ground and excited states respectively. The molecular parameters derived in [1] give an accurate description of transition frequencies up to  $J \sim 160$  within the stated uncertainty of 60 MHz. The representation of Eqs. (5.1 a,5.1 b) will be used in the present study to denote the “centre-of-gravity”, i.e. the energy level structure and transition frequencies with all hyperfine effects set to zero.

The hyperfine structure of  $I_2$  has been studied previously for a large number of individual rotational lines scattered in the visible wavelength range. For the purpose of our analysis only the two most important terms in the hyperfine Hamiltonian [23] are included:

$$H_{hf} = eQq \cdot H_{EQ} + C \cdot H_{SR}, \quad (5.2)$$

where  $eQq \cdot H_{EQ}$  is the electric quadrupole term and  $C \cdot H_{SR}$  is the spin-rotation term ( $eQq$  and  $C$  are the conventional symbols, representing the constants for the respective interactions). These terms are sufficient to represent the separations of  $F = J$  hyperfine components with respect to the “centre-of-gravity” at the 0.2 MHz accuracy level if  $\Delta J = \pm 2$  contributions are included in the diagonalization of the hyperfine matrix. Following the discussion of Bordé *et al.* [21] we adopt for the  $X^1\Sigma_g^+$ ,  $\nu' = 1$  ground state the hyperfine constants  $eQq'' = -2452.6$  MHz and  $C'' = 3$  kHz. For the excited

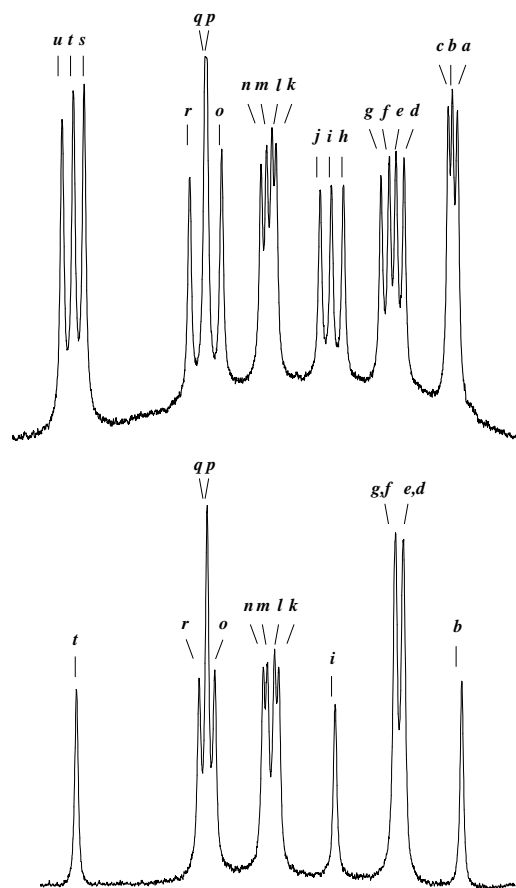


**Figure 5.3:** Typical pattern of hyperfine structures in  $I_2$ . The upper trace is a recording of the R69(16-1) line and shows the typical structure for an odd- $J$  line with  $21 \Delta F = \Delta J$  main transitions. The lower trace shows the R98(16-1) line with the typical  $15 \Delta F = \Delta J$  main transitions in an even- $J$  line. In the present study we have adopted the identification of “a”-“u” components of Sansonetti [20].

vibrational levels the hyperfine constants ( $eQq$  and  $C$ ) have been reported for  $\nu' = 15$  [24] and  $\nu' = 17$  [25] only. In this work we adopted the hyperfine constants  $eQq_{\nu'}$  and  $C_{\nu'}$  using the empirical formulae given by Razet and Picard [26], including the  $J$ -dependence in  $C'$ . The uncertainty in the  $eQq_{\nu'}$  is estimated at 0.3 MHz, which yields an uncertainty of less than 0.1 MHz in the position of the “t” component with respect to the “centre-of-gravity”. Since the spin-rotation contribution to the eigenvalues for  $F = J$  hyperfine components can be neglected at our level of accuracy, one of them - the “t” component

is preferably used in this study.

For all lines calibrated in the present study the “centre-of-gravity” of the rotational structure was determined by correcting the measured hyperfine components (Table 5.1) for the calculated hyperfine shift. All “t”-components are red-shifted by approximately 483 MHz, with slight variations over the six bands measured and over the rotational lines. The accurately calibrated lines cited in the literature [9, 11, 18, 20] were included in the analysis, but not presented on Table 5.1. For each line an estimated uncertainty is listed as well, which depends on the measurement error and the uncertainty of the reference line used. For the collection of lines taken from Sansonetti the resulting uncertainty is less than 1.0 MHz, including a contribution of the hyperfine shift correction. For a number of previously reported lines calibrated by our group [7, 8] (not listed here), the accuracy varies from 3.0-5.0 MHz. The lines specifically calibrated in the present work have an accuracy of 1.5-4.5 MHz depending on the measuring conditions.

For each band all available data on the “centre-of-gravity” transition frequencies (calculated from Table 5.1 and from Refs. [7, 8, 18, 20]) were included in a weighted least squares fit in order to obtain a parameterization over the rotational structure in  $B-X(\nu' - 1)$  bands ( $\nu' = 13 - 18$ ). It turned out to be sufficient to vary only the band origin  $E_0 = E_{\nu'} - E_1$ , the rotational constant  $B_1$  and the rotational constants  $B_{\nu'}$ ,  $D_{\nu'}$  and  $H_{\nu'}$  of the excited state to find convergence with a resulting  $\chi^2$  of less than 1.0 per data point. The higher order molecular constants for the ground state ( $\nu'' = 1$ ) were kept fixed at the values of Gerstenkorn and Luc [1]:  $D_1 = 4.5722085 \times 10^{-9} \text{ cm}^{-1}$  and  $H_1 = -5.3403223 \times 10^{-16} \text{ cm}^{-1}$ . The higher order centrifugal distortion coefficients for the excited state ( $L_{\nu'}$  and  $M_{\nu'}$ ) were also kept fixed at the values of Ref. [1]. Since the goal of the present study is to find a parameterization of the energy levels only rather than deriving new details on the molecular structure, no further attempts in this latter direction were made. The resulting parameters for the transitions with upper level  $\nu' = (13 - 18)$  (see Table 5.2) were inserted in Eqs. (5.1 a, 5.1 b) for calculation of the “centre-of-gravity” frequencies.

**Table 5.2:** The derived values for the constants appearing in Eqs. (5.1 a, 5.1 b), corresponding to  $\nu' - 1$  transitions. All the values are in wavenumbers.

$\nu'$	$E_{\nu'} - E_1$	$B_1 \times 10^2$	$B_{\nu'} \times 10^2$	$D_{\nu'} \times 10^8$	$-H_{\nu'} \times 10^{14}$	$-L_{\nu'} \times 10^{19}$	$-M_{\nu'} \times 10^{25}$
13	16999.931315	3.71968789	2.67324769	0.83217395	0.66855643	0.142729375	0.82943669
14	17102.554990	3.71970147	2.65407989	0.85592155	0.70580093	0.161026496	0.97512745
15	17203.371621	3.71969569	2.63449183	0.87997748	0.80130524	0.181804330	1.14494794
16	17302.358760	3.71969318	2.61450317	0.90621126	0.87175280	0.205409358	1.34313350
17	17399.494325	3.71964275	2.59404320	0.93415830	0.94165694	0.232226556	1.57482286
18	17494.756134	3.71967270	2.57323368	0.96427269	1.00923370	0.262682841	1.84624651

The consistency of the fits is such that for all bands the resulting  $\chi^2$  is much lower than the number of data points. In all cases 5 parameters (described above) were optimized in the fitting routines. From the resulting  $\chi^2$  values we estimate that the final

uncertainties of all “centre-of-gravity” rotational frequencies are accurate within 2 MHz. This can be seen from Fig. 5.4, where the offsets of the calibrated lines in (18-1) band from the fit are presented. Most of the measured values lay in the interval (-2,+2) MHz and the fit passes through all error margins. Consequently, the fit for the “centre-of-gravity” frequencies can be used to predict the positions of the “t” hyperfine components for all lines with 2 MHz accuracy. This procedure will be discussed in section 5.4.

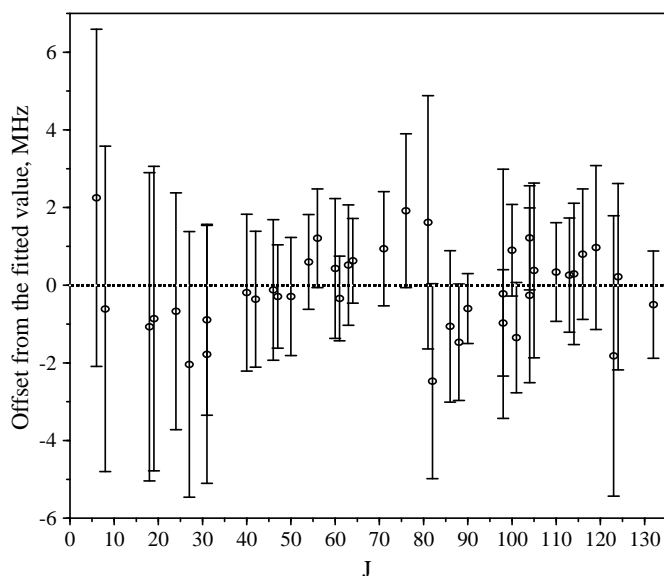


**Figure 5.4:** The offset of the “centre-of-gravity” frequencies, measured in the (18-1) band (the data points) from the fitted values (dashed line).

An important assumption for the validity of the present procedure is the unperturbed nature of the  $B$ - $X$  system of  $I_2$ . The excited  $B$ -state is known to be perturbed by a repulsive state of  $^1\Pi_u$  symmetry, causing pre-dissociation in the  $B$ -state [27]. This holds for the region  $\nu' = (13 - 18)$  in the  $B$ -state. At much higher  $\nu$ -states also other states interact and even  $u$ - $g$  symmetry breaking has been observed [21,27]. The coupling with the state may in principle cause energy shifts to the  $B$ -state energy levels. However, the coupling to the repulsive state gives only rise to global effects, slowly varying over the  $J$ -quantum number, while no local effects such as accidental shifts are expected. Indeed such phenomena were not observed, while care was taken that  $P(J)$  and  $R(J)$  transitions were included in the fit in a wide range of  $J$ -values with gaps as small as possible. Possible perturbative effects by the  $^1\Pi_u$  state are therefore included in the present parameterization of the  $B$ -state energy levels by the effective molecular parameters as derived in the fits (Table 5.2).

## 5.4 The reference standard

The molecular parameters derived from the present measurements and fitting procedures give a representation of “centre-of-gravity” transition frequencies of  $R(J)$  and  $P(J)$  lines in the (13-1) to (18-1) bands for  $J$  up to 140 at an accuracy level of 2 MHz (Table 5.2). By invoking the theoretically known hyperfine structure, the frequency of the “t”-component of each line can be calculated at the same accuracy level. A list of these calculated transition frequencies of “t”-components is given in the Appendices 5.I and 5.II, corresponding to R and P branches respectively\*. The tables start at  $J = 9$  because of the strong mutual overlapping of the rotational lines with lower  $J$ , which makes them unsuited for spectroscopic calibration. These frequencies form a secondary reference standard in the range 571-596 nm. It is a factor of 30 more accurate than the Doppler-broadened  $I_2$ -reference standard [1]. Since a calibrated component is found in nearly all intervals of  $1 \text{ cm}^{-1}$  this dense grid of reference lines should become a useful tool in laser spectroscopic studies.

## 5.5 Conclusions

In this Chapter we have shown that a simple parameterization (involving 5 molecular parameters) of the positions of the “t” hyperfine components in the rotational structure of  $^{127}I_2$  is possible giving an accuracy of 2 MHz, suitable for precise spectroscopic measurements. Using this procedure we present a table, containing 1584 accurate wavenumbers (see Appendices 5.I and 5.II)\*, which predicts the line-positions of the “t” components in the  $B-X$  system of  $^{127}I_2$  for vibrational bands (13-1) up to (18-1) and rotational quantum numbers  $J$  from 9 up to 140 (both for  $R$  and  $P$  branches). This dense grid of high precision data covers the wavelength range 571-596 nm, corresponding to a frequency span of  $715 \text{ cm}^{-1}$ . In a wavelength range near 790 nm a similar reference standard based on  $I_2$  hyperfine components is being developed by Knöckel *et al.* [28].

### Acknowledgments

The authors would like to thank Dr. C. Sansonetti (NIST) for providing us with his results on absolute calibrations prior to publication and for stimulating discussions. They acknowledge Dr. K. A. H. van Leeuwen (Eindhoven) for the construction of the stabilized HeNe-laser during his Ph.D. thesis work in our laboratory. Dr. S. Picard (BIPM) has been very helpful by sending us publications on hyperfine structure calculations. The Netherlands Foundation for Fundamental Research on Matter (FOM) is acknowledged for financial support.

---

\*These tables constitute a supplementary material to the article J. Mol. Spectrosc. **187**, 21 (1998) and are available on-line on the Journal of Molecular Spectroscopy homepage (<http://www.apnet.com/www/journal/ms.htm> or <http://www.europe.apnet.com/www/journal/ms.htm>). In view of their length we do not present them in this Thesis.

## References

- [1] S. Gerstenkorn and P. Luc, "Atlas du spectre d'absorption de la molecul e de l'iode entre 14,800-20,000  $\text{cm}^{-1}$ ", Ed. CNRS, Paris; we use the 1985 version with the "Complément" containing line identifications and details on the rotational analysis
- [2] S. Gerstenkorn and P. Luc, "Atlas du spectre d'absorption de la molecul e de l'iode entre 14,000-15,600  $\text{cm}^{-1}$ ", Ed. CNRS, Paris, 1978
- [3] S. Gerstenkorn, J. Verges, J. Chevillard, "Atlas du spectre d'absorption de la molecul e de l'iode entre 11,000-14,000  $\text{cm}^{-1}$ ", Ed. CNRS, Paris, 1982
- [4] S. Gerstenkorn, P. Luc, *Rev. Phys. Appl.* **14**, 791 (1979).
- [5] J.M. Gilligan, E.E. Eyler, *Phys. Rev. A* **46**, 3676 (1992).
- [6] K. S. E. Eikema, W. Ubachs, W. Vassen, W. Hogervorst, *Phys. Rev. Lett.* **76**, 1216 (1996).
- [7] K. S. E. Eikema, W. Ubachs, W. Vassen, W. Hogervorst, *Phys. Rev. A* **55**, 1866 (1997).
- [8] W. Ubachs, K. S. E. Eikema, W. Hogervorst, P. C. Cacciani, *J. Opt. Soc. Am. B* **14**, 2469 (1997).
- [9] T. J. Quinn, *Mertologia* **30**, 523 (1993).
- [10] J. E. M. Goldsmith, E. W. Weber, F. V. Kowalski, A. L. Schawlow, *Appl. Opt.* **18**, 1983 (1979).
- [11] P. Juncar, J. Pinard, J. Hamon, A. Chartier, *Mertologia* **17**, 77 (1981).
- [12] D. A. Jennings, C. R. Pollock, F. R. Petersen, R. E. Drullinger, K. M. Evenson, J. S. Wells, J. L. Hall, H. P. Layer, *Opt. Lett.* **8**, 136 (1983); C. R. Pollock, D. A. Jennings, F.R. Petersen, J. S. Wells, R. E. Drullinger, E. C. Beaty and K. M. Evenson, *Opt. Lett.* **8**, 133 (1983).
- [13] L. Hlousek, W. H. Fairbank, *Opt. Lett.* **8**, 322 (1983).
- [14] P. Juncar, H. G. Berry, R. Damaschini, H. T. Duong, *J. Phys. B* **16**, 381 (1983).
- [15] D. Shiner, J. M. Gilligan, B. M. Cook, W. Lichten, *Phys. Rev. A* **47**, 4042 (1993).
- [16] O. Acef, J. J. Zondy, M. Abed, D. J. Rovera, A. H. Gerard, A. Clairon, Ph. Laurent, Y. Millerioux, P. Juncar, *Opt. Commun.* **97**, 29 (1993).
- [17] U. Brand, *Opt. Commun.* **100**, 361 (1993).
- [18] R. Grieser, G. Bönsch, S. Dickopf, G. Huber, R. Klein, P. Merz, A. Nicolaus, H. Schnatz, *Z. Phys. A* **348**, 147 (1994).
- [19] C. S. Edwards, G. P. Barwood, P. Gill, F. Rodríguez-Llorente, W. R. C. Rowley, *Opt. Commun.* **132**, 94 (1996).
- [20] C. J. Sansonetti, *J. Opt. Soc. Am. B* **14**, 1913 (1997).
- [21] Ch. J. Bordé, G. Camy, B. Decomps, J.P. Descoubes, J. Vigué, *J. Physique* **42**, 1393 (1981).
- [22] W. G. Schweitzer, E. G. Kessler, R. D. Deslattes, H. P. Layer, J. R. Whetstone, *Appl. Opt.* **12**, 2927 (1973).
- [23] G. R. Hanes, J. Lapierre, P. R. Bunker, K. C. Shotton, *J. Mol. Spectrosc.* **39**, 506 (1971).
- [24] A. Razet, Y. Millerioux, P. Juncar, *Mertologia* **28**, 309 (1991).
- [25] A. Razet, *Mertologia* **30**, 193 (1993).
- [26] A. Razet, S. Picard, *Mertologia* **34**, 181 (1997).
- [27] J. Vigué, M. Broyer, J. C. Lehmann, *J. Physique* **42**, 937, 949, 961 (1981).
- [28] H. Knöckel, S. Kremser, B. Bodermann, E. Tiemann, *Z. Phys. D* **37**, 43 (1996).



# Chapter 6

## Precision frequency calibration in XUV.

### 6.1 Precision spectroscopy of argon at 105 nm\*

The results of a precision measurement of the  $3p^6 - 3p^54s'[1/2]_1$  ( $1s_2$  in Paschen notation) transition in argon by resonance enhanced 1VUV + 1UV photo-ionization spectroscopy at 105 nm are presented. Tunable narrow-band VUV radiation is generated by frequency up-conversion of the powerful output of a pulsed dye amplifier system. A transition frequency of  $95399.833(3) \text{ cm}^{-1}$  in  $^{40}\text{Ar}$  is measured, in agreement with but an order of magnitude more accurate than the existing value for this transition. Transition isotope shifts  $\delta\nu_{40-38} = 550(10) \text{ MHz}$  and  $\delta\nu_{40-36} = 1036(7) \text{ MHz}$  are obtained, from which specific mass shifts are deduced. An improved value for the ionization potential in argon (IP= $127109.842(4) \text{ cm}^{-1}$ ) is also given.

#### 6.1.1 Introduction

In the past decade, with the development of powerful dye amplifiers and harmonic-generation techniques, the vacuum ultraviolet (VUV) spectral region became accessible with narrow-band tunable laser sources, thus making possible spectroscopic studies of transitions involving ground states of noble gas atoms with unsurpassed accuracy. The energy level structure of the noble gases is such, that the entire manifold of electronically excited states is separated from the electronic ground state by a large energy gap. A laser at 58 nm was used [1] to bridge this gap in helium resulting in accurate values for the ionization potential (IP), the ground state Lamb shift and the  $^3\text{He}$ - $^4\text{He}$  isotope shift. Similar studies of heavier rare gases such as Ne and Kr in the VUV [2,3] gave valuable information on the level structure of these more complex systems and at present an accuracy of  $0.005 \text{ cm}^{-1}$  is reached for some VUV transitions. However, in Ar accurate values for the VUV transition frequencies are missing; hence the ionization potential is not accurately known for this atom. Recently [4] a multichannel quantum defect analysis of the Rydberg series of  $^{40}\text{Ar}$  was reported, determining accurate values ( $\pm 0.003 \text{ cm}^{-1}$ ) for the two ionization potentials ( $j_c = 1/2, 3/2$ ) with respect to the metastable  $^3P_2$  level ( $1s_5$  in Paschen notation), populated in a discharge.

In this Section we report on a precision calibration of the  $3p^6(^1S_0) - 3p^54s'[1/2]_1(1s_2)$  transition in argon by 1VUV+1UV photo-ionization using a narrow-band laser source at 105 nm. The accuracy of  $0.003 \text{ cm}^{-1}$  is a factor 15 better than the best known value of  $0.05 \text{ cm}^{-1}$  [5] dating from the early 70's. Furthermore an analysis of the isotope shifts in the  $^1S_0 - 1s_2$  transition for the three stable argon isotopes (36, 38, 40) is made. In general, these shifts are due to differences in the nuclear mass (mass shifts) and nuclear charge distribution (field shifts). To a good approximation [6] the isotope shift can be

---

\*Journal of Physics B: Atomic, Molecular and Optical Physics **32** (17), L511-L516 (1999).

presented as a sum of the mass and field shift. The latter is negligible for light elements such as argon, but it can dominate the isotope shift in heavy elements. The mass shift can be described as consisting of two parts: normal mass shift (NMS), also called Bohr shift, due to the change of the reduced mass  $\mu$ , and specific mass shift (SMS), resulting from the correlation between the momenta of all electrons in the atom. While the NMS is easy to calculate, difficult many-body calculations are needed in order to estimate the SMS [7]. In the following we give experimental values for the SMS in  $^1S_0 - 1s_2$  transition for the three stable argon isotopes.

### 6.1.2 Experimental setup

In Fig. 6.1 a scheme of the experimental setup is presented. Tunable visible wavelengths at 630 nm are generated with an Ar-ion laser pumped continuous wave (CW) ring-dye-laser operating on DCM dye and delivering 400 mW of single mode narrow-band radiation. A sealed and temperature stabilized etalon, which is actively locked to a frequency-stabilized He-Ne laser, provides accurate frequency markers. Its free spectral range of 148.9565(4) MHz was calibrated by measuring the frequency separation between two accurately known hyperfine components of P61(7-3) and R96(9-4) lines in molecular iodine [8]. Absolute calibration in the visible is based on the “t” hyperfine component of R67(9-4) in the saturation spectrum of iodine measured for the purpose of this experiment [9].

The output of the dye laser is coupled into a polarization maintaining single-mode fiber (3M, FS-PM-3-21) for beam transportation to the pulsed part of the experiment as well as for spatial filtering. The fiber output (200 mW) is seeding a three-stage pulsed dye amplifier (PDA) operating on DCM dye as well, which is pumped by a frequency-doubled (532 nm), injection-seeded Nd:YAG (Quanta Ray, GCR 5) laser at 10 Hz repetition rate. Wavelength-tunable pulses of 5 ns duration and 80 mJ/pulse energy, generated in the PDA, are frequency doubled in a KD\*P crystal. The UV (315 nm) is separated from the visible and focused (inside a vacuum chamber) in an expanding pulsed gas jet of Xe for frequency tripling down to 105 nm. The overlapping VUV and UV beams are intersected at 90° by an atomic beam of natural argon (99.6%  $^{40}\text{Ar}$ ; 0.063%  $^{38}\text{Ar}$ ; 0.337%  $^{36}\text{Ar}$ ). The ions created by 1VUV + 1UV photo-ionization are collected and mass-separated by a time-of-flight (TOF) mass-spectrometer. Three boxcar integrators are used to detect simultaneously each one of the three isotopes. With only 10 mJ/pulse UV energy the VUV production is sufficient to detect even the least abundant  $^{38}\text{Ar}$  isotope from a natural sample. During a single scan of the CW dye laser frequency, the spectra from the three isotopes are recorded along with the  $\text{I}_2$  saturation spectrum and the etalon markers.

### 6.1.3 Results and discussion

A single scan over 50 GHz in the VUV is shown in Fig. 6.2. The first three spectra represent the  $3p^6 - 3p^5 4s'[1/2]_1$  transition in  $^{40}\text{Ar}$ ,  $^{38}\text{Ar}$ , and  $^{36}\text{Ar}$ , respectively. The line-width of the Ar resonance width is  $\sim 450$  MHz, predominantly governed by the band-

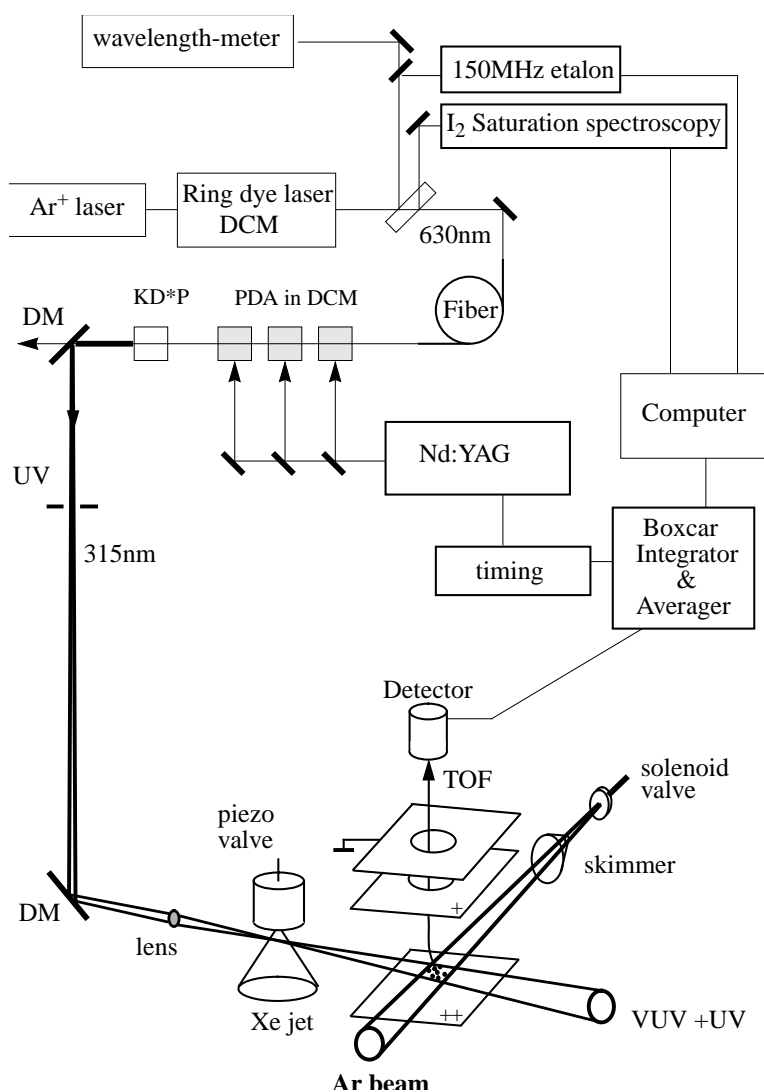


**Figure 6.1:** Scheme of the experimental setup.

width of the VUV-source and some contribution from the residual Doppler broadening in the crossed-beam configuration. The etalon trace gives the relative frequency scale of  $893.739(3)$  MHz per marker spacing. The scan is extended towards the nearest iodine line R67(9-4). Its “t” component (denoted in Fig. 6.2 by an asterisk) is calibrated in the visible with respect to the “t” hyperfine component of P61(7-3) known with  $0.00002 \text{ cm}^{-1}$

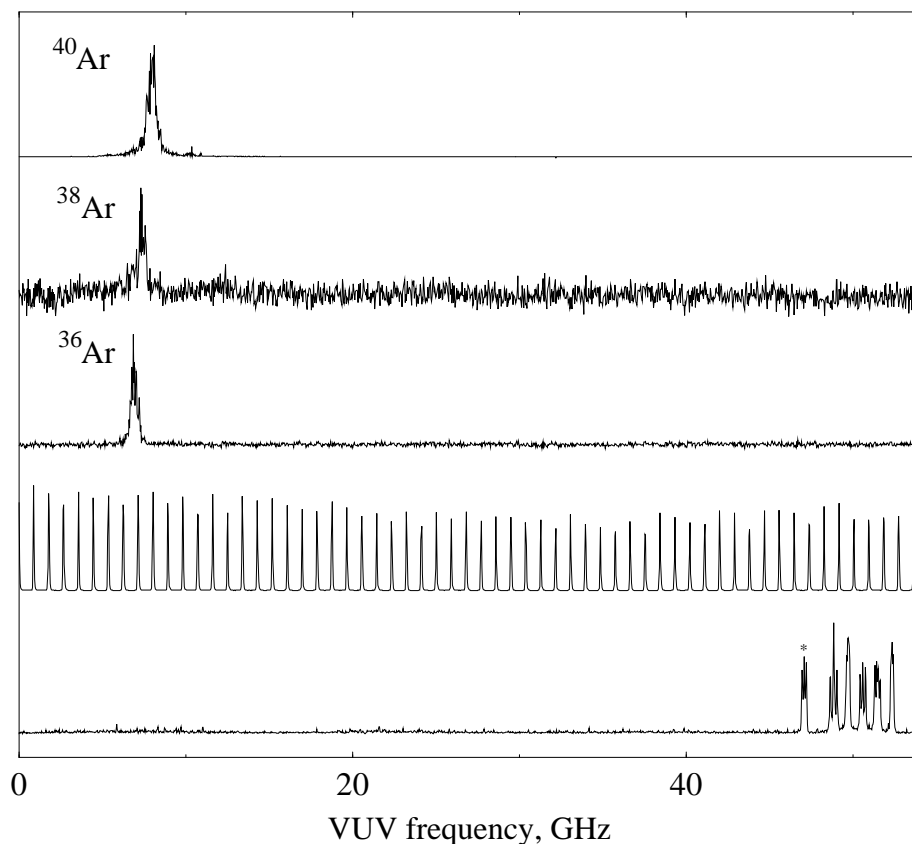


**Figure 6.2:** A scan of the  $^1S_0 - 1s_2$  resonance for the three isotopes, the etalon markers and the iodine saturation spectrum of  $R67(9-4)$ . Asterisk (\*) points at the “t” hyperfine component calibrated previously and used as frequency standard at 105 nm.

accuracy [8]. Our measurement yields  $15900.19013(7) \text{ cm}^{-1}$  for the “t” component of  $R67(9-4)$ , thus setting an accurate frequency standard of  $95401.14078(42) \text{ cm}^{-1}$  in the VUV near 105 nm. The transition frequencies of the three argon isotopes observed are then determined via a procedure, involving computerized fitting of the line profiles and interpolation on the frequency scale provided by the etalon markers.

Although the absolute calibration using  $\text{I}_2$  saturation spectroscopy in the CW part of the experiment and the relation  $\nu_{\text{VUV}} = 6\nu_{\text{vis}}$  gives very good accuracy, there are several systematic error sources to be taken into account. As the geometry of the experiment allows for a slight deviation from  $90^\circ$  beam crossing, a Doppler shift may be present and must be evaluated. Increasing the velocity of the atoms by seeding Ar (10%) in He beam

at constant geometry allows us to determine the Doppler shift under the experimental conditions to be  $+20(7)$  MHz. No indication of AC Stark shift is observed for UV powers of 10 mJ/pulse (*see* also Ref. [1]). However, the chirp induced in the PDA has to be estimated since its contribution can be significant after the frequency up-conversion [1]. We rely on existing measurements of chirp in dye amplifiers operating on DCM [10], which set an upper limit of about 100 MHz in this wavelength region. In Table 6.1 we summarize all contributions to the error in the measurement of the  $^1S_0 - 1s_2$  transition of  $^{40}\text{Ar}$ . It can be seen that the chirp generated during the amplification process is the dominating error source. A detailed quantitative evaluation of the chirp effect, as previously done for the case of helium [1], would potentially reduce the uncertainty in the measurement by a factor of three.

**Table 6.1:** Error budget for the  $^1S_0 - 1s_2$  transition frequency in  $^{40}\text{Ar}$ .

Source	Error [MHz]
Statistical $1\sigma$	20
I <sub>2</sub> calibration	12
Doppler shift	7
Chirp	$\leq 100$
Total error rms	103

Taking into account the above mentioned remarks, the transition frequencies for the three isotopes are determined as follows:  $\nu_{40} = 95399.833(3)$   $\text{cm}^{-1}$ ;  $\nu_{38} = 95399.815(3)$   $\text{cm}^{-1}$ ;  $\nu_{36} = 95399.798(3)$   $\text{cm}^{-1}$ . To our knowledge these are the most accurate values for any transition involving the ground state of Ar so far. The best measurement for  $1s_2$  line is the classical spectroscopic value reported by Minnhagen [5] with 15 times lower accuracy.

The presently measured transition frequency can be used to determine an improved value for the first ionization potential  $I_{3/2}$  of Argon I. In a recent study of the  $J=4$  Rydberg series the group of Hotop [4] reported on a value  $I_{3/2}=21647.076(2)$   $\text{cm}^{-1}$  with respect to the  $3p^5 4p[5/2]_3$  level ( $2p_9$  in Paschen notation). The difference between this even parity  $2p_9$  level and the odd parity  $1s_2$  level (the upper level in the present experiment), follows from the work of Minnhagen [5]. We take the average of the value of Minnhagen [5] and Norlén [11] for  $2p_9$ , differing by only  $0.0011$   $\text{cm}^{-1}$ . Hence we deduce  $10062.9325(10)$   $\text{cm}^{-1}$  for the separation  $2p_9 - 1s_2$ . Combining this value with the  $^1S_0 - 1s_2$  transition frequency and the  $I_{3/2}(2p_9)$  from [4] we deduce a value for the first ionization potential  $I_{3/2}=127109.842(4)$   $\text{cm}^{-1}$ . For the spin-orbit excited ionization limit  $I_{1/2}$  we use the fine structure splitting of  $1431.5831(7)$   $\text{cm}^{-1}$  for  $\text{Ar}^+(^2P_{3/2} - ^2P_{1/2})$  measured by IR spectroscopy [12], resulting in  $I_{1/2}=128541.425(4)$   $\text{cm}^{-1}$ .

In Fig. 6.3 a simultaneous scan over the  $1s_2$  resonance in the three argon isotopes is presented along with the etalon markers spanning 8 GHz in the VUV. While in the

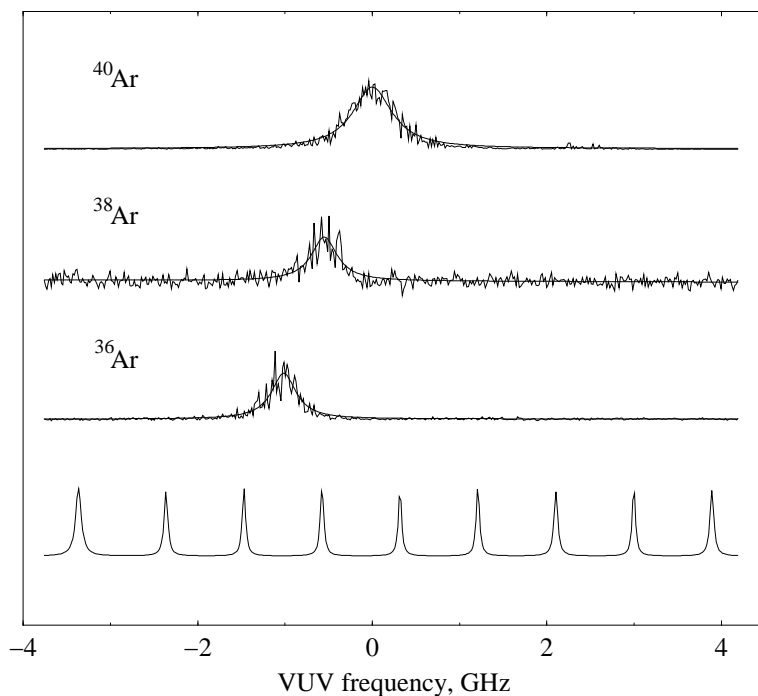


**Figure 6.3:** A scan over the  $^1S_0 - 1s_2$  resonance for the three isotopes.

measurement of the absolute transition frequencies the uncertainty is largely determined by systematic effects, this is not the case in a relative measurement yielding values for the isotope shifts. Hence, the uncertainty is only determined by statistical errors in the fitting procedure. The resulting isotope shifts with respect to the most abundant  $^{40}\text{Ar}$  are listed in the second column of Table 6.2.

According to [6] the NMS of an atomic level can be calculated by the formula:

$$\Delta E_{H,L} = m_e \frac{(M_H - M_L)}{M_H(M_L + m_e)} E_H, \quad (6.1)$$

where  $M_H$  and  $M_L$  are the masses of the heavy and light isotopes, respectively;  $m_e$  is the mass of the electron and  $E_H$  is the level energy of the heavier isotope (in our case  $^{40}\text{Ar}$ ). For the transition of interest the shift in the transition frequency due to the NMS is:

$$NMS(40, A) = \Delta E_{40,A}^g - \Delta E_{40,A}^e \quad (6.2)$$

where  $g$  and  $e$  denote ground and excited state respectively. The masses of the isotopes we take from [13]; the calculated values, according to Eq. (6.2) for the NMS are included

**Table 6.2:** Isotope shift analysis with respect to  $^{40}\text{Ar}$ .

A	$\delta\nu_{40-A}$ MHz	NMS(40,A) MHz	SMS= $\delta\nu_{40-A}$ -NMS(40,A) MHz
38	550(10)	2068	-1518(10)
36	1036(7)	4360	-3324(7)

in the third column of Table 6.2. In combination with the experimentally measured isotope shifts, values for the SMS in  $3p^6 - 3p^5 4s'[1/2]_1$  transition are deduced and reported in the fourth column of Table 6.2 with an accuracy that allows for future comparison with theoretical many-body calculations. As in case of Ne [2], our measurement shows that the SMS tends to compensate for the normal mass shift in the  $np^6 - np^5(n+1)s'[1/2]_1$  transition.

#### 6.1.4 Conclusion

In conclusion, precision spectroscopic measurement of the  $^1S_0 - 1s_2$  transition in argon at 105 nm is reported along with accurate isotope shift measurements for the three stable isotopes ( $^{36}\text{Ar}$ ,  $^{38}\text{Ar}$ ,  $^{40}\text{Ar}$ ). The data provided is valuable in connecting all accurately known levels in the argon atom with the ground state and in this way an order of magnitude improvement in the ionization potentials is achieved. From the isotope shift measurements, accurate values for the SMS are deduced for this VUV transition.

#### Acknowledgments

The authors wish to thank H. Hotop (University of Kaiserslautern) for stimulating discussions. This work was carried out with a research grant from the Netherlands Foundation for Research of Matter (FOM).

## 6.2 Precision VUV spectroscopy of xenon\*

The results from a high-resolution VUV spectroscopic study of Xenon in four transitions from the  $5p^6$  ( $^1S_0$ ) ground state to the  $5d'[3/2]_1$ ,  $8d[1/2]_1$ ,  $8d[3/2]_1$  and  $7s'[1/2]_1$  excited states is presented. Employing a narrowband VUV laser source based on successive second and third harmonic generation, the spectra of all nine stable isotopes are resolved making possible hyperfine splitting and isotope shift measurements. Using existing data for the change of the mean-square nuclear charge radii, mass shift and field shift contributions to the isotope shifts are separated. Precision transition frequency calibration yields an accurate value for the ionization energy of  $^{136}\text{Xe}$  ( $E_{3/2}^{136} = 97833.805(11) \text{ cm}^{-1}$ ).

\*an excerpt from a paper submitted for publication.

### 6.2.1 Introduction

VUV/XUV laser sources, based on harmonic generation of powerful UV laser pulses and utilizing the technique of 1VUV+1UV photoionization, have already been applied to spectroscopic studies of the noble gases He, Ne, Ar, and Kr [1–3,14], in which isotope shifts (IS) and hyperfine splittings (HFS) have been measured. In both He and Ar new accurate values of the ionization energy have been deduced from these measurements. For the heaviest stable noble gas, Xenon, accurate values for the VUV transitions from the ground state are missing, hence the ionization energy is less accurately known.

The investigation of the IS of a heavy element provides an insight into the electronic density at the nucleus as well. Previous IS measurements in a two-photon transition from the xenon ground state [15] have indicated a large screening effect by the  $p$ -electrons in the closed shell.

In this Section we present the results from a high-resolution 1VUV+1UV photoionization spectroscopy in Xe. We investigate the transitions from the ground state  $5p^6$  to four excited states:  $5d'[3/2]_1$ ,  $8d[1/2]_1$ ,  $8d[3/2]_1$  and  $7s'[1/2]_1$  at 106.8, 106.1, 105.6 and 104.4 nm, respectively. A natural Xenon sample consists of nine stable isotopes with abundances:  $^{124}\text{Xe}$  (0.0096%),  $^{126}\text{Xe}$  (0.009%),  $^{128}\text{Xe}$  (1.92%),  $^{129}\text{Xe}$  (26.4%),  $^{130}\text{Xe}$  (4.1%),  $^{131}\text{Xe}$  (21.1%),  $^{132}\text{Xe}$  (26.9%),  $^{134}\text{Xe}$  (10.4%) and  $^{136}\text{Xe}$  (8.9%). Our setup allows to spectrally resolve all isotopes and to measure the isotope shift in the investigated transitions.

Absolute transition frequencies are measured using a calibration procedure based on saturation spectroscopy of molecular iodine (*see* Chapter 5) and the use of actively stabilized Fabry-Perot interferometer. Our work connects, by means of accurate frequency measurements, the energy of the ground state to the entire manifold of electronically excited states; the transitions between those excited states and their position with respect to the ionization limit are known with high accuracy from precision laser spectroscopy in the visible and infrared.

### 6.2.2 Experimental

The experimental scheme for generation of wavelength-tunable VUV pulses has been explained in detail in Section 6.1.2 and Refs. [1,2,14]; here only a brief description is given. CW light from a tunable ring-dye-laser (Spectra-Physics, 380D), operating on DCM dye and pumped with the second harmonic of a CW Nd:YAG laser (Spectra-Physics, Millennia V), is amplified in a three-stage pulse-dye-amplifier (PDA). The PDA, which also operates on the DCM dye and is pumped by the second harmonic of an injection-seeded Q-switched Nd:YAG laser, delivers pulses with a repetition rate of 10 Hz, 5 ns pulse duration, and energy up to 60 mJ/pulse. These pulses are then frequency doubled in a KD\*P crystal, producing 8 mJ pulses in the UV, and subsequently focused in a Xenon gas jet for third harmonic generation. The overlapping UV and VUV light beams intersect at  $90^\circ$  a collimated Xenon atomic beam in the interaction region, where a 1VUV+1UV photoionization process takes place. A time-of-flight mass spectrometer collects the ions to be detected on an electron multiplier. The signals from the isotopes are recorded

with a number of boxcar integrators with gates, set at appropriate time windows. The signal-to-noise ratio is sufficiently high and allows to record the less abundant  $^{124}\text{Xe}$  and  $^{126}\text{Xe}$  isotopes as well; the only exception is the weak transition to the  $8d[1/2]_1$  excited state.

The absolute frequency of the CW light is calibrated by simultaneous recording of a saturated absorption spectrum of molecular iodine. The “t” hyperfine components of the  $\text{I}_2$  lines, recently calibrated with 1 MHz accuracy ( $1\sigma$ ) in the 595-655nm wavelength range [16], are used as a reference. Calibration of the VUV light is accomplished by taking into account the factor of 6 due to the frequency doubling and tripling. The center frequency of the pulsed output of the PDA may undergo, because of chirp, a small net shift with respect to the seeding CW light, used for calibration. This issue, including its effect in the harmonic frequencies, has been extensively discussed elsewhere [1, 10]. From such studies it is estimated that the uncertainty in the absolute VUV frequency is less than  $0.003\text{ cm}^{-1}$ . The chirp phenomenon, assuming weak wavelength dependence, does not affect the results of the relative frequency measurements, such as isotope shifts.

In addition, the transmission peaks of Fabry-Perot interferometer (FPI) are also recorded, in order to obtain accurate frequency markers for the CW light. The FPI is locked to a frequency-stabilized He-Ne laser, and its free spectral range of  $148.9563(3)\text{MHz}$  is calibrated against the known “t” hyperfine component of two  $\text{I}_2$  lines (P65(7-4) and P95(7-4) [16]). The FPI fringes are then translated into VUV frequency markers with a spacing of  $893.7378(18)\text{MHz}$ . Spectra of the Xenon resonances, the  $\text{I}_2$  reference spectrum and the FPI markers are recorded simultaneously and stored in a computer for further analysis. The width of the Xe lines is typically  $400\text{MHz}$  (FWHM) in a Gaussian profile, mainly due to the bandwidth of the VUV light along with a small Doppler contribution in the crossed-beam configuration.

### 6.2.3 Data analysis and discussion

The four transitions investigated are indicated by their excited state configurations, namely  $5d'[3/2]_1$ ,  $8d[1/2]_1$ ,  $8d[3/2]_1$  and  $7s'[1/2]_1$ . Isotopically and hyperfine resolved spectra of these states in excitation from the ground state are recorded. An example of the experimental results is given in Fig. 6.4, where the spectra recorded for all nine isotopes in the  $7s'[1/2]_1$  transition are shown. The different noise levels in the spectra reflect the relative natural abundance of the isotopes. Since only four boxcars are used, not all the isotopic lines have been measured simultaneously; hence one isotopic signal is chosen as a reference and recorded in each scan to facilitate the data analysis. Fig. 6.4 contains the results of three different scans, which are put together on the same frequency scale making use of the signal from the reference isotope. The FPI markers are also shown and the frequency scale is given in VUV frequency. It has to be noted that the weak peak present in the  $^{130}\text{Xe}$  spectrum is an artefact, associated with the resonance of the highly abundant lighter  $^{129}\text{Xe}$  isotope, which arrives earlier at the detector. To perform the absolute frequency calibration a long scan is usually needed to bridge the gap between the Xe line and the nearest  $\text{I}_2$  line (recorded in the visible). In the case of the  $7s'[1/2]_1$  the gap toward the R95(10-4) line is  $\sim 20\text{ GHz}$ , as seen in Fig. 6.4. In the

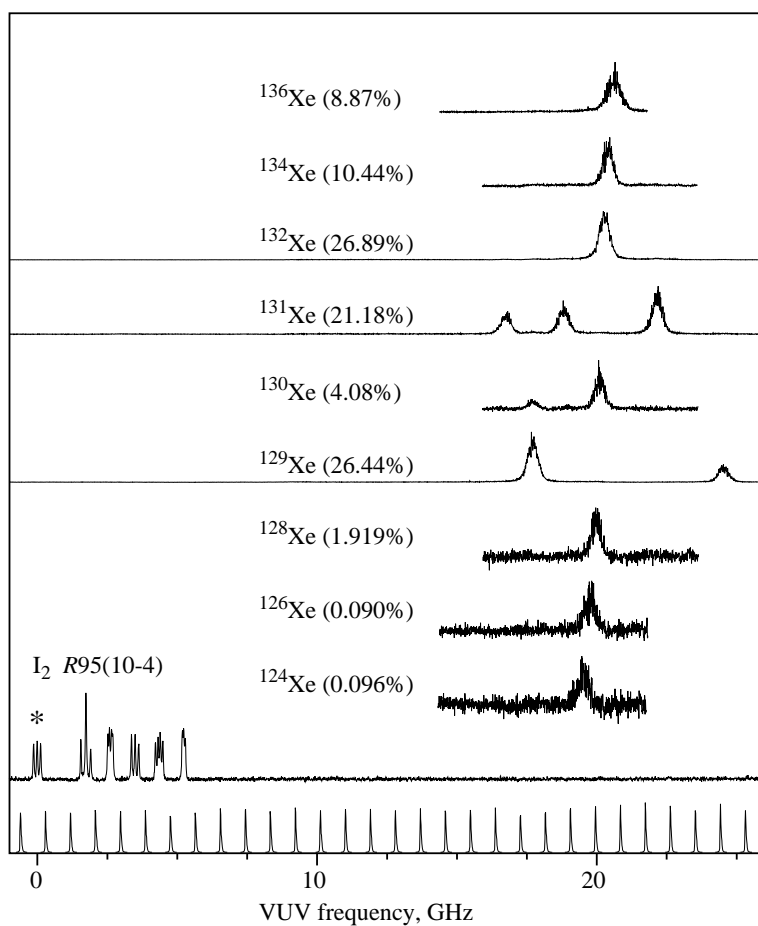


**Figure 6.4:** Spectra of the  $(5p^6 - 7s'[1/2]_1)$  transition, for all natural isotopes of Xenon. FPI transmission peaks, from which the frequency scale is deduced are also shown. The zero frequency is the “t” hyperfine component of  $R95(10-4)$   $I_2$  line (\*) used for absolute frequency calibration.

following the results of the measurements are presented and discussed.

#### *Isotope shift measurements*

The IS of an atomic transition consists of two different contributions. One is related to the finite mass of the nucleus and is commonly referred to as the *mass shift* (MS), while the other is due to the non-zero size of the nucleus and is called the *field shift*

(FS) [6]. The latter is dominant in heavy elements ( $Z > 60$ ), while the former prevails in light elements ( $Z < 30$ ). For a medium-weight element like Xenon both effects give a significant contribution.

The mass shift in a transition  $a$  can again be expressed as the sum of two contributions,  $MS_a^{A',A} = NMS_a^{A',A} + SMS_a^{A',A}$ , where  $A'$  and  $A$ , are the isotope mass numbers. The first contribution is the *normal mass shift* (NMS, also called Bohr Shift) It is given, to a good approximation, by  $NMS_a^{A',A} = M^{A',A} \frac{m_e}{m_u} \nu_a$  where  $m_e$ ,  $m_u$  are the electron mass and atomic mass unit respectively,  $\nu_a$  is the transition frequency and  $M^{A',A} = \frac{A'-A}{A'A}$ . Hence the NMS of a transition can be easily evaluated provided that the transition frequency is accurately known. The second contribution is the *specific mass shift* (SMS), that arises from the correlated electron momenta. Although there exists no simple expression for the SMS, its dependence on the isotopic masses is the same as that for the NMS, thus it is possible to express the MS as the product of two factors,  $MS_a^{A',A} = K_a \cdot M^{A',A}$ , where the  $K_a$  factor depends only on the electronic transition [6].

In a similar fashion the field shift can be factorized as  $FS_a^{A',A} = F_a \cdot C^{A',A}$ , where the  $F_a$  factor is proportional to the change in the non-relativistic electronic density at the nucleus when the atom undergoes the transition  $a$ , while the quantity  $C^{A',A}$  is, to a good approximation, the change in the mean square nuclear charge radius between isotopes with atomic mass  $A'$  and  $A$ , i.e.  $C^{A',A} \approx \delta \langle r^2 \rangle^{A',A}$  [17].

**Table 6.3:** Results of isotope shift measurements,  $IS^{136,A} = \nu^{136} - \nu^A$  (in MHz). Reported uncertainties are  $1\sigma$ .

$A$	$5d'[3/2]_1$	$8d[1/2]_1$	$8d[3/2]_1$	$7s'[1/2]_1$
134	203(10)	207(12)	219(15)	213(12)
132	351(18)	384(18)	354(20)	365(18)
131	470(11)	531(23)	545(17)	492(20)
130	509(13)	557(11)	529(30)	523(24)
129	591(19)	675(14)	684(27)	678(24)
128	667(12)	747(19)	726(20)	692(22)
126	821(14)		912(20)	869(25)
124	1008(20)		1116(20)	1069(22)

The measured IS are presented in Table 6.3. The heaviest  $^{136}\text{Xe}$  isotope is chosen as a reference to express the isotope shifts, given as  $IS^{136,A} = \nu^{136} - \nu^A$ , where  $\nu^A$  is the frequency of the transition measured for the isotope with atomic mass  $A$ . The reported values are averaged over 4 to 18 measurements depending on the number of scans recorded for each isotope; the errors are  $1\sigma$ . In the weaker  $8d[1/2]_1$  transition the two less abundant  $^{126}\text{Xe}$  and  $^{124}\text{Xe}$  isotopes are not observed.

For the two odd isotopes the IS are evaluated from the center of gravity of the

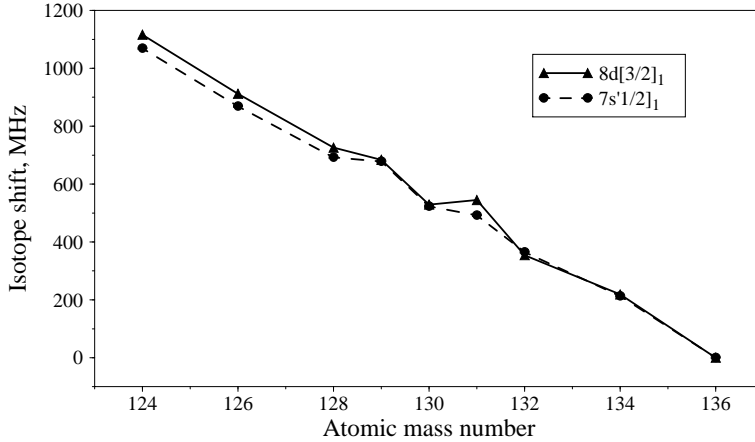


**Figure 6.5:** Measured isotope shift as function of the atomic mass number, for the  $8d[3/2]_1$  and  $7s'[1/2]_1$  transitions. The experimental uncertainty is about 20 MHz.

measured  $HFS$ . According to the “odd-even staggering” phenomenon they do not lie midway between the two neighboring even isotopes, but lie closer to the lighter one [18]. This is graphically shown in Fig. 6.5, where the measured  $IS^{136,A}$  of the  $8d[3/2]_1$  and  $7s'[1/2]_1$  transitions are plotted against the atomic mass number  $A$ . Fig. 6.5 shows also the anomaly for  $^{136}\text{Xe}$ , related to the neutron shell closing at  $N = 82$ . These effects reflect the change of the mean square nuclear charge radius between isotopes. In our analysis the attention is focused on an interpretation of the IS with the aim to extract information on the electronic structure of the atom. This implies that all the information on the nuclear charge distribution, contained in the  $C$ -factors, will be divided out, leaving only the effect of the electronic structure, contained in the  $K_a$  and  $F_a$  factors.

In order to extract physical information from the measured IS the two contributions must be separated. For that purpose, the modified IS is introduced, defined as  $IS^{A',A}$  divided by the factor  $M^{A',A}$ , and for which the following equation applies:

$$IS_a^{A',A}/M^{A',A} = K_a + F_a \cdot C^{A',A}/M^{A',A}. \quad (6.3)$$

Here  $C^{A',A}/M^{A',A}$  are the so-called modified  $C$ -factors. When the modified  $C$  factors are known they can be plotted against the modified IS and a straight line is obtained, the slope and intercept of which give  $F_a$  and  $K_a$  respectively (King plot). The  $K_a$  factor, which is related to the SMS, has no straightforward interpretation since its theoretical evaluation requires complicated many-body atomic structure calculations. The  $F_a$  factor, on the contrary, gives direct insight into the electronic density at the nucleus.

To perform the IS analysis a set of  $C$  values has to be assumed. Two different sets for Xe are reported in the literature [19,20], that differ by about a factor of 2. Both sets

have been extracted from IS measurements involving excited states, of which one has an  $s$ -electron configuration. In such a transition the  $F_a$  factor can be evaluated since the change in the electronic density at the nucleus is mainly determined by the  $s$ -electron plus a small screening contribution from the non  $s$ -electron. The difference in the two sets reflects in fact that a different estimation for the SMS contribution is used to extract the FS from the measured IS. More refined explanations on nuclear structure effects in IS can be found in [6, 19, 20].

**Table 6.4:** Values of the IS factors deduced using the  $C$  factors reported by Schneider [19].

	$5d'[3/2]_1$	$8d[1/2]_1$	$8d[3/2]_1$	$7s'[1/2]_1$
$F_a$ (GHz fm $^{-2}$ )	2.31(33)	1.95(24)	3.04(28)	2.70(30)
$K_a$ (GHz)	1130(52)	1363(39)	1165(43)	1151(46)

The results of the data analysis are summarized in Table 6.4, where the IS factors,  $F_a$  and  $K_a$ , for the four investigated transitions are shown. The  $F_a$  factors obtained using the  $C$  values from Aufmuth *et al.* [20] are consistent, within the error margins, with those reported in Table 6.4. Discrepancies appear in the  $K_a$  factors only, being systematically smaller. This fact reflects the different SMS values assumed to derive the two sets of  $C$ -factors. Our measurements yield a high value for the  $F_a$  factors even in the transitions in which no  $s$ -electron is involved. These values can be compared for example with the value of -2.3 GHz fm $^{-2}$  reported by Geisen *et al.* [17] for the  $(6s[3/2]_2 - 5d[3/2]_3)$  transition. The present results are consistent with what reported by Plimmer *et al.* [15], who measured the IS in the two-photon transition between the ground state and the  $6p[1/2]_0$  excited state, from which a value of 2.49 GHz fm $^{-2}$  follows. Since the  $F_a$  factor is proportional to the change in the electronic density at the nucleus, the results of the present measurements clearly show a large contribution of the removal of the  $5p$ -electron from the closed shell, which strongly decreases the screening of the inner  $s$ -electrons.

#### *Absolute frequency calibration*

The results from absolute calibration of the resonance frequencies, performed on three transitions ( $8d[1/2]_1$ ,  $8d[3/2]_1$ ,  $7s'[1/2]_1$ ) are reported in Table 6.5. The frequencies of the “t” hyperfine component of the  $I_2$  lines,  $\nu(I_2)$ , are taken from the new atlas of reference lines [16]. The measured values for the frequency difference between the Xe isotope line and the “t”-component of the  $I_2$  calibration line,  $\Delta\nu(A_{ref}, I_2)$ , are given in cm $^{-1}$  (see Table. 6.5). These are averaged values from 5 to 8 measurements, depending on the number of spectra recorded; the uncertainties represent  $1\sigma$ . The absolute frequency for the reference Xe isotope line is obtained as  $\nu(A_{ref}) = \Delta\nu(A_{ref}, I_2) + 6 \times \nu(I_2)$ , where the factor 6 reflects the fact that the  $I_2$  saturated absorption lines are measured with the fundamental frequency. The uncertainty in  $\nu(A_{ref})$  is due to the experimental errors in  $\Delta\nu(A_{ref}, I_2)$  plus a possible contribution due to frequency chirp arising in the PDA. This is estimated to be less than 0.003 cm $^{-1}$  [1, 10] and is the main source of error in

the absolute calibration. Previous results from classical absorption spectroscopy [21] are reported for comparison in the last row of Table 6.5. However, here no isotope is specified since the individual isotope lines have not been resolved. The present results are fully consistent with previous data but improve the accuracy by almost two orders of magnitude.

**Table 6.5:** Absolute calibration of transition frequencies from the ground state (values in  $\text{cm}^{-1}$ ). The first and second rows denote the Xe isotope and the  $I_2$  reference line.  $\nu(I_2)$  is the frequency of the “t” hyperfine component of this  $I_2$  line,  $\Delta\nu(A, I_2)$  the measured frequency difference between the reference Xenon isotope line and this “t”-component in the VUV frequency scale,  $\nu(A)$  is the absolute frequency of the Xenon line for the reference isotope. In the last row the value from Yoshino and Freeman [21] is given for comparison.

	$8d[1/2]_1$	$8d[3/2]_1$	$7s'[1/2]_1$
$A$	136	136	132
$I_2$	P30(7-4)	P68(8-4)	R95(10-4)
$\nu(I_2)$	15704.88007(3)	15780.92844(3)	15966.65174(3)
$\Delta\nu(A, I_2)$	-1.2617(12)	-0.08839(57)	0.67629(61)
$\nu(A)$	94228.0187(32)	94685.4822(30)	95800.5867(30)
From [21]	94228.02(20)	94685.47(20)	95800.70(20)

From the absolute calibration of the  $8d[1/2]_1$  transition it is possible to derive a new and more accurate value of the ionization energy of  $^{136}\text{Xe}$ . Knight and Wang [22] performed laser spectroscopy of the  $nf[3/2]_1$  ( $n > 24$ ) Rydberg series in Xe, resulting in an ionization limit of  $21637.02(1) \text{ cm}^{-1}$  above the  $6s'[1/2]_0$  level. A value of the ionization energy of  $E_{3/2} = 97833.81(10) \text{ cm}^{-1}$  was reported as well, based on the value of the energy of the  $6s'[1/2]_0$  level of  $76196.79(10) \text{ cm}^{-1}$ . However, from the high precision interferometric measurements on enriched  $^{136}\text{Xe}$  sample by Humphreys and Paul [23], energy separation between  $6s'[1/2]_0$  and  $8d[1/2]_1$  levels of  $18031.2339(14) \text{ cm}^{-1}$  can be deduced. This value, combined with the absolute calibration of the energy of the  $8d[1/2]_1$  level in  $^{136}\text{Xe}$ , gives an energy of the  $6s'[1/2]_0$  level of  $76196.7848(35) \text{ cm}^{-1}$ . Finally, a value for the ionization energy for  $^{136}\text{Xe}$  of  $E_{3/2}^{136} = 97833.805(11) \text{ cm}^{-1}$  is deduced.

It has to be pointed out that in the experiment of Knight and Wang [22] isotopes have not been resolved, hence, in order to validate the present result, an estimate has to be given of the IS in the transitions measured. Using the results reported by Jackson and Coulombe [24] ( $IS_{(6s'[1/2]_0-5f[3/2]_1)}^{136,130} = -84(9) \text{ MHz}$ ), an upper limit of  $0.003 \text{ cm}^{-1}$  for the  $IS^{136,130}$  in the transitions studied in [22] can be estimated. This shift does not affect the present result.

### 6.2.4 Conclusions

In this Section the results of high-resolution VUV-laser spectroscopy of Xenon are presented. Tunable narrow-band VUV pulses near 105 nm wavelength are used to investigate transitions from the ground state to four excited states,  $5d'[3/2]_1$ ,  $8d[1/2]_1$ ,  $8d[3/2]_1$  and  $7s'[1/2]_1$  by two-photon ionization spectroscopy. A time-of-flight mass spectrometer allows to resolve the transitions of all nine stable isotopes. Using values reported in the literature for the change in mean-square nuclear charge radii, isotope shift factors are evaluated, and field shift and mass shift contributions are separated. The field factor turns out to be high, even when no  $s$ -electron is involved in the transition. This leads to the conclusion that the removal of a  $p$ -electron from the ground state's closed shell strongly increases the electronic density at the nucleus. This result may stimulate *ab initio* many-body calculations that can reveal the screening effect of  $p$ -electrons in a closed shell configuration.

For three of the transitions absolute frequency calibration is also performed. This results in an improved by two orders of magnitude accuracy for the absolute energies of the investigated levels compared with previous measurements. A new value for the ionization energy of  $^{136}\text{Xe}$  is derived with an accuracy of about one order of magnitude higher than the previous value.

## 6.3 Precision XUV spectroscopy of $\text{N}_2$ around 98 nm\*

In a high-resolution laser spectroscopic study, using a tunable Fourier-transform limited light source in the extreme ultraviolet, the  $b^1\Pi_u$   $v=1$  excited valence state of molecular nitrogen is investigated.

### 6.3.1 Introduction

Transition frequencies for several rotational lines in the  $b^1\Pi_u - X^1\Sigma_g^+(1,0)$  band of molecular nitrogen are determined at very high accuracy, yielding improved rotational constants for the  $b^1\Pi_u$ ,  $v=1$  state.

### 6.3.2 Experimental

The experimental setup is similar to the one used previously for the study of the  $^1\Sigma_u^+$  states of  $\text{N}_2$  [25], while details of the experimental methods are explained in Ref. [26] and Section 6.1.2 of this Thesis. Tunable XUV-radiation is produced with a laser system consisting of a chain of a stabilized CW-ring dye laser in the range 570-600 nm (Rhodamine 6G), a pulsed-dye-amplifier pumped by a powerful Nd:YAG laser, frequency-doubling in a KDP-crystal and third-harmonic generation in a pulsed jet of xenon gas. This chain delivers coherent XUV-light with a bandwidth in the range 250-350 MHz, dependent on specific conditions in the dye amplifier. The value for the instrument width involves for the major part the bandwidth of the XUV-source and an additional effect of residual

---

\*an excerpt from Journal of Chemical Physics **112** 5711-5716 (2000).

Doppler broadening in the crossed beam configuration. The latter depends on the specific geometry chosen, the diameters of the nozzle opening and skimmer as well as the divergence of the XUV beam.

Spectroscopy of  $N_2$  is performed via 1 XUV + 1 UV photo-ionization in a setup where the XUV-beam is perpendicularly crossed with a collimated beam of pure nitrogen gas obtained from a pulsed valve. In the collision-free expanding jet of  $N_2$  only the lowest rotational states were accessible for investigation. Simultaneously with the  $N_2$  spectra in the XUV-domain the visible output from the CW-ring dye laser is used to record markers of a stabilized etalon (Free Spectral Range 148.9560(5) MHz) and a saturated absorption spectrum of molecular iodine for absolute frequency calibration. The accurately calibrated reference lines were obtained either from Ref. [27] (*see also Chapter 5*) or specifically calibrated in our laboratory during the measurements.

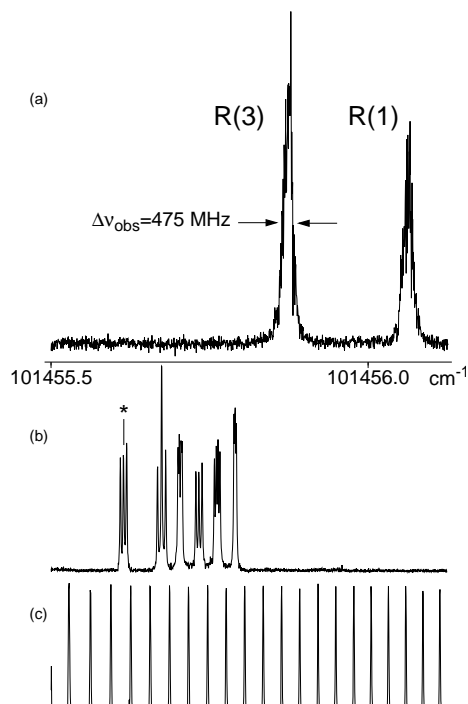


**Figure 6.6:** (a) Spectrum of the  $R(1)$  and  $R(3)$  lines in the  $b^1\Pi_u - X^1\Sigma_g^+(1,0)$  band of  $N_2$  at  $\lambda=98.56$  nm recorded with the pulsed tunable XUV-source; (b) simultaneously recorded  $I_2$ -saturation spectrum for absolute calibration with the CW-output of the ring dye laser at the fundamental wavelength  $\lambda=591.39$  nm; the line marked by (\*) is the “t” hyperfine component of the  $B-X(13-1)R95$  line of  $I_2$  at  $16909.26600$   $\text{cm}^{-1}$ ; (c) simultaneously recorded etalon markers with  $\text{FSR}=149.9560$  MHz.

### 6.3.3 Results

**Table 6.6:** Accurately calibrated lines in the  $b^1\Pi_u - X^1\Sigma_g^+(1,0)$  band of  $N_2$  and deviations from a least squares fit. Note that in the listed frequencies a possible systematic overall shift of  $0.003\text{ cm}^{-1}$ , due to the chirp effect, is not accounted for.

Line	Frequency, $\text{cm}^{-1}$	Obs.-calc.
$R(0)$	101 454.411 $\pm$ 0.001	0.001
$R(1)$	101 456.062 $\pm$ 0.001	-0.001
$R(2)$	101 456.551 $\pm$ 0.001	0.000
$R(3)$	101 455.873 $\pm$ 0.001	-0.002
$R(4)$	101 454.031 $\pm$ 0.001	-0.001
$Q(2)$	101 448.105 $\pm$ 0.001	0.000
$Q(3)$	101 444.615 $\pm$ 0.001	0.000
$Q(4)$	101 439.960 $\pm$ 0.001	0.000
$P(2)$	101 442.474 $\pm$ 0.001	0.001
$P(3)$	101 436.168 $\pm$ 0.001	0.000
$P(4)$	101 428.700 $\pm$ 0.001	0.001
$P(5)$	101 420.066 $\pm$ 0.001	-0.001

**Table 6.7:** Frequency separations between sets of lines in the  $b^1\Pi_u - X^1\Sigma_g^+(1,0)$  band of  $N_2$ .

Lines	Frequency separation, MHz	Obs.-Calc.
$R(1)-R(3)$	5663 $\pm$ 27	-25.5
$R(0)-R(4)$	11374 $\pm$ 25	-39.5
$R(1)-R(2)$	14578 $\pm$ 50	64.6
$Q(1)-R(5)$	17687 $\pm$ 50	23.0

In Fig. 6.6 a spectral recording of the  $R(1)$  and  $R(3)$  lines of the  $b^1\Pi_u - X^1\Sigma_g^+(1,0)$  band is shown with simultaneously recorded etalon and  $I_2$ -reference spectra. The superior characteristics of the tunable XUV-source allow for the first time to fully resolve these lines in this bandhead region. The line marked with (\*) in the  $I_2$ -reference spectrum is the “t” hyperfine component of the  $R95$  transition in the  $B-X(13-1)$  band of  $I_2$  at  $16909.26600(7)\text{ cm}^{-1}$  [27]. The absolute frequency position of the  $N_2$ -lines is related, via the etalon markers, to this reference line. From a series of measurements a value for the transition frequency is obtained with a ( $2\sigma$ ) accuracy of  $0.001\text{ cm}^{-1}$  or 30 MHz. As outlined previously [26, 28] some systematic effects should be accounted for in evalu-

ating absolute transition frequencies. Similar as in previous work the residual Doppler shift was addressed by varying the flow speed of the nitrogen molecules in the molecular beam expansion. The effect of a net shift of the resonance frequency by frequency chirp generated in the dye-amplifier [28] was not addressed in the present study. Since the measured N<sub>2</sub>-resonances are in a small wavelength interval it is a valid assumption that the frequency separations between lines are not affected by this chirp; in the absolute frequencies chirp may result in a maximum uncertainty of 100 MHz or 0.0033 cm<sup>-1</sup>. In Table 6.6 the measured frequency positions of N<sub>2</sub>-resonances are listed (neglecting this chirp-induced uncertainty), while in Table 6.7 the measured frequency separations are given. The absolute frequencies could in some cases be directly related to the “t” components of lines in the *B-X*(*v*',1) bands of molecular iodine for *v*'=13-18, as presented in the work of Velchev *et al.* [27]. However some N<sub>2</sub>-resonances were calibrated with respect to other I<sub>2</sub>-lines. These other reference lines, listed in Table 6.8, were for the purpose of this study calibrated in our laboratory, following the procedures of Ref. [27].

**Table 6.8:** Frequencies of newly calibrated reference lines of I<sub>2</sub>. In all cases we refer to the “t” hyperfine component [27]

Assignment	Frequency, cm <sup>-1</sup>
<i>B-X</i> (15,2) <i>P</i> 85	16908.11161 ± 0.00007
<i>B-X</i> (15,2) <i>R</i> 91	16905.91406 ± 0.00007
<i>B-X</i> (16,2) <i>P</i> 126	16907.56713 ± 0.00007
<i>B-X</i> (16,2) <i>P</i> 127	16904.70045 ± 0.00007
<i>B-X</i> (16,2) <i>R</i> 131	16906.58866 ± 0.00007

**Table 6.9:** Molecular constants for the *b*<sup>1</sup>Π<sub>u</sub>, *v*=1 state of N<sub>2</sub> derived from absolute line positions (Table 6.6), frequency separations (Table 6.7), and values from Ref. [29]. All values in cm<sup>-1</sup>.

$\nu_0$	101453.0022 ± 0.0006 <sup>a</sup>
<i>B</i>	1.40805 ± 0.00006
<i>D</i>	1.589 × 10 <sup>-5</sup> ± 7 × 10 <sup>-8</sup>
<i>q</i>	-4 × 10 <sup>-5</sup> ± 4 × 10 <sup>-5</sup>

<sup>a</sup>This value follows from the least squares fit; due to the chirp effect a possible systematic error of 0.003 cm<sup>-1</sup> should be taken as the true value.

The present absolute frequency positions and frequency separations between lines of the *b*<sup>1</sup>Π<sub>u</sub> – *X*<sup>1</sup>Σ<sub>g</sub><sup>+</sup>(1,0) band are included in a combined least-squares fit with the lower

resolution data of Ref. [29] using the energy expression:

$$E(J) = \nu_{10} + B[J(J+1) - 1] - D[J(J+1) - 1]^2 + q[J(J+1) - 1], \quad (6.4)$$

where the last term proportional to the  $\Lambda$ -doubling parameter  $q$  only holds for the levels of ( $f$ ) symmetry probed in the  $Q$ -branch. The data points were weighted in the fit according to the uncertainties to derive a weighted  $\chi^2$ -value. The present absolute frequencies are included with the uncertainty of  $0.001 \text{ cm}^{-1}$ , while the frequency separations were given the uncertainties as listed in Table 6.7. For the older data from Ref. [29] uncertainties of  $0.03 \text{ cm}^{-1}$  (for the lower  $J$ ) and  $0.06 \text{ cm}^{-1}$  (for  $J > 18$ ) were taken; blended lines were given an uncertainty of  $0.15 \text{ cm}^{-1}$ . We found that the  $R(2)$  line in Ref. [29] contained a typing error and should read  $101456.602 \text{ cm}^{-1}$ . For the electronic ground state improved parameters have become available in recent years. We adopt the constants derived from a simultaneous reanalysis of several bands by *Trickett al.* [30];  $B_0=1.9895776(1) \text{ cm}^{-1}$ ,  $D_0=5.74137(100)\times 10^{-6} \text{ cm}^{-1}$ ,  $H_0=4.843(1.000)\times 10^{-12} \text{ cm}^{-1}$ . These ground state constants were kept fixed in the fit.

The weighted fit resulted in a summed  $\chi^2$  of 104 for the set of 84 data points. This implies that the uncertainties are somewhat underestimated. However this underestimation is not in the presently obtained highly accurate data; for the 12 data points a summed  $\chi^2$  of 7 is obtained. Because of this internal consistency these data were not assigned with an uncertainty related to the possible overall shift of  $0.003 \text{ cm}^{-1}$  due to the frequency chirp in the laser. The resulting molecular constants for the  $b^1\Pi_u$ ,  $v=1$  excited state are presented in Table 6.9. The stated uncertainties represent  $1\sigma$ . The rotational constants  $B$  and  $D$  are in agreement with previous findings within  $2\sigma$ . The  $\Lambda$ -doubling parameter  $q$ , previously not included, does not significantly differ from zero even with the high precision measurements. The band origin  $\nu_0$  is lower by  $0.05 \text{ cm}^{-1}$  with respect to the previous lower resolution study [29]. This systematic shift is reflected in the data sets of the present and previous experiments; the presently obtained frequencies are on average lower by  $0.05 \text{ cm}^{-1}$ . We have no explanation for this discrepancy. In view of the much higher resolution in the present study and the improved absolute calibration method the present data are more reliable. This implies that the values of Ref. [29] might have to be shifted by  $0.05 \text{ cm}^{-1}$ .

### 6.3.4 Conclusion

Ultra-high resolution XUV-excitation spectra of the  $b^1\Pi_u - X^1\Sigma_g^+(1, 0)$  band have been recorded. Techniques of pulsed-dye amplification and harmonic generation, in combination with on-line saturation spectroscopy of  $\text{I}_2$  have been applied to determine absolute frequencies of  $\text{N}_2$  transitions in the XUV-domain with unprecedented accuracy. These techniques could also be employed for other bands, but in the corresponding wavelength ranges no  $\text{I}_2$  frequency standards are available yet. Future calibrations could easily deliver absolute transition frequencies in the (5,0) and (6,0) bands with almost the same accuracy.

## Acknowledgment

This work was financially supported by the Netherlands Foundation for Fundamental Research of Matter (FOM).

## References

- [1] K. S. E. Eikema, W. Ubachs, W. Vassen, W. Hogervorst, Phys. Rev. A **55**, 1866 (1997)
- [2] K. S. E. Eikema, W. Ubachs, W. Hogervorst, Phys. Rev. A **49**, 803 (1994)
- [3] T. Trickl, M. J. J. Vrakking, E. Cromwell, Y. T. Lee, A. H. Kung, Phys. Rev. A **39**, 2948 (1989)
- [4] J. Bömmels, J. M. Weber, A. Gopalan, N. Herschbach, E. Leber, A. Schramm, K. Ueda, M. -W Ruf, H. Hotop, J. Phys. B **32**, 2399 (1999)
- [5] L. Minnhagen, J. Opt. Soc. Am. **63**, 1185 (1973)
- [6] W. H. King, *Isotope Shifts in Atomic Spectra* (Plenum, New York, 1984)
- [7] L. Veseth, J. Phys. B **18**, 3463 (1985)
- [8] C. J. Sansonetti, J. Opt. Soc. Am. B **14**, 1913 (1997)
- [9] For notations of the hyperfine components in iodine saturation spectrum and the calibration procedure see I. Velchev, R. van Dierendonck, W. Hogervorst, W. Ubachs, J. Mol. Spectrosc. **187**, 21 (1998)
- [10] S. Gangopadhyay, N. Melikechi, E. E. Eyler, J. Opt. Soc. Am. B **11**, 231 (1994); Eyler E E, Yiannopoulou A, Gangopadhyay S and Melikechi N, Opt. Lett. **22**, 49 (1997)
- [11] G. Norlén, Ark. Fys. **35**, 119 (1967)
- [12] C. Yamada, H. Kanamori, E. Hirota, J. Chem. Phys. **83**, 552 (1985)
- [13] A. M. Wapstra, K. Bos, At. Data Nucl. Data Tables **19**, 177 (1977)
- [14] I. Velchev, W. Hogervorst, and W. Ubachs, J. Phys. B **32**, L511 (1999).
- [15] M. D. Plimmer, P. E. G. Baird, C. J. Foot, D. N. Stacey, J. B. Swan, and G. K. Woodgate, J. Phys. B **22**, L241 (1989).
- [16] S. C. Xu, R. van Dierendonck, W. Hogervorst, and W. Ubachs, J. Mol. Spectrosc. **201**, 256 (2000).
- [17] H. Geisen, T. Krumpelmann, D. Neuschafer, and Ch. Ottinger, Phys. Lett. A **130**, 299 (1988).
- [18] P. Aufmuth and M. Haunert, Physica B & C **123C**, 109 (1983).
- [19] F. Schneider, *PhD Thesis* (Freie Universität Berlin, 1985), p. 168.
- [20] P. Aufmuth, K. Heilig, and A. Steudel, At. Data Nucl. Data Tables **37**, 455 (1987).
- [21] K. Yoshino, and D. E. Freeman, J. Opt. Soc. Am. B **2**, 1268 (1985).
- [22] R. D. Knight, and L. -G. Wang, J. Opt. Soc. Am. B **2**, 1084 (1985).
- [23] C. J. Humphreys, and E. Paul Jr., J. Opt. Soc. Am. B **60**, 1302 (1970).
- [24] D. A. Jackson, and M. C. Coulombe, Proc. R. Soc. Lond. A **343**, 453 (1975).
- [25] W. Ubachs, Chem. Phys. Lett. **268**, 201 (1997)
- [26] W. Ubachs, K. S. E. Eikema, W. Hogervorst, P.C. Cacciani, J. Opt. Soc. Am. B **14**, 2469 (1997)
- [27] I. Velchev, R. van Dierendonck, W. Hogervorst, W. Ubachs, J. Mol. Spectrosc. **187**, 21 (1998)
- [28] K. S. E. Eikema, W. Ubachs, W. Vassen, W. Hogervorst, Phys. Rev. A **55**, 1866 (1997)
- [29] W. Ubachs, L. Tashiro, R.N. Zare, Chem. Phys. **130**, 1 (1989)
- [30] T. Trickl, D. Proch, K.L. Kompa, J. Mol. Spectrosc. **171**, 374 (1995)

# Chapter 7

## Table-top narrow-band XUV laser source.

The design of a new coherent narrow-band XUV laser source, based on high-harmonic generation of powerful infrared (IR) pulses is introduced. Wavelength-tunable, Fourier-transform limited laser pulses of 300 ps duration are produced by injection-seeded pulse-dye-amplifier (PDA) pumped by stimulated Brillouin scattering (SBS) compressed output of a single longitudinal mode, Q-switched Nd:YAG laser. The pulses with 10 Hz repetition rate are subsequently amplified in a Ti:Sapphire crystal in multi-pass configuration. High-harmonic generation in both expanding gas-jet and hollow fiber are discussed.

### 7.1 Introduction

Tunable radiation in the extreme ultra-violet (XUV) range (50 - 100 nm) can be generated by frequency up-conversion of the output of powerful nano-second pulsed laser sources. In the set-up, described in Chapter 6.1.2 (Fig. 6.1), vacuum ultraviolet light at 105 nm is generated in two consecutive steps: efficient ( $\approx 25\%$ ) second harmonic generation in KD\*P crystal, followed by relatively inefficient third-harmonic generation in a free expanding Xe gas jet. The accessible wavelength range with this system is limited to  $\approx 70$  nm, due to the transparency cut-off of the SHG crystals at about 200 nm. When 5th harmonic is used as a second step, the deep extreme ultraviolet (XUV) region becomes accessible, although, the conversion efficiency is much lower. The latter scheme was used by Eikema *et al.* [1] in their measurement of the Lamb-shift in the helium ground state. Visible pulses, tunable around 584 nm were frequency doubled and subsequently quintupled to reach 58.4 nm region with a bandwidth of  $\delta\nu/\nu \approx 5 \times 10^{-8}$ .

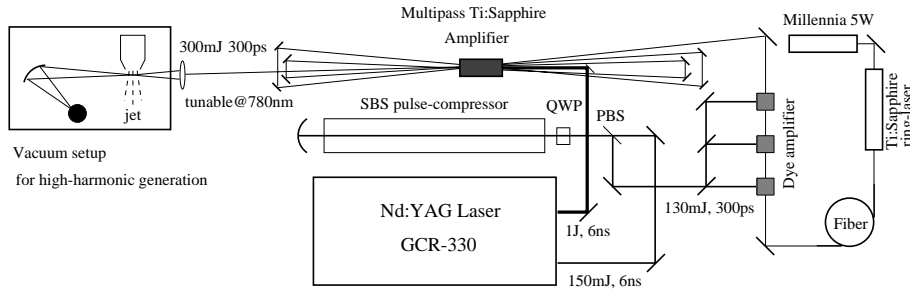


**Figure 7.1:** Table-top narrow-band XUV laser source based on high-harmonic generation of powerful IR pulses.

Alternatively, with high-peak intensity femto-second laser pulses the water window at 2-4 nm can be reached via high-harmonic generation; the spectral resolution, however, is very poor. We aim at reaching wavelengths as short as 30 nm, with tunability and spectral purity orders of magnitude better than the synchrotron sources usually used for spectroscopy in this wavelength region.

In this Chapter we present a new design of a laser system, which generates powerful Fourier-transform limited 300 ps pulses tunable in wavelength within the Ti:Sapphire range with a bandwidth  $\delta\nu/\nu \approx 3 \times 10^{-6}$ . In Fig. 7.1 a scheme of the set-up is shown. The frequency *clock* for the experiment is a CW Ti:Sapphire ring-laser, pumped by a frequency-doubled (532 nm) solid-state CW laser (Section 7.2). This narrow-band ( $\sim 1$  MHz) tunable radiation, transmitted through a short polarization-maintaining single-mode fiber (Section 7.3), is used for injection seeding of a three-stage pulse-dye-amplifier (PDA) pumped by 300 ps Fourier-transform limited pulses from the compressed secondary output of an injection seeded, Q-switched and frequency-doubled Nd:YAG laser (Section 7.4). The pulse compression from 6 ns down to 300 ps (factor of 20) is achieved by stimulated Brillouin scattering in a water cell [2] (*see* also Chapter 2 of this Thesis). After the dye amplification pulses of 300 ps and energy  $\sim 2$  mJ/pulse are obtained and further amplified in a multi-pass Ti:Sapphire amplifier pumped by the main frequency-doubled output (6 ns, 1 J @ 532nm) of Nd:YAG laser (Section 7.5). Pulses of  $\sim 300$  mJ and 300 ps duration can in principle be achieved after the amplification stage. Such powerful, narrow-band, tunable over a broad wavelength range pulses, can generate high-harmonics (*see* Section 1.3), reaching wavelengths of 30 nm (25th harmonic of 780 nm), either in a pulsed gas jet (focusing geometry), or in a gas-filled hollow fiber (guided geometry).

## 7.2 Continuous-wave part of the setup

The fundamental frequency is provided by a Ti:Sapphire ring-laser (Coherent 899-21), pumped by a 5 W frequency-doubled diode-pumped Nd:YVO<sub>4</sub> laser (Spectra Physics Millennia V). Wavelengths within the Ti:Sapphire amplification range are generated with 550 mW maximum output power and 1 MHz bandwidth (Fig. 7.2). The narrow-band, single longitudinal mode operation of the laser is ensured by a set of intra cavity passive frequency-selective elements, unidirectional device (optical diode), and an active frequency control. A Brewster-angle birefringent Lyot filter allows broadband operation (2 GHz) and coarse frequency selection. Two low-finesse etalons of different thickness reduce the bandwidth to 10 MHz. The active frequency stabilization is realized by locking the laser resonator to a temperature-stabilized reference cavity, further reducing the line-width to  $\sim 1$  MHz. Continuous single-mode scanning ranges up to 30 GHz.

By using a wedge (Fig. 7.2), two reflected beams are created from the main laser beam: one is sent to a high-finesse etalon used for relative frequency measurements, while the other is sent to a wavelength-meter for absolute wavelength measurement. The signal from the two-beam interference on a plane parallel-plate (P) in the etalon beam is used for laser-frequency tracking and eventual mode-hop detection; its reflection signal is detected by a photo-diode (PD). After the wedge the laser beam passes through an

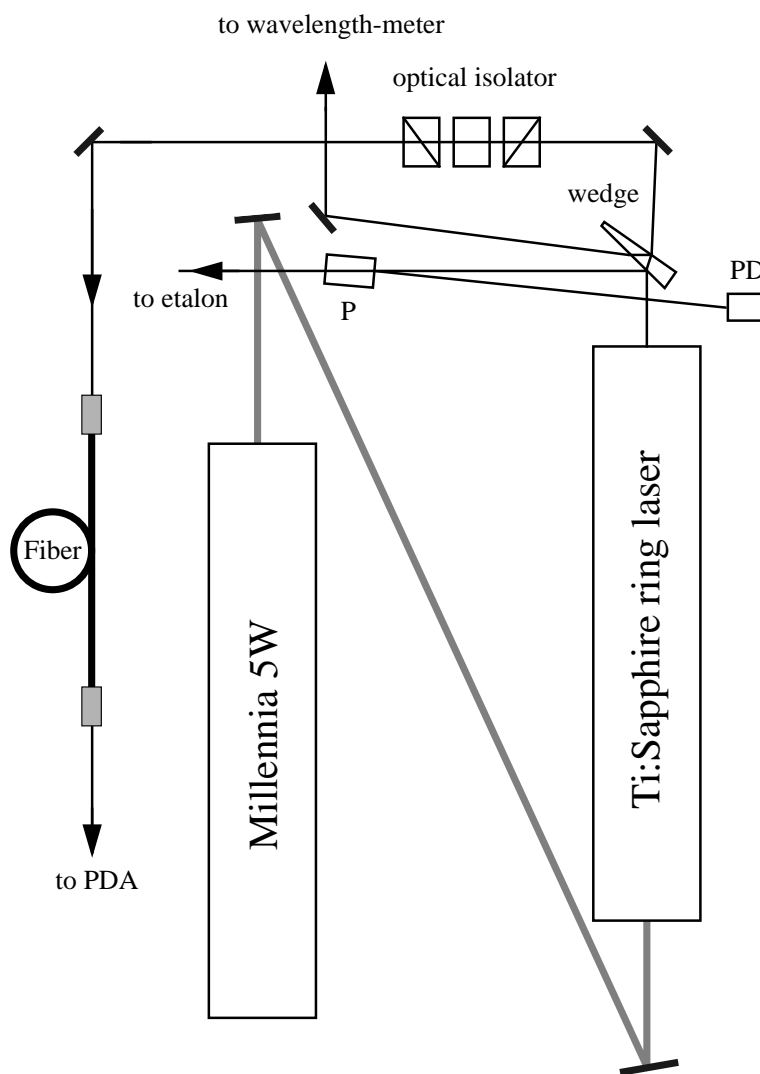


**Figure 7.2:** Scheme of the continuous-wave part of the setup. P - plane-parallel plate used as low-finesse etalon; PD - photodiode.

optical isolator and is launched into a short polarization-maintaining single-mode optical fiber. The optical isolator ensures that light, reflected from the tip of the fiber, is not sent back into the ring-laser.

### 7.3 The fiber connection

In order to transport the CW light to the pulsed part of the set-up we use single-mode polarization-maintaining fiber. In this Section we elaborate on the use of optical fibers for laser light transmission. The positive and negative aspects of CW fiber-connections are discussed.

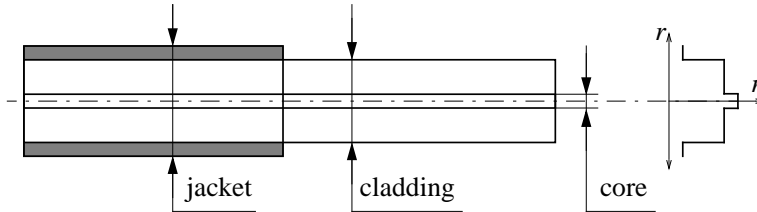


**Figure 7.3:** Schematic illustration of the structure of step-index fiber and the refractive-index profile.

The principle of total internal reflection, known from the nineteenth century [3], is responsible for guiding light through an optical fiber. In Fig. 7.3 a longitudinal section of a simple (step-index) fiber is presented along with a graph of the refractive-index *vs.* radial distance. The light is guided in the central *core*, which has the highest index of refraction ( $n_{core}$ ). The core is surrounded by a thick region (*cladding*) with slightly lower index of refraction ( $n_{cladding} = (1 - \Delta)n_{core}$ ;  $\Delta \approx 3 \times 10^{-3}$ ) [4]. The core-cladding structure is surrounded by a plastic *jacket* (see Fig. 7.3). It makes the stiff and fragile silica fiber flexible and mechanically resistant to bending and strain.

An important parameter when choosing an optical fiber is its optical losses. Material absorption and spontaneous Rayleigh scattering are the main sources of low-signal losses, which are usually of the order of 1-10 dB/km in the visible and near-IR. From a practical point of view, the most significant material absorption is caused by OH at  $2.73 \mu\text{m}$ ,  $1.37 \mu\text{m}$  and  $1.23 \mu\text{m}$ . The Rayleigh scattering, due to its  $\omega^4$  frequency dependence, dominates the optical losses in the visible. Bending and boundary losses are less prominent, but should be considered as well.

Single-mode fibers can support two degenerate modes, polarized in two orthogonal directions. In the ideal case of perfect cylindrical geometry and isotropic material, a mode excited with polarization in the *x* direction would not couple to the orthogonal *y*-polarized mode. However, in practice, even small deviations from cylindrical geometry or small material anisotropy result in a mixing of the two polarization states by breaking the mode degeneracy. This effect is referred to as *modal birefringence* and, in a conventional single-mode fiber, leads to scrambling of the polarization state of initially linearly polarized light. For many applications it is crucial that the fiber transmits the light preserving its polarization state. When a large amount of birefringence is introduced in the fiber during the fabrication process, small random birefringence fluctuations do not affect the polarization state of the guided light. Such fibers are called *polarization-*

*maintaining* fibers. Linearly polarized light with polarization axis coinciding with one of the axes of the induced birefringence, remains linear during propagation. Since we are interested in transmission of CW light used for injection seeding, both minimal optical losses and polarization stability are crucial. The use of polarization-maintaining fiber is the most convenient solution, combining the low optical losses of the contemporary single-mode fibers with exceptionally good polarization stability.

Other important loss sources in optical fibers are the nonlinear processes, taking place at high power levels. They are in fact dominant when short powerful pulses are propagating through a fiber. In our case of CW fiber connection, only stimulated Brillouin and Raman scattering are relevant. In a laboratory single-mode fiber-connection of  $\sim 20$  m length in the visible, the threshold for SBS can be as low as 400 mW, whereas in few kilometers long single-mode fiber the stimulated Brillouin scattering limits the transmission at  $\sim 10$  mW level. The SBS threshold is calculated according to the relation  $P_{th} = 21A_{eff}/g_B L_{eff}$ , where  $A_{eff}$  and  $L_{eff}$  are the effective core area and fiber length, respectively;  $g_B = (\gamma_e^2 \omega^2)/(nc^3 \nu \rho_0 \Gamma_B)$  is the Brillouin gain (*see* Chapter 1 and Eq.(1.25)). Once the threshold is reached, a large part of the pump power is reflected back, thus reducing the transmission. The only way to overcome the stimulated scattering limitations is reducing either the fiber-length or the input power. In the experimental setup for precision frequency measurements in the XUV presented in Chapter 6 (*see* Fig. 6.1), the transmission through the fiber was indeed limited by the onset of SBS at an input power level of 500 mW.

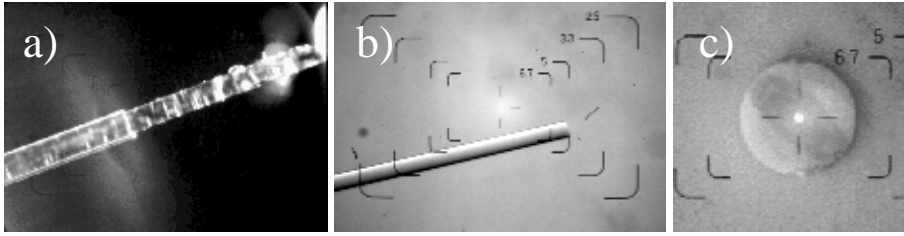


**Figure 7.4:** Microscope images of polarization-maintaining fiber; a) - stripped jacket, no cleaning; b) - after cleaning and cleaving; c) - the fiber cross section - the elliptically shaped stress-zone is clearly seen. Some light is coupled in for better visualization of the core.

In our set-up, the fiber connection is used in order to separate the CW and pulsed part of the set-up and to aid the alignment. A short 50 cm polarization-maintaining single-mode fiber ensures no stimulated scattering losses as well as excellent polarization and pointing stability at power levels of  $\approx 300$  mW. The fiber we use is 3M FS-PM-4611; mode-field diameter  $5.42 \mu\text{m}$ ; cladding diameter  $80 \mu\text{m}$ ; attenuation  $\alpha = 2.92$  dB/km @ 820 nm. It is designed for use at 820 nm with second mode cut-off at 715 nm. Microscope images of the fiber are shown in Fig. 7.4 in order to visualize better the cleaning and cleaving process. In Fig. 7.4a the jacket is stripped by dissolving it in

methylene-chloride. The image in Fig. 7.4b shows the cleaned and cleaved fiber-end. The cleaved tip is shown in Fig. 7.4c using magnification  $40\times$ . For better visualization of the core, some light is coupled in. The elliptical stress-zone around the core is seen as well.

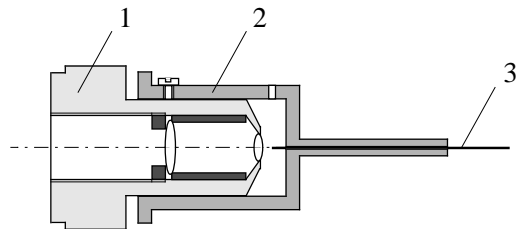


**Figure 7.5:** The in-coupling unit; 1 -  $10\times$  microscope objective; 2 - guiding aluminum fitting; 3 - fiber.

In Fig. 7.5 a schematic drawing of the in-coupling unit is shown as a demonstration of an easy and efficient way of launching light into a single-mode fiber. A microscope objective ( $10\times$ ) is used to focus the laser beam. The cleaned and cleaved fiber, glued to an aluminum fitting, is guided on the optical axis for fixing the proper distance  $z$  between the fiber-tip and the objective. Having fixed one of the five degrees of freedom ( $x, y, z, \theta, \phi$ ), the alignment involves maximizing the transmission by two pairs of angular degrees of freedom (one pair for the in-coupling unit and one pair for the last steering mirror). The procedure is straightforward and can be easily computerized if necessary.

## 7.4 Pulse-dye-amplifier

The light transmitted through the fiber, is used for seeding a three-stage pulse-dye-amplifier (PDA) operating on LDS 765 dye (see Fig. 7.6). The pump pulses are generated in an SBS pulse compressor and have 300 ps duration. The inset in Fig. 7.6 shows the compressor set-up where the remainder of the infrared beam after the first second-harmonic generation (SHG) stage is doubled again and pulses with energy  $\approx 130$  mJ and 6 ns pulse duration are achieved. These pulses pass through a thin-film polarizer used as polarizing beam-splitter (PBS) for the horizontal polarization. After a Fresnel rhomb the beam is transferred into a circular polarization state and enters a Brillouin cell filled with water. A concave mirror of 20 cm focal length situated behind the cell refocuses the light back into the water. In the focal plane a phase-conjugate Stokes pulse is generated, which propagating through the pump pulse is compressed (for more details on the SBS pulse compression see Chapter 2). We separate the Stokes pulses taking advantage of their polarization. The SBS process does not conjugate the polarization state of the light, hence the left-hand circular polarization is reflected as right-hand one and, after passing again through the Fresnel rhomb, the polarization is orthogonal to

the input one. At the output of the compressor pulses with energy  $\approx 100$  mJ/pulse and 300 ps duration are obtained.

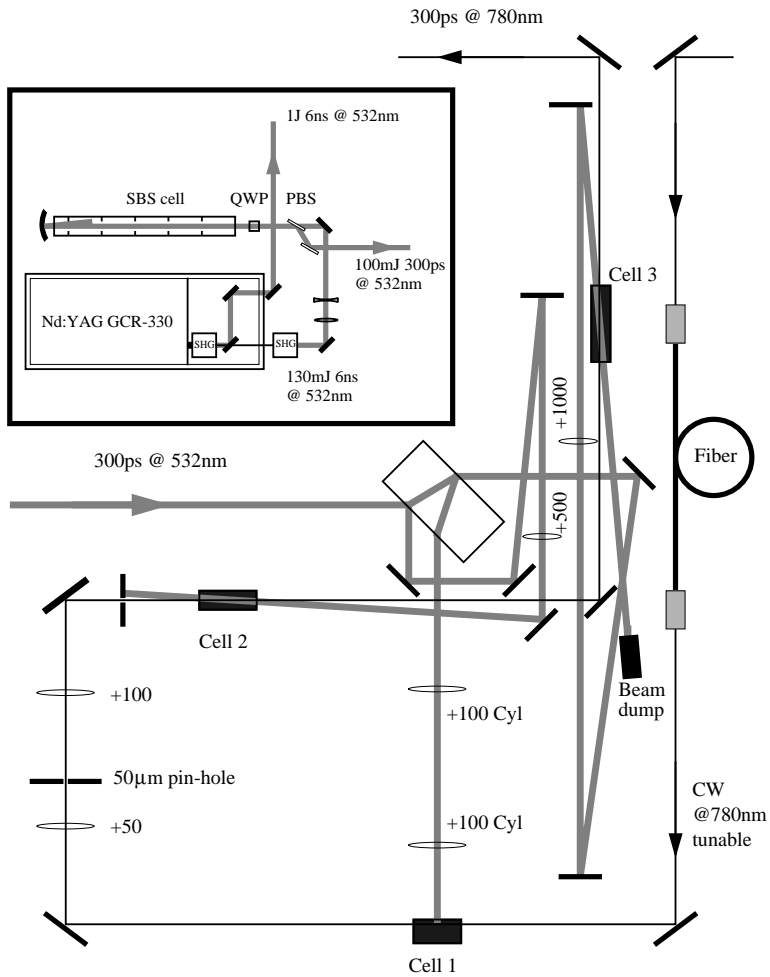


**Figure 7.6:** Pulse-dye-amplification set-up. The inset shows the SBS pulse compressor, generating 300 ps pulses for pumping of the PDA.

The PDA setup, shown in Fig. 7.6, consists of three tilted dye-cells. The first cell (139 mg/l LDS 765 in methanol) of the amplifier chain is transversely pumped by 4% of the pump power. Two cylindrical lenses are used to create a line-focus, concentrating the pump energy into a narrow region overlapped with the seed beam just behind the side wall of the cuvette. The weak pulses created in the first cell are spatially filtered and

amplified in two consecutive amplification stages (39 mg/l) both pumped longitudinally in direction opposite to the seed beam. The first one is pumped by 4% of the pump power, while the remaining  $\approx 90$  mJ pumps the third cell. Since the excited state lifetimes of the infrared dyes are of the order of 300 ps (see Fig. 7.7), the pump pulses in both second and third amplification stage must be properly delayed such that they arrive simultaneously with the infrared pulses. The output pulses of the PDA have  $\approx 300$  ps pulse duration with an energy in the pulse of  $\approx 2$  mJ.

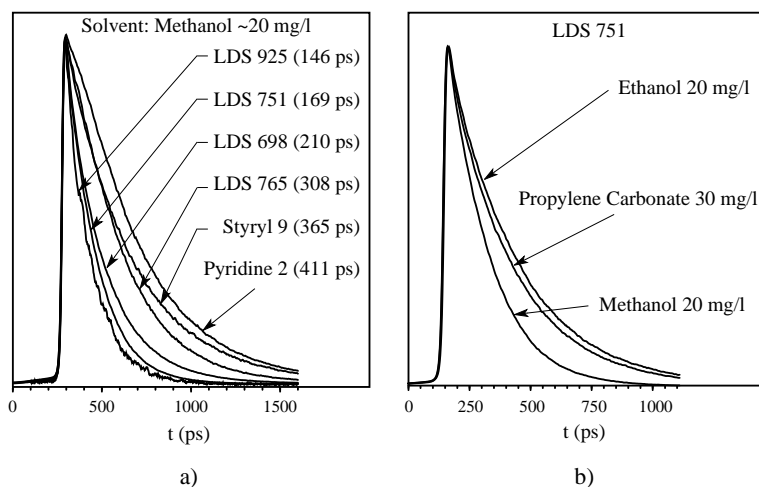


**Figure 7.7:** Fluorescence decay of different dyes measured with a pico-second streak-camera after a femto-second pulse excitation; a) - different dyes in methanol; b) - LDS 751 in different solvents. These measurements were performed with the equipment of the Biophysics laboratory, for which we are grateful to Prof. R. v. Grondelle and B. Gobets.

#### 7.4.1 Spectral and temporal characterization of the PDA output

The spectral characteristics of the PDA output are examined using the experimental setup shown in Fig. 7.8a where the infrared pulses are focused onto a diffuser in front of a Fabry-Perot interferometer (FPI). The transmission through a pin-hole is detected by a fast photodiode and the signal is gated in the presence of a PDA pulse by a boxcar integrator. The transmission peaks when scanning the frequency of the seed beam<sup>a</sup>, are shown in Fig. 7.8b. The CW seeding transmission is the *inverted* upper trace used for instrumental linewidth measurement ( $\Delta\nu_{CW} = 197(3)$  MHz at half-maximum level).

<sup>a</sup>Note that the scan is towards higher frequencies and, therefore the spectra recorded have the red frequencies on the right-hand side of the FPI transmission peak. In Fig. 7.9 this inconvenience is eliminated.

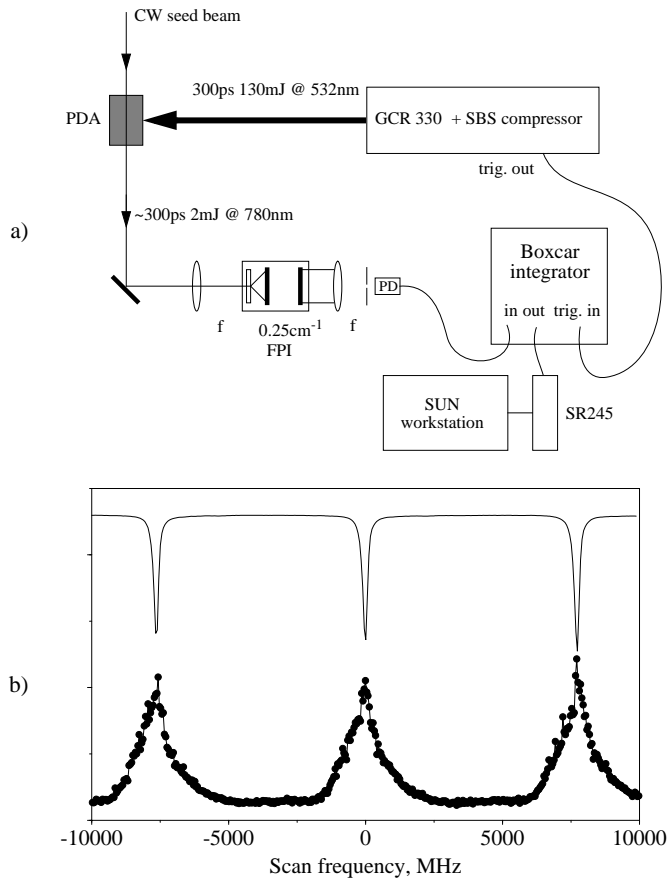


**Figure 7.8:** Spectral characterization of the PDA output. a) - Scheme of the experiment; b) - transmission peaks of the CW seeding (upper trace *inverted*) and the PDA output (lower trace) through a  $0.25 \text{ cm}^{-1}$  Fabry-Perot interferometer.

The PDA transmission is the lower trace. In Fig. 7.8b the contribution of the seed light can be seen on the red side of each transmission peak as well. Although the CW power level after the PDA is  $\sim 100 \text{ mW}$  and the pulsed peak-power is orders of magnitude higher, due to the CW spectral purity ( $\Delta\nu \sim 1 \text{ MHz}$ ) one can still observe it along with the three orders of magnitude broader pulsed spectrum.

An average over 20 transmission peaks is shown in Fig. 7.9a,c for two different output powers achieved by misalignment of the pump beam in the second amplifier cell. The curve through the points is a fit consisting of two peaks: a Lorentzian of fixed width  $\sim 197 \text{ MHz}$  (deduced from the CW transmission peaks in Fig. 7.8) and a Gaussian (for

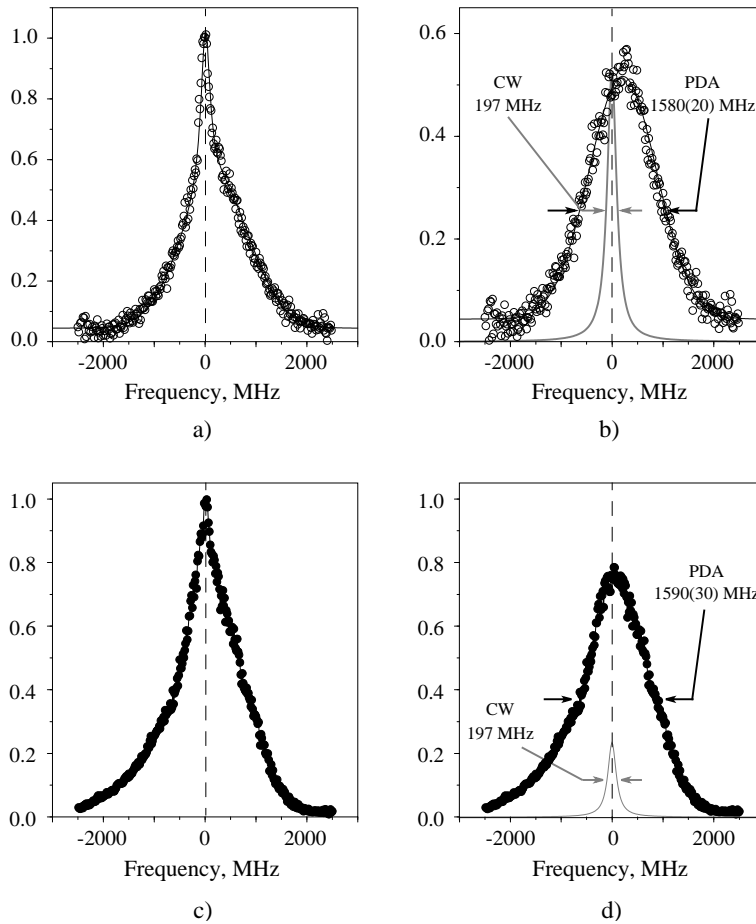


**Figure 7.9:** Spectral characterization of the PDA output; a) - an average over 20 transmission peaks (the data points) and a fit (see the text for details); b) - the CW contribution (the gray line) and the PDA transmission peak, fitted with a Gaussian function.

the PDA spectrum) with an unknown offset. By fitting such a curve the spectral width of the PDA output is obtained, as well as the chirp-induced frequency shift during the amplification process. In Fig. 7.9a the output power is reduced such that the spectral peak intensity of the output pulses is comparable with the peak intensity of the CW spectrum. This way the two contributions can be clearly distinguished. In Fig. 7.9b the CW contribution (the gray curve) has been subtracted from the data presented in Fig. 7.9a and the resulting PDA transmission peak was fitted with a Gaussian function.

A full-width at half-maximum of 1580(20) MHz is thus derived along with a blue shift of 198(6) MHz. The measured shift of  $\approx 200$  MHz is rather big and is most probably due to the combined effect of the lack of gain in the second cell, due to the pump misalignment, and the considerable gain experienced in the last cell. In Fig. 7.9c the averaged over 20 transmission peaks spectrum of the pulses when operating at maximum output power is presented. The Lorentz-Gaussian fit shows a reduced contribution of the CW transmission, along with a reduced chirp-induced frequency shift (*see* Fig. 7.9d). The measured blue shift in this case is 58(7) MHz; a three-fold reduction as compared to the one measured at lower power. The measured spectral width is 1590(30) MHz, not differing from the previously obtained value of 1580(20) MHz. This width is a convolution of the PDA spectral width and the instrument linewidth of 197 MHz. Hence, the PDA linewidth at half-maximum of 1570(20) MHz can be deduced.

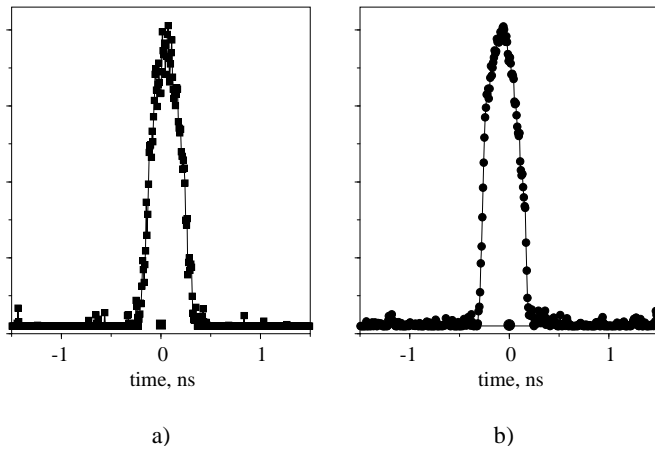


**Figure 7.10:** Pulse duration measurements with a streak camera; a) - the pump pulse from the SBS pulse compressor  $\tau_{SBS} = 337$  ps; b) - the output pulse of the PDA  $\tau_{PDA} = 358$  ps. The widths are measured at  $1/e$  level.

The pulse duration measurements are performed using a streak camera (Hadland IMACON 500 - 20 ps). In Fig. 7.10a the pump pulse from the SBS pulse compressor is shown, while in Fig. 7.10b the PDA output pulse is presented. The PDA pulse is consistently longer compared to the SBS one by  $\approx 20$  ps on average and its duration is measured to be  $\approx 358$  ps at  $1/e$  level. This corresponds (if Gaussian shape is assumed) to  $\approx 298$  ps at half-maximum.

In case of a Gaussian intensity distribution the Fourier-transform limited pulse duration  $\tau_{FWHM}$  measured at half-maximum level corresponds to a spectral full-width at



GCR-330 Nd:YAG laser (*see* Chapter 7.1). The general scheme of the pre-amplification stage is depicted in Fig. 7.11. The Ti:sapphire crystal is Brewster-cut in order to avoid reflection losses at the facets, and is mounted in a brass holder as shown in the inset in Fig. 7.11. The rectangular cross-section of the crystal allows for a direct-contact cooling from four sides. The pump beam from the Nd:YAG laser is split into two parts by a 90/10 beam-splitter, thus providing two pump channels of approximately 800 mJ for the multi-pass amplifier, and 100 mJ for the single-pass pre-amplifier. The beam is properly reshaped and focused by using the telescope shown in Fig. 7.11. It is subsequently directed towards the Ti:sapphire crystal under a proper angle, such that the pump light is counter-propagating to the seed light inside the crystal. The beam profiles, recorded as imprints on a photographic paper, are shown in Fig. 7.11 as well. A gray frame corresponds to a beam profile of the pump-beam, whereas a black frame is used to distinguish the infrared beam-profile photos.

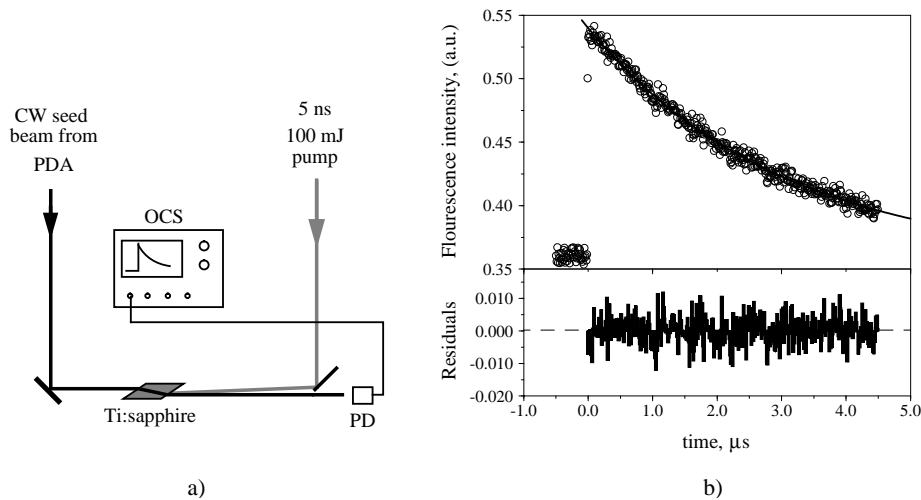


**Figure 7.12:** Fluorescence decay from the CW seeded pre-amplifier.

In order to study how critical the timings of the pump-pulse and the seed-pulse are we performed the experiment shown in Fig. 7.12a, where the pre-amplifier crystal is pumped by 100 mJ from the Nd:YAG laser and is seeded by the remainder ( $\approx 100$  mW) of the CW light only. A photodiode placed at the output of the pre-amplifier records the decay of the fluorescence (*i.e.* the population inversion) from the crystal. The result of such measurements (averaged over 32 shots) is presented in Fig. 7.12b, where the open circles represent the data points, the solid line is an exponential fit, and the bar-diagram below shows the residuals of the fit. The even distribution of the residuals is a proof for a single-exponential decay. The lifetime of the excited state is thus measured to be  $3.09(2) \mu\text{s}$  - more than 60 times shorter than the unseeded Ti:sapphire, but still providing enough room for time delay between the seed-pulse from the PDA and the

5 ns pump-pulse on a time-scale of few tens of nano-seconds.

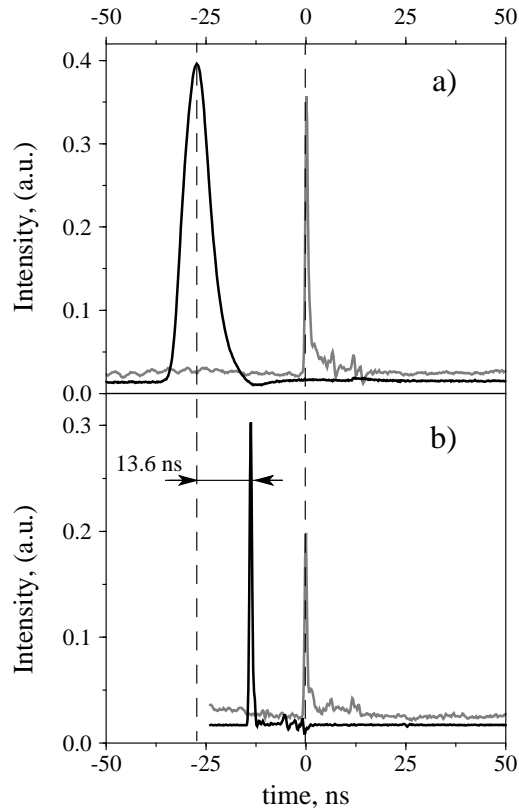


**Figure 7.13:** The timing of the pulses in the pre-amplifier; a) - the 5 ns pump pulse; b) - the pulse generated from the PDA. The gray curve in both graphs is the SBS pulse used as a reference point in time.

In the experimental realization of the pre-amplifier the pump pulse arrives 13.6 ns before the seed-pulse as measured on a fast photodiode. The results from this measurement are presented in Fig. 7.13a,b. The SBS pulse which pumps the PDA is depicted in gray in Fig. 7.13a,b and is used as a reference point in time for both measurements.

The optimization of the pre-amplifier involves fine alignment of the pump beam both in direction and size (*see* Fig. 7.14a) in order to achieve maximum amplification. The pulses after the pre-amplifier are monitored by a fast photodiode and a 1 GHz oscilloscope after considerable attenuation by using neutral-density filters. The amplification achieved is measured by comparing the height of the pulses from the PDA (the gray curve in Fig. 7.14b) with the pulses when the pump of the pre-amplifier is on (the black curve in Fig. 7.14b). Maximum amplification of 12 times can be deduced from such

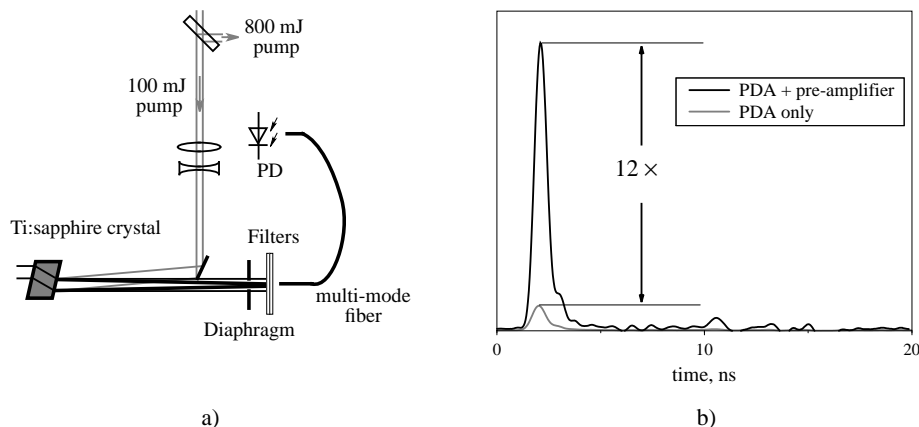


**Figure 7.14:** Pre-amplifier optimization. a) - experimental setup; b) - amplification measurement.

measurement, but it is important to note that this is not the energy amplification, since this measurement yields intensity ratio only. Due to thermal lensing induced in the Ti:sapphire crystal, the beam is focused thus increasing the peak intensity and resulting in a higher intensity ratio than the actual amplification. The effect of thermal lensing is also evident when examining the beam profiles before and after the pre-amplifier (*see* Fig. 7.11). A direct energy measurement yields  $\approx 6$  mJ/pulse after the pre-amplifier, which corresponds to amplification of  $\approx 3$ . The usually undesirable effect of thermal lensing can be efficiently used to separate the remainder of the seed beam from the pulses by merely inserting a diaphragm (*see* Fig. 7.14a) with a proper size in the focal spot, generated by the thermal lens.

### 7.5.2 Ti:sapphire multi-pass amplifier

The Ti:sapphire crystal is a high damage threshold high quality laser rod manufactured by Crystal Systems. It has cylindrical shape (*see* Fig. 7.15a); the path length through the crystal is  $L = 10$  mm; the crystal diameter is  $d = 10$  mm. The absorption coefficient at the pump wavelength 532 nm is  $\alpha = 2.3$  cm $^{-1}$ , which is equivalent to a low-power single pass (LPSP) absorption of 89.9% ( $A = 1 - \exp(-\alpha L)$ ). The figure of merit, defined as  $FOM = (\alpha_{532\text{ nm, P-pol}}/\alpha_{800\text{ nm, P-pol}})$ , is specified to be greater than 250, corresponding to less than 1% LPSP absorption at 800 nm. The crystal is with plane parallel facets, both broad-band anti-reflection coated to minimize the reflection losses. This is important since at least 4 passes are needed in order to achieve the high peak-power necessary for high-harmonic generation.

The design of the crystal holder is presented in Fig. 7.15b. A massive brass cylinder with the crystal nested in the middle is used to implement passive air cooling, while a

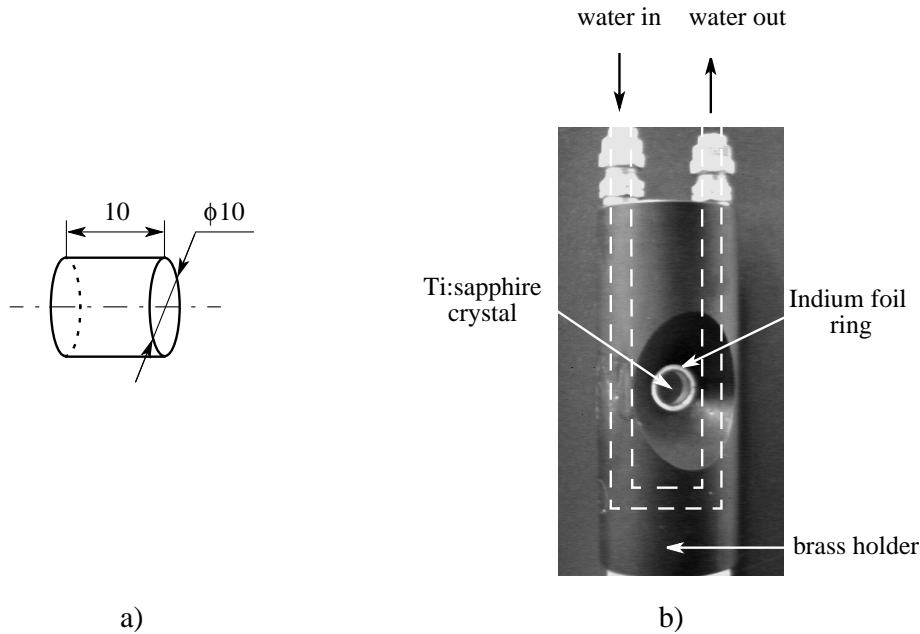


**Figure 7.15:** The Ti:sapphire multi-pass amplifier crystal; a) - crystal dimensions; b) - the crystal holder design.

water cooling option is also provided if necessary. For thermal contact with the cooler a 1 mm thick ring made from indium is used taking advantage of both its malleability and high thermal conductivity (*see* Fig. 7.15b).

The multi-pass amplification stage was still under construction when this Thesis was in preparation. Therefore no performance characteristics could be presented here. Our expectations based on amplification  $\approx 3$  per pass are that after 4 passes the output power would be of the order of 350 mJ per pulse.

## 7.6 Outlook

We are in the process of building a multi-pass amplifier in either mono-planar or a bi-planar geometry depending on the single-pass amplification. A schematic drawing of a mono-planar four-pass amplifier setup is presented in Fig. 7.16. The 800 mJ pulses from the GCR-300 Nd:YAG laser are split in two by means of a 50/50 beam-splitter (BS) and the two parts are used for longitudinal pumping of the Ti:sapphire crystal from both sides. In order to avoid interference between the two pump pulses inside the crystal one is delayed by 4 ns (*see* Fig. 7.16). The infrared seed 300 ps pulses pass four times through the crystal and are amplified following the mono-planar path depicted in

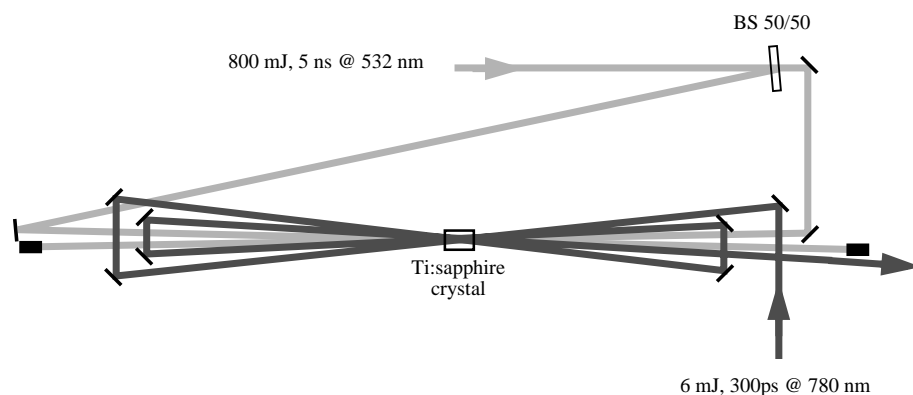


**Figure 7.16:** The Ti:sapphire four-pass mono-planar amplifier setup.

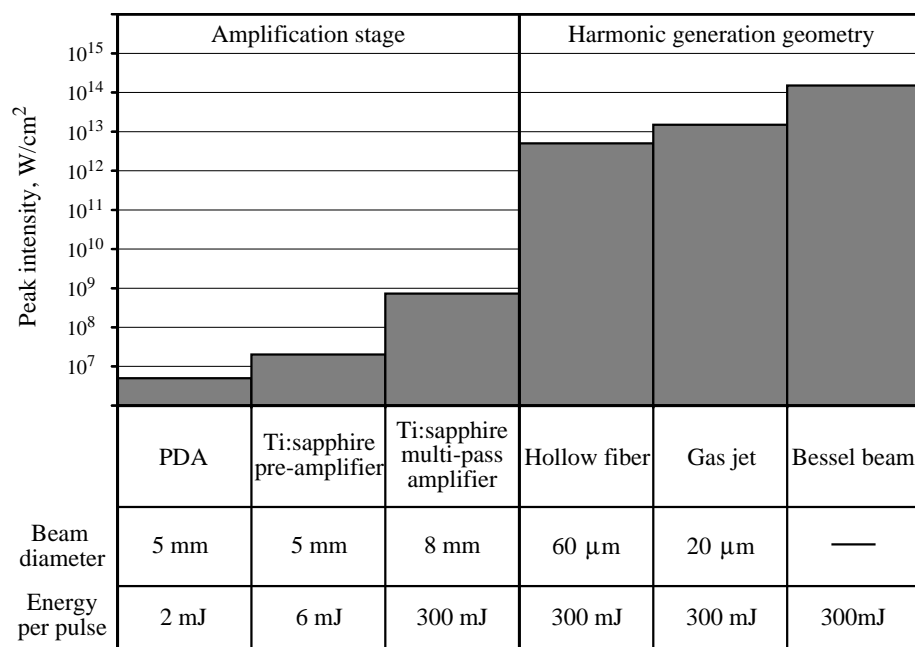


**Figure 7.17:** The expected peak intensities at different stages of the amplification and different harmonic generation geometries.

dark-gray in Fig. 7.16. Four passes are expected to deliver the desired output power of  $\approx 300$  mJ per pulse, but in case the amplification is less a complementary two or four

passes will be added in a plane tilted by a few degrees (bi-planar geometry).

In Fig. 7.17 a diagram is presented reflecting the peak intensities achieved/predicted at different stages of the amplification and different harmonic generation geometries. The PDA discussed in Section 7.4 delivers  $\approx 2$  mJ energy per pulse in  $\approx 5$  mm wide beam. This corresponds to a peak intensity of few times  $10^6$  W/cm<sup>2</sup>. After the pre-amplifier stage (*see* Section 7.5), assuming 5 mm beam diameter, the peak intensity is  $\sim 2 \times 10^7$  W/cm<sup>2</sup>. The expected 300 mJ per pulse after the multi-pass amplifier in  $\approx 8$  mm beam corresponds to  $\sim 1 \times 10^9$  W/cm<sup>2</sup> peak intensity. As discussed in Section 1.3, the peak intensity necessary for high-order harmonic generation is of the order of  $10^{13}$  W/cm<sup>2</sup> - a gap of at least four orders of magnitude that can be bridged by means of focusing to a typical beam diameter of 20  $\mu$ m or in a waveguide (hollow-fiber) with a typical diameter of 60  $\mu$ m (*see* Fig. 7.17). The use of a Bessel beam for harmonic generation may prove beneficial since the peak intensity can be an order of magnitude higher than in the case of focusing by a lens and the harmonic orders are generated on cones with different apex angles, thus facilitating their separation. The long line-focus (*see* Chapter 4) provides increased interaction length. All three geometries are in principle applicable in a high-order harmonic generation scheme, but the most efficient one is going to be experimentally chosen.

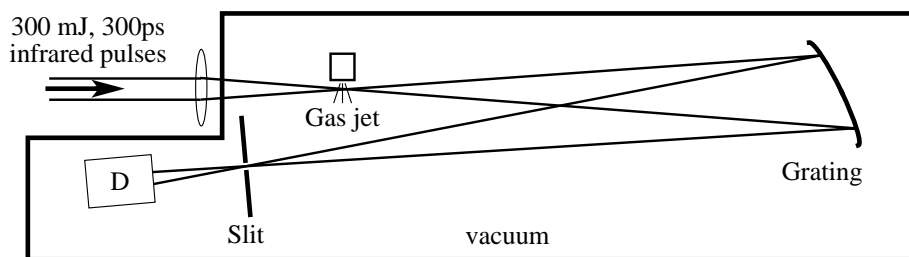


**Figure 7.18:** The harmonic order separation and detection setup.

In Fig. 7.18 the already built vacuum setup for harmonic order separation and detection is presented. It utilizes a concave grating under near normal incidence and focal length of 1 m as a dispersive element. The grating is optimized for 70 nm wavelength, hence the 11th harmonic will be most efficiently diffracted. It images the source (gas-jet or hollow fiber) onto a spot where a movable slit is placed for harmonic-order separation. The XUV photon intensity will be detected by an electron multiplier situated behind the slit. A scan through the harmonic orders is made possible by a motorized fine rotation of the grating. With this set-up we are planning to investigate the most efficient geometry for harmonic generation. The same setup will be used for spectroscopic studies in the XUV by adding another vacuum chamber where the XUV beam will interact with the species under investigation.

## References

- [1] K. S. E. Eikema, W. Ubachs, W. Vassen, W. Hogervorst, Phys. Rev. Lett. **76**, 1216 (1996).
- [2] D. Neshev, I. Velchev, W. Majewski, W. Hogervorst, and W. Ubachs, Appl. Phys. B **68**, 671 (1999).
- [3] J. Tyndall, Proc. Roy. Inst. **1**, 446 (1854).
- [4] G. P. Agrawal, "*Nonlinear Fiber Optics*", (Academic Press, Boston, 1989).



## Publications

### ARTICLES

- **Higher-order stimulated Brillouin scattering with non-diffracting beams**  
I. Velchev, W. Hogervorst, V. N. Belyi, and W. Ubachs,  
Opt. Lett. **26** (8), 530-532 (2001).
- **Predissociation in the E  $^1\Pi$ ,  $v = 1$  state of the six natural isotopomers of CO**  
W. Ubachs, I. Velchev, and P. Cacciani,  
J. Chem. Phys. **113** (2), 547-560 (2000).
- **Predissociation of b  $^1\Pi_u$ ,  $v(v = 1, 4, 5, 6)$  levels of N<sub>2</sub>**  
W. Ubachs, I. Velchev, and A. de Lange,  
J. Chem. Phys. **112** (13), 5711-5716 (2000).
- **Pulse compression to the sub-phonon lifetime region by half-cycle gain in transient stimulated Brillouin scattering**  
I. Velchev, D. Neshev, W. Hogervorst, and W. Ubachs,  
IEEE J. Quantum Electron. **QE-35** (12), 1812-1816 (1999).
- **Precision VUV spectroscopy of argon I at 105nm**  
I. Velchev, W. Hogervorst, and W. Ubachs,  
J. Phys. B **32** (17), L511-L516 (1999).
- **Steering of one-dimensional odd dark beams of finite length**  
A. Dreischuh, G. G. Paulus, F. Zacher, and I. Velchev,  
Appl. Phys. B **69** (2), 113-117 (1999).
- **SBS pulse compression to 200 ps in a compact single-cell setup**  
D. Neshev, I. Velchev, W. A. Majewski, W. Hogervorst, and W. Ubachs,  
Appl. Phys. B **68** (4), 671-675 (1999).
- **A Dense Grid Of Reference Iodine Lines For Optical Frequency Calibration In The Range 571-596nm**  
I. Velchev, R. van Dierendonck, W. Hogervorst, and W. Ubachs,  
J. Mol. Spectrosc. **187** (1), 21-27 (1998).

- **Multiple-Charged Optical Vortex Solitons in Bulk Kerr Media**  
I. Velchev, A. Dreischuh, D. Neshev, and S. Dinev,  
*Opt. Commun.* **140** (1-3), 77-82 (1997).
- **Interaction of Optical Vortex-Solitons Superimposed on Different Background Beams**  
I. Velchev, A. Dreischuh, D. Neshev, and S. Dinev,  
*Opt. Commun.* **130** (4-6), 385-392 (1996).
- **Phase Measurements of Ring Dark Solitons**  
A. Dreischuh, W. Fliesser, I. Velchev, S. Dinev, and L. Windholz,  
*Appl. Phys. B* **62** (2), 139-142 (1996).
- **Generation and Evolution of Two-Dimensional Dark Spatial Solitons**  
S. Baluschev, A. Dreischuh, I. Velchev, S. Dinev, and O. Marazov,  
*Phys. Rev. E* **52** (5), 5517-5523 (1995).
- **Odd and Even Two-Dimensional Dark Spatial Solitons**  
S. Baluschev, A. Dreischuh, I. Velchev, S. Dinev, and O. Marazov,  
*Appl. Phys. B* **61** (1), 121-124 (1995).

## PROCEEDINGS

- **Topological-charge controlled interaction within ordered structures of optical vortex solitons**  
M. Assa, I. Velchev, D. Neshev, A. Dreischuh, and S. Dinev,  
*Proceedings SPIE* **3502**, 218-222 (1997).
- **Two-Dimensional Dark Spatial Solitons**  
A. Dreischuh, S. Baluschev, I. Velchev, D. Neshev, S. Dinev, and O. Marazov,  
*Proceedings of VIII School on Quantum Electronics, Lasers and Applications 327-332* (1996) M. Nenchev, P. Atanasov, and M. Himber (eds.), University Paris-Nord, Paris

## ARTICLES SUBMITTED FOR PUBLICATION

- **Lifetime measurement on the  $c'_4 \ ^1\Sigma_u^+$ ,  $v=0, 1$ , and  $2$  states of molecular Nitrogen**  
W. Ubachs, R. Lang, I. Velchev, W.-U. L. Tchang-Brillet, A. Johansson, Z. S. Li, V. Likhnygin, and C-G. Wahlstrom,
- **High-Resolution VUV Spectroscopy of Xe: Hyperfine Splittings, Isotope Shifts and Isotope Dependent Ionization Energies**  
F. Brandi, I. Velchev, W. Hogervorst, and W. Ubachs.
- **Isotope dependent predissociation in the  $C \ ^1\Sigma^+$ ,  $v = 0$  and  $v = 1$  states of CO**  
P. Cacciani, F. Brandi, I. Velchev, C. Lyngå, C.-G. Wahlström, and W. Ubachs.

# Pulscompressie met gestimuleerde Brillouinverstrooiing en harmonische conversie - Toepassingen op precisie extreem-ultraviolet laserspectroscopie

## Samenvatting

Dit proefschrift handelt over precisiespectroscopie in het extreem ultraviolette (XUV) deel van het elektromagnetische spectrum, waarbij gebruik wordt gemaakt van twee niet-lineaire optische processen: gestimuleerde Brillouinverstrooiing (SBS) en harmonische conversie. Het eerste dient om laserpulsen efficiënt in tijdsduur te comprimeren om zodoende de hoge piekintensiteiten te bereiken, die nodig zijn om de opbrengst in het daaropvolgende harmonische conversieproces te verhogen. Het proces van SBS-pulscompressie wordt in het eerste deel van het proefschrift in detail behandeld, vanuit zowel een theoretisch als een experimenteel perspectief. Het gebruik van opeenvolgende tweede en derde harmonischen voor precisiespectroscopie in het XUV-domein wordt toegelicht. Een lasersysteem is in ontwikkeling, waarvan de meest recente resultaten worden beschreven in Hoofdstuk 7, dat de technieken van SBS-pulscompressie combineert met harmonische conversie; naar verwachting zullen daarmee smalbandige ( $\delta\nu/\nu \approx 3 \times 10^{-6}$ ) en golflengte-verstembare pulsen in het XUV geproduceerd worden.

Dit proefschrift bestaat uit 7 hoofdstukken met 58 figuren en 14 tabellen, en is als volgt samengesteld.

Hoofdstuk 1 geeft een inleiding op gestimuleerde Brillouinverstrooiing en hogere-orde harmonische conversie. Deze beide essentieel niet-lineaire optische processen zijn belangrijke ingrediënten voor de volgende hoofdstukken. Eerst worden de basistheorie van het SBS-proces en een aantal toepassingen besproken. De stationaire SBS-theorie wordt ontwikkeld met nadruk op twee belangrijke configuraties (SBS-versterker en SBS-generator), die essentieel zijn voor het begrip van het SBS-pulscompressieproces. De eerste experimenten aan SBS worden besproken vanuit een historisch perspectief, met als doel de ideeënontwikkeling te volgen die leidde tot SBS-pulscompressie in de jaren zestig, zeventig en tachtig van de afgelopen eeuw. Enkele van de vele praktische toepassingen van SBS worden ook behandeld. Aan het slot van Hoofdstuk 1 worden de fundamentele begrippen aangaande harmonische conversie geïntroduceerd, zowel voor de geometrie met een focus als voor bundels in lichtgeleiders.

Verschillende methoden voor de experimentele realisatie van SBS-pulscompressie worden besproken in Hoofdstuk 2. De tweede en derde harmonischen van een Nd:YAG

laser worden efficiënt gecompriëerd in verschillende vloeistoffen in een nieuw ontwikkelde experimentele opstelling met slechts één cel die tegelijkertijd dient als versterker en generator. Laserpulsen van 5 ns tijdsduur, zoals geproduceerd in commerciële Nd:YAG lasers (die wel een z.g. “injection-seeder” bevatten), kunnen op zeer efficiënte wijze worden gecompriëerd tot pulsen van 200 ps lengte; op deze manier worden commercieel beschikbare lasers veelzijdig inzetbare instrumenten, ook in dynamische studies en niet-lineaire optische studies.

Hoofdstuk 3 behandelt de mogelijkheid om laserpulsen te comprimeren, zodanig dat ze korter worden dan de levensduur van de fononen in de vloeistof. Een nieuwe theoretische benadering van SBS wordt gepresenteerd, waarin ook ultrasnelle tijdsvariëaties worden meegenomen; deze theorie laat zien wat de werkelijke fysische beperkingen zijn voor het produceren van korte pulsen via SBS. Een numerieke methode is ontwikkeld die de evolutie van het SBS-proces beschrijft, ook op de zeer korte tijdschaal. Onder geoptimaliseerde condities kunnen pulsen worden geproduceerd met een pulsduur zo kort als een halve akoestische trilling in de vloeistof. Deze theoretische voorspelling is ook experimenteel bevestigd.

In Hoofdstuk 4 is een fundamentele experimentele studie verricht aan het SBS-proces uitgaande van een optische bundel met een Bessel-geometrie. In dat geval zijn voor het eerst hogere-orde Stokes-componenten waargenomen, die ontstaan via stapsgewijze verstrooiing in de vloeistof. De ruimtelijke, spectrale en temporele eigenschappen van de wisselwerkende lichtgolven worden besproken.

Hoofdstuk 5 is een bijdrage aan de metrologie. Gebruik makend van dopplervrije verzadigingsspectroscopie in jodiumdamp werden in het golflengtegebied 571 – 596 nm meer dan 100 hyperfijncomponenten absoluut gecalibreerd met een nauwkeurigheid van 2 MHz. In combinatie met een theoretische studie van de hyperfijnstructuur werd de absolute frequentie van 1584 hyperfijncomponenten in 6 banden voorspeld met een nauwkeurigheid van 2 MHz voor vibratiequantumgetallen  $13 \leq v' \leq 18$  en rotatiequantumgetallen  $9 \leq J \leq 140$ . Deze frequenties vormen een dicht rooster van referentielijnen (één in elk interval van  $1 \text{ cm}^{-1}$ ) en zijn bovendien meer dan een orde van grootte nauwkeuriger dan de lijnen in de veel gebruikte jodiumatlas, die gebaseerd is op dopplerverbrede lijnen. Hiermee is de nieuwe jodiumatlas een handzame referentie voor golflengtekalibratie en precisiestudies in de spectroscopie.

In Hoofdstuk 6 wordt beschreven hoe deze nieuwe referentiestandaard gebruikt wordt in precieze frequentiekalibratie in het domein van het extreme ultraviolet. Een smalbandige laserbron, gebaseerd op opeenvolgende tweede en derde harmonische conversie van intense Fourier-gelimiterde pulsen, wordt toegepast in spectroscopische studies aan argon, krypton en stikstof bij golflengten korter dan 105 nm. Een hoge absolute nauwkeurigheid van 100 MHz wordt behaald via gelijktijdige meting van het verzadigingsabsorptiespectrum van  $\text{I}_2$  en de transmissiepieken van een actief gestabiliseerd etalon in het zichtbare golflengtegebied.

In Hoofdstuk 7 wordt een nieuw project beschreven. De wetenschappelijke resultaten uit voorgaande hoofdstukken worden gecombineerd in een ontwerp voor een nieuwe smalbandige en verstembare XUV-laserbron. Recente resultaten worden gepresenteerd. Het ontwerp is gebaseerd op hogere-orde harmonische conversie van intense infrarood-

pulsen van 300 ps tijdsduur. Licht uit een smalbandige continue titaan-saffier laser wordt pulsversterkt in een keten van kleurstofversterkers, die gepompt worden met SBS-gecomprimeerde pulsen uit een Nd:YAG laser. Resulterende infraroodpulsen van 300 ps tijdsduur met Fourier-gelimiteerde bandbreedte zullen daarna verder versterkt worden in een titaan-saffier versterker met meerdere doorgangen, om zodoende hoogenergetische pulsen te produceren die gebruikt kunnen worden voor XUV-productie.



# Компресиране на импулси чрез стимулирано Брилуеново разсейване и генерация на хармонични - приложения за прецизна спектроскопия в дълбокия ултравиолет

## Обобщение

Настоящата Дисертация е посветена на прецизна спектроскопия в дълбокия ултравиолет (ДУВ) с помощта на два типа нелинейни процеси: стимулирано Брилуеново разсейване (СБР) и генерация на хармонични. Компресиране на оптични импулси чрез СБР е използвано за постигане на висок пиков интензитет необходим за повишаване ефективността при генерацията на хармонични. В първата част на Дисертацията процесът на високо-ефективно компресиране на импулси чрез СБР е изследван детайлно както теоретично, така и експериментално. В допълнение, използването на последователно генериране на втора и трета хармонични за прецизни честотни измервания в ДУВ е успешно демонстрирано. В процес на разработка е и нова лазерна система (последните резултати са представени в Глава 7), в която компресиране на импулси чрез СБР и генерация на високи хармонични са съчетани за постигане на честотно пренастройваеми импулси в ДУВ с висока степен на монохроматичност ( $\delta\nu/\nu \approx 3 \times 10^{-6}$ ).

Дисертацията се състои от 7 глави и включва 58 фигури, 14 таблици и е организирана както следва.

Глава 1 е въведение в процесите на стимулирано Брилуеново разсейване и генерация на високи хармонични. Тези два нелинейни феномена са важни елементи в настоящата Дисертация и имат тясна връзка с материала, представен в следващите глави. В първите две части на Глава 1 общата теория на Брилуеновото разсейване е разгледана заедно с някои от многобройните му приложения. Стационарната теория на СБР е развита, като ударението е поставено върху двете важни конфигурации (СБР усилвател и СБР генератор) необходими за дълбокото разбиране на компресията на импулси чрез СБР. От историческа гледна точка, първите експерименти със СБР са дискутирани накратко с основна цел да се проследи еволюцията на идеи през 60-те 70-те и 80-те години на XX век, довела до реализацията на ефективно компресиране на импулси чрез СБР. Някои от многобройните практически приложения на СБР тясно свързани със съдържанието на настоящата

дисертация са подробно разгледани. В последната част на Глава 1 общите идеи лежащи в основата на генерацията на високи хармонични е представена, като двете важни геометрични конфигурации (вълноводна и фокусирана) са съпоставени.

Различни експериментални реализации на компресия на оптични импулси чрез СБР са разгледани в Глава 2. Втора и трета хармонични на Nd:YAG лазер са ефективно компресирани в различни течности, използвайки нова схема, съчетаваща генератор и усилвател в една кювета. Продължителност на компресираните импулси до 200 пс е постигната с изключително висока ефективност от първоначалните 5 нс импулси, генерирани от комерсиален Nd:YAG лазер с Q-модулация. Компресията по напречното сечение на лазерния сноп е също изследвана. Предложена е рецепта за контрол върху продължителността на изходния импулс в интервала 2 нс - 200 пс, като по този начин широко разпространените Nd:YAG лазери, налични на пазара, се превръщат в многофункционални лабораторни средства за динамични и нелинейни оптични изследвания.

Възможността за компресиране на импулси чрез СБР под границата определена от времето на живот на фононите е основна тема на Глава 3. Нов теоретичен подход към нестационарния СБР-процес е представен, разкриващ реалните физически ограничения към продължителността на изходния импулс в СБР компресор. Разработен е числен метод за моделиране еволюцията на процеса в напълно нестационарен режим, като различните етапи са детайлно дискутирани. При подходящи условия, импулси с продължителност равна на половин акустичен период се генерират. Експериментално изследване на процеса в нестационарен режим потвърждава теоретичните резултати.

Фундаментално изследване на СБР с напмпване от недифрактиращ (Беселов) сноп е представено в Глава 4. Стоксови компоненти от висок порядък са наблюдавани за първи път, в резултат на многократно разсейване в обемна нелинейна среда. Пространствените, времеви и спектрални характеристики на вълните, участващи в процеса са дискутирани.

Глава 5 представлява принос към прецизната метрология. С помощта на суб-Доплерова спектроскопия на насищането в молекулен йод в интервала 571 – 596 нм, над 100 компоненти от свръхфината структура на  $B-X$  системата са калибрирани със средна абсолютна точност от 2 МHz. В комбинация с теоретично изследване на свръхфиното разцепване в разглежданите преходи, абсолютните честоти на 1584 компоненти в шест  $(v'-1)$  ивици ( $v' = 13..18$ ) са предвидени със средна точност от 2 МHz за  $9 \leq J \leq 140$ . Този набор от калибрирани компоненти формира мрежа от отправни честоти за прецизни спектроскопски изследвания, с повече от порядък по-добра точност от широко използвания атлас, базиран върху Доплерово-уширени преходи във видимия спектър на йод. Най-малко една калибрирана честота във всеки обратен сантиметър осигурява леснота на използване и пълнота на нововъведения набор от стандартни честоти, което го прави полезно средство за прецизни честотни измервания.

Този прецизен спектрален атлас, заедно с разширента му версия към дълговълновата част на спектъра е използван за честотно калибриране на атомни и молекулни преходи в ДУВ. Резултатите от тези изследвания са представени в Глава 6. Лазерен източник с висока степен на монохроматичност, основан на последователна генерация на втора и трета хармонични от мощни Фурие-ограничени импулси е приложен за прецизни спектроскопски изследвания на аргон, ксенон и азот в околност на 105 нм. Високата абсолютна точност на измерванията е постигната чрез едновременна регистрация на наситения спектър на йод и ивиците на пропускане на Фабри-Перо еталон във видимата област, заедно със спектъра в ДУВ. С настоящото изследване доказваме, че предложената експериментална схема води до ненадмината абсолютна точност от порядъка на 100 МНз при честотните измервания в ДУВ.

В Глава 7 развитието на един нов проект е разгледано. Той обединява научните резултати изложени в предходните глави в нов пренстройваем лазерен източник с висока степен на монохроматичност в ДУВ. Основната идея се базира на генерация на високи хармонични от мощни инфрачервени 300 пс импулси. Тясноивичен непрекъснат Ti:Sapphire лазер с кръгов резонатор е използван за зараждане на лъчението<sup>a</sup> във верига от багрилни усилватели, напмпвани от СБР компресирани импулси генерирани от Nd:YAG лазер. По този начин пренастройваеми, Фурие-ограничени импулси с продължителност от 300 пс са усилены в многопроходен Ti:Sapphire усилвател за постигане на високо енергетични импулси, използвани в последствие при генерацията на високи хармонични.

---

<sup>a</sup>англ. "injection seeding"



## Dankwoord

My sincere gratitude goes first to Wim Ubachs for his key contribution to the results presented in this Thesis; for the support and for the numerous ideas. I am thankful to Wim Hogervorst for all the help, and for allowing me the freedom to pursue diverse scientific goals I have found interesting outside my main field of research. To Wim Vassen; the discussions with him were always fruitful. I am very much indebted to our technician Jacques Bouma, who was of enormous help on the technical side of every new experiment and who has always had elegant solutions in mind.

I wish to thank all my colleagues from the Atomic Physics Group: Norbert Herschbach, Arno de Lange, Paul Tol, Elmar Reinhold, Kjeld Eikemma, Joop Mes, Eric-Jan van Duijn, Stefan Petra, Maarten Snee, Rüdiger Lang, Jeroen Koelemeij, Roland Stas, for the help, and for their patience and understanding. Many thanks to my colleagues who had left our group during my time and who had helped me to enjoy my work and my stay in Amsterdam: Wojciech Majewski, Hans Naus, Annemieke Kips, Kees Karremans, Marc Leblans, Paul Hinnen, Roelant van Dierendonck, and Fernando Brandi.

Special thanks to our collaborators from Lund Institute of Technology, Sweden: Claes-Göran Wahlström, Vladimir Likhnygin, Allan Johansson, and Li Zhongshan for the fruitful three weeks of experiments in the spring of year 2000. Many thanks to Patrice Cacciani for the good time during the two excellent experiments in CO we conducted together in Amsterdam.

Благодаря на Александър Драйшу за модела на учен, който той отстоява, и който чрез своя опит и търпение ми помагаше през изминалите осем години. Благодаря също и на Стоян Динев за подкрепата толкова важна в началото на научната ми кариера. На Драгомир Нешев за приятелството и плодотворните дискусии по време на неколкото му пребиваване в Амстердам.<sup>a</sup>

Warm thanks to my good friend Norbert Nerschbach for the great time spent together; for the Sunday evenings in Uilenstede Café, where along with the drinks some great ideas were born; for the numerous enjoyable discussions about Physics, politics, economics, philosophy, etc.; for the evenings we cooked together and for the wine.

Благодаря от сърце на моите родители Цветан Велчев и Йорданка Велчева, както и на сестра ми Мирена Велчева за всеотдайната подкрепа и грижите.

---

<sup>a</sup>English translation: I would like to thank Alexander Dreischuh for the example of a scientist he stands up for, and whose experience and patience were helping me during the past eight years. I am grateful to Stoyan Dinev for the support he gave me in the beginning of my scientific career. To Dragomir Neshev for the friendship and for the fruitful discussions during his stays in Amsterdam.

На съпругата ми Христина и на сина ми Александър за обичта и щастливите мигове с които те ме даряват и без чиято подкрепа не бих могъл да преодоля многобройните трудности, с които животът в чужбина ме сблъска.<sup>b</sup>

---

<sup>b</sup>English translation: I am deeply grateful to my parents Tzvetan Veltchev and Iordanka Veltcheva, as well as to my sister Mirena Veltcheva for the support and the care. To my wife Hristina and my son Alexander for the love and the moments of happiness they gave me and without whose support I couldn't have overcome the difficulties which the life abroad confronted me with.